AEDC-TR-96-3

Experimental Characterization of Gas Turbine Emissions at Simulated Flight Altitude Conditions

R. P. Howard et al
Sverdrup Technology Inc., AEDC Group

September 1996

Final Report for Period January 1995 to April 1996

DTIC QUALITY INSPECTED 2

ARNOLD ENGINEERING DEVELOPMENT CENTER
ARNOLD AIR FORCE BASE, TENNESSEE
AIR FORCE MATERIEL COMMAND
UNITED STATES AIR FORCE

19960924 064

APPROVAL STATEMENT

This report has been reviewed and approved.

TRUNG V. LE
Technology Project Engineer
Applied Technology Division
Test Operations Directorate

Approved for publication

FOR THE COMMANDER

ROBERT T. CROOK
Asst. Chief, Applied Technology Division
Test Operations Directorate

REPORT DOCUMENTATION PAGE

Per is reported, burden for this collection of information is estimated to average 1 hour per response, including the time for reviewing instructions, searching existing data sources, gathering and maintaining the data needed, and completing and reviewing the collection of information. Send comments regarding this burden estimate or any other aspect of this collection of information, including suggestions for reducing this burden, to Washington Headquarters Services, Directorate for Information Operations an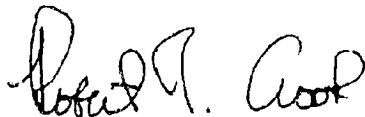d Reports, 2 15 Jefferson Davis Highway, Suite 1204, Arlington, VA 22202-4302, and to the Office of Management and Budget, Paperwork Reduction Project (0704-0188), Washington, DC 20503.

1. AGENCY USE ONLY (Leave blank)	2. REPORT DATE	3. REPORT TYPE AND DATES COVERED
	September 1996	Final January 1995 through April 1996

4. TITLE AND SUBTITLE	5. FUNDING NUMBERS
Experimental Characterization of Gas Turbine Emissions at Simulated Flight Altitude Conditions	Job No. 2100 ZTS96DOT

6. AUTHOR(S)

R.P. Howard et al.   J.C. Wormhoudt   P.D. Whitefield
Sverdrup Technology, Inc., AEDC Group   Aerodyne Research, Inc   Unversity of Missouri

7. PERFORMING ORGANIZATION NAME(S) AND ADDRESS(ES)	8. PERFORMING ORGANIZATION REPORT NUMBER
Arnold Engineering Development Center/DOT Air Force Materiel Command Arnold AFB, TN 37389 9011	AEDC-TR-96-3

9. SPONSORING/MONITORING AGENCY NAME(S) AND ADDRESS(ES)	10. SPONSORING/MONITORING AGENCY REPORT NUMBER
NASA Lewis Research Center 21000 Brookpark Road Cleveland, OH 44135-3191	

11. SUPPLEMENTARY NOTES

Available in Defense Technical Information Center (DTIC).

12A. DISTRIBUTION/AVAILABILITY STATEMENT	12B. DISTRIBUTION CODE
Approved for public release; distribution is unlimited.	

13. ABSTRACT (Maximum 200 words)

NASA's Atmospheric Effects of Aviation Project (AEAP) is developing a scientific basis for assessment of the atmospheric impact of subsonic and supersonic aviation. A primary goal is to assist assessments of United Nations scientific organizations and hence, consideration of emissions standards by the International Civil Aviation Organization (ICAO). Engine tests have been conducted at AEDC to fulfill the need of AEAP. The purpose of these tests is to obtain a comprehensive database to be used for supplying critical information to the atmospheric research community. It includes (1) simulated sea-level-static test data as well as simulated altitude data; and (2) intrusive (extractive probe) data as well as non-intrusive (optical techniques) data. A commercial-type bypass engine with aviation fuel was used in this test series. The test matrix was set by parametrically selecting the temperature, pressure, and flow rate at sea-level-static and different altitudes to obtain a parametric set of data.

14. SUBJECT TERMS					15. NUMBER OF PAGES
emissions turbine exhaust		gas turbine	exhaust emissions	IR-TDL	159
particulates particles		ultraviolet absorption	resonance absorption		16. PRICE CODE

17. SECURITY CLASSIFICATION OF REPORT	18. SECURITY CLASSIFICATION OF THIS PAGE	19. SECURITY CLASSIFICATION OF ABSTRACT	20. LIMITATION OF ABSTRACT
UNCLASSIFIED	UNCLASSSIFIED	UNCLASSIFIED	SAME AS REPORT

COMPUTER GENERATED

DISCLAIMER NOTICE
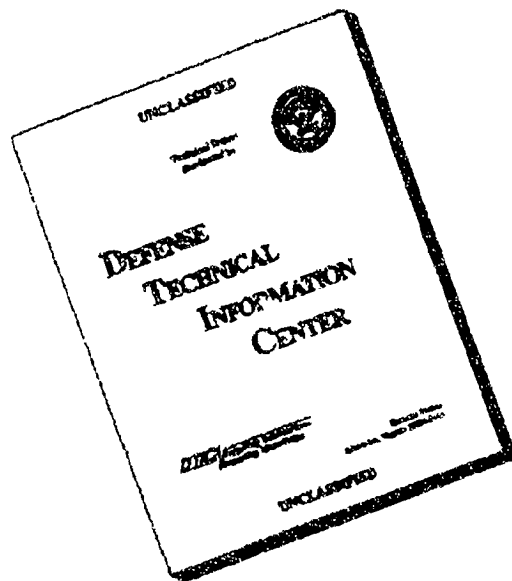
THIS DOCUMENT IS BEST
QUALITY AVAILABLE. THE
COPY FURNISHED TO DTIC
CONTAINED A SIGNIFICANT
NUMBER OF PAGES WHICH DO
NOT REPRODUCE LEGIBLY.

PREFACE

The work reported herein was sponsored by NASA through the Atmospheric Effects of Aviation Project under the Engine Exhaust Trace Chemistry Committee and managed through the NASA Lewis Research Center by Mr. Richard Niedzwiecki, NASA, and Dr. Chowen Chou Wey, Army Research Lab (ARL).

The work reported herein was conducted at the Arnold Engineering Development Center (AEDC), Air Force Materiel Command (AFMC), Arnold AFB, TN. The work was accomplished by the combined efforts of Sverdrup Technology, Inc. (AEDC Group), NASA Lewis Research Center (NASA LeRC), Pratt & Whitney (PW), Aerodyne Research, Inc. (ARI), and the University of Missouri-Rolla (UMR). Sverdrup Technology is the test contractor for AEDC, AFMC, Arnold Air Force Base, TN. The AEDC efforts were performed under Job No. 2100 and coordinated by the Air Force Project Manager, Mr. Trung Le. In addition to being a major participant, Sverdrup provided technical coordination among the investigative agencies under the direction of Dr. Robert P. Howard, Principal Investigator and Sverdrup Project Manager. The manuscript was submitted for publication on July 19, 1996.

The major objective of this report was to document the results of a set of parametric measurements of engine exhaust emissions conducted on a gas turbine engine in an AEDC simulated altitude test facility. The primary authors were:

Dr. Robert P. Howard	Sverdrup/AEDC
Mr. Robert S. Hiers, Jr.	Sverdrup/AEDC
Dr. Phillip D. Whitefield	University of Missouri-Rolla
Dr. Donald E. Hagen	University of Missouri-Rolla
Dr. Joda C. Wormhoudt	Aerodyne Research, Inc.
Dr. Richard C. Miake-Lye	Aerodyne Research, Inc.
Mr. Richard Strange	Pratt and Whitney, East Hartford

The scope of work defined in the project objectives required the services and cooperation of many engineers and scientists from several government and private organizations. The work and documentation reported herein is an accumulation of contributions from individuals acknowledged below and other persons too numerous to list. Although participants were a team with contributions beyond individual responsibilities, primary functions associated with each include:

NASA Project Management	Mr. Richard Niedzwiecki	NASA LeRC
	Dr. Chowen Chou Wey	ARL/NASA LeRC

1

Air Force Project Management	Mr. Trung V. Le	AF/AEDC
	Capt. Lee Lopes	AF/AEDC
Principal Investigator and Sverdrup Project Manager	Dr. Robert P. Howard	Sverdrup/AEDC
Technical Direction	Dr. Robert P. Howard	Sverdrup/AEDC
	Mr. Richard Niedzwiecki	NASA LeRC
	Mr. Richard Strange	PW-East Hartford
	Mr. Robert S. Hiers, Jr.	Sverdrup/AEDC
	Dr. Chowen Chou Wey	ARL/NASA LeRC
AEDC Test Facility	Mr. Robert Ballard	Sverdrup/AEDC
	Mr. Noel Pujol	Sverdrup/AEDC
	Mr. Scott Grigsby	Sverdrup/AEDC
	Mr. Dave Hester	Sverdrup/AEDC
	Mr. Steve Arnold	Sverdrup/AEDC
Air Force Data Release	Mr. Trung V. Le	AF/AEDC
	Capt. Lee Lopes	AF/AEDC
	Lt. Roy Glassco	Wright Patterson, AFB
Probe Rake Design, Development, and Application	Mr. Robert S. Hiers, Jr.	Sverdrup/AEDC
NO-UV Resonance and Continuum Absorption Systems	Dr. Robert P. Howard	Sverdrup/AEDC
	Ms. Alecia Davis	Sverdrup/AEDC
	Mr. Joseph Money	Sverdrup/AEDC
IR-Tunable Diode Laser	Dr. Joda C. Wormhoudt	ARI
	Dr. Richard C. Miake-Lye	ARI
	Mr. Ben Hartsfield	Sverdrup/AEDC
Mobile Aerosol Sampling System	Dr. Phillip D. Whitefield	UMR
	Dr. Donald E. Hagen	UMR
	Dr. Harvey Lilenfield	McDonnell Douglas
	Mr. Alfred R. Hopkins	UMR
	Mr. Max B. Trueblood	UMR
	Mr. Jonathan Paladino	UMR

Extractive Gas Sampling	Mr. Vincent A. Zaccardi	Sverdrup/AEDC
	Mr. Donald G. Gardner	Sverdrup/AEDC
	Mr. Douglas J. Gonnion	Sverdrup/AEDC
	Mr. Jeffrey A. Ready	Sverdrup/AEDC
	Mr. Paul A. Jalbert	Sverdrup/AEDC
	Mr. Robert S. Hiers, Jr.	Sverdrup/AEDC
	Dr. Robert P. Howard	Sverdrup/AEDC
	Daniel R. Catalano	Sverdrup/AEDC
OH Laser Absorption	Mr. Carl W. Brasier	Sverdrup/AEDC
	Dr. James A. Drakes	Sverdrup/AEDC
	Mr. Ronald G. Porter	Sverdrup/AEDC
	Mr. Michael D. Forsythe	Sverdrup/AEDC
	Dr. Robert P. Howard	Sverdrup/AEDC

CONTENTS

ILLUSTRATIONS

TABLES

APPENDICES

1.0 INTRODUCTION

The National Aeronautics Space Administration (NASA), charged with the responsibility for the development of advanced combustor technologies for both subsonic and supersonic aircraft, is developing a database for assessment of the atmospheric impact of aircraft emissions under the NASA Atmospheric Effects of Aviation Project (AEAP). Quantitative levels of emissions for various classes of engines are vital inputs to atmospheric models developed for such assessment programs. In support of these efforts, gaseous and particulate emissions were measured exiting an engine containing an annular combustor, representative of modern combustor technology. In addition to emissions at altitude, data were acquired at conditions equivalent to sea-level-static to assess the validity of extrapolation techniques used to determine altitude emissions from measurements obtained at sea-level conditions. The combustor size was representative of a 133-178 kN (30-40,000 lbf) thrust commercial engine. Altitude testing was primarily at 0.8 flight Mach number for simulation of commercial cruise operation. The measurements were performed at Arnold Engineering Development Center (AEDC) at simulated altitude conditions ranging from sea-level-static (SLS) to 15.3 km. The engine was operated over a range of combustor temperatures and pressures at each of several altitudes to provide the atmospheric modeling community with detailed measurements of altitude cruise emissions and to provide NASA a set of parametric data that will provide insight to exhaust emission variations as a function of combustor parameters and altitude.

Extractive gas and aerosol sampling and nonintrusive optical measurement systems were used to characterize emissions in the exhaust. This provided independent measurement techniques for gaseous constituents and permitted comparison of optical nonintrusive diagnostics with the reference conventional gas extractive methods. Optical techniques included both ultraviolet (UV) and infrared (IR) for in-situ nonintrusive measurements of gaseous constituents. Extractive techniques included a suite of instruments recommended by the Society of Automotive Engineers (SAE) for measuring gaseous species and smoke number and a unique particulate sampling system developed by the University of Missouri-Rolla (UMR). The UMR system, referred to as the Mobile Aerosol Sampling System (MASS), is being developed in part through the NASA AEAP because the current industry standard for particulate characterization in jet engine emissions, the "smoke number" technique, does not provide enough information to characterize the aerosol emitted. Although useful, "smoke number" does not provide the essential characteristics: total aerosol and non-volatile aerosol concentration, size distribution, and hydration or growth as measured by soluble mass fraction and critical supersaturation spectrum. These data are essential in order to effectively assess the environmental impact of particulate engine emissions, since they also represent the input parameters required by models designed to describe the production and dispersion of engine aerosol emittants from the combustor, through the exhaust nozzle plane to their eventual equilibration with the ambient atmosphere.

Exhaust samples were extracted using a multi-point cruciform rake assembly located near the engine nozzle exit plane with the versatility of single-point and multiple-probe average sampling. Aerodynamic pressure and total temperature probes were interspersed among the gas sampling

7

probes along the horizontal arm of the cruciform rake to provide spatial measurements from which static pressure, static temperature, and exhaust gas velocity profiles were inferred. These measurements were taken near the centerline path of the optical measurement systems and provided flow-field properties used in the analyses of the optical data.

Independent of exhaust emissions characterization, flight condition and engine performance parameters were monitored by test facility instrumentation. Data required for relating emissions measurements to test conditions and engine performance are provided in this report.

2.0 TEST FACILITY AND ENGINE PARAMETERS

This test program measured gaseous and particulate constituents exiting an engine with a 0.28-m² mixed flow exhaust nozzle area and an annular combustor representative of modern combustors in commercial use. The nozzle was slightly convergent-divergent with an exit radius of 30 cm. The fan (bypass) air for this engine was introduced in an annular flow surrounding the core flow upstream of the nozzle exit without forced mixing. The engine was operated from sea-level-static to 15.3-km altitude with a range of power settings from idle to takeoff. The engine cycle is representative of a commercial engine in the thrust category of 133–178 kN (30–40,000 lbf). The overall engine pressure ratio was approximately 30:1. The engine was tested at a flight Mach number near 0.8, except at the 7.6-km altitude condition where Mach number was set near 0.7. The aviation fuel is specified in the accompanying fuel analysis reports prepared by the AEDC Chemical Laboratory (Table 1) and the United States Air Force Aerospace Fuels Laboratory at Wright Patterson Air Force Base, OH (Table 2).

The test facility provided air directly to the engine inlet simulating total temperature and pressure conditions appropriate for the desired flight Mach number and altitude. This testing method is referred to as a direct-connect test configuration. The engine exhaust vented into a 1.66-m-diam diffuser connected to facility exhaust pumping stations (exhausters) that maintained simulated-altitude pressures within the test cell. The test cell was purged with air to assist engine cooling, sustain desired ambient pressure, and minimize recirculation of engine exhaust gases that could interfere with optical measurements near the engine exit. A 7.6-cm gap between the nozzle exit and the diffuser inlet allowed optical access to the exhaust flow field.

In order to protect the engine, true sea-level-static conditions are not simulated in altitude test facilities. The engine inlet total pressure and temperature conditions were consistent with sea-level-static operation, but the ambient test cell pressure was lower than one atmosphere, as noted by a 3.1-km altitude pressure in Table 3. For these inlet conditions, the engine performance, and thus exhaust emissions, should be representative of sea-level-static conditions and be fairly insensitive to the subatmospheric test cell pressure at the engine exit plane.

The test matrix was set by parametrically varying the combustor inlet temperature (T3) or combustor inlet pressure (P3) at simulated SLS and four other altitudes. The T3 and P3 values

8

reported herein are actually compressor discharge stagnation temperature and pressure measurements, but closely approximate combustor inlet conditions. Facility and engine parameters for steady-state operating conditions are summarized in Table 3. For convenience, test conditions are noted graphically on Fig. 1 as a function of combustor pressure and temperature and grouped according to altitude. Facility air was preconditioned to provide "standard-day" temperatures at the engine inlet for respective altitudes. Inlet air humidity, affected by the conditioning process, was monitored using a dew-point hygrometer and reported as dew-point temperature. Fuel/air ratios (by weight), determined from facility engine performance measurements, are given in Table 3 for both the hot core section and mixed hot core and fan bypass streams. The core fuel/air is the ratio of the fuel flow rate to the hot core flow rate, while the mixed fuel/air is the ratio of the fuel flow rate to the sum of the hot core and fan bypass air flow rates. Data presented in Table 3 were acquired during steady-state operation of the engine and test facility. Multiple data points acquired during steady-state conditions were relatively constant over time and were therefore averaged and reported as a single value. Clock times are included in the table to document the actual test sequence, relate approximate duration per steady-state test condition, and to correlate with data from other measurement systems.

3.0 EMISSIONS MEASUREMENT SYSTEMS

A suite of optical and extractive diagnostic instrumentation was assembled for the emissions characterization measurements study. These are listed in Table 4 and summarized below. Details of the respective techniques and applications to this test program are described in the appendices. Figure 2 illustrates relative measurement locations for the optical techniques and probes with respect to the inlet of the test cell diffuser. The shaded area on the rake assembly illustrates the extent of the engine nozzle exit area.

3.1 PROBE RAKE

A cruciform multi-point rake was used to obtain exhaust samples at individual and combined spatial locations allowing a mapping of exit plane core, bypass, and intermediate mixed flow regimes. The conceptual design of the rake is illustrated schematically in Appendix A along with probe design details. Two distinct bars mounted 90 deg apart formed a cross as illustrated in Fig. 2. One was mounted vertically and one horizontally with each completely spanning the exhaust flow field and beyond. The center of the rake, and thus the horizontal bar, was 2.54 cm above the centerline axis of the engine nozzle. The gas sampling probes were designed to meet emissions certification test requirements. Since this probe rake system was to eventually be used for multiple tests on various engine types, the gas sampling probes were spaced equally across the rake rather than at positions corresponding to centers of equal area of the exhaust. The gas sampling probes on each radial section of either bar could be "ganged" (valved to a common line) or sampled individually. Individual probe sampling allowed spatial mapping of the core, bypass, intermediate partially mixed flow regimes, and gas recirculation regions surrounding the exhaust. "Ganged" operation provided spatial averages for selected regions either within or external to the exhaust flow field. Ex-

9

ternal measurements quantified concentrations of gas recirculation constituents. The vertical bar contained only gas sampling probes. The horizontal bar of the rake assembly contained alternating Mach number/Flow Angularity (MFA), stagnation temperature, and gas sampling probes. Probes were amply spaced to minimize interferences of neighboring probe interactions with the flow field. The data from these probes were used to determine local static temperature, static pressure, and gas velocity distributions required to analyze optical data for determination of gaseous species concentrations and emission indices. The probe rake assembly was designed to withstand turbine engine exhaust conditions over the full range of engine power settings and altitudes specified for the test program. The probe rake assembly was mounted inside the test cell diffuser with the longer MFA probes extended upstream within 7.6 cm of the nozzle exit plane, thus providing optical access for non-intrusive diagnostics between the nozzle exit plane and probe rake assembly.

Two additional probes were mounted to the rake body near the center of the exhaust flow field to provide exhaust gas samples to a McDonnell Douglas CO_2 analyzer, discussed later, and an AEDC instrument not related to this measurement program. Sample lines for these probes were independent of the gas sample distribution system, and thus provided continuous samples to these analyzers with no impact on other AEDC and UMR measurement systems.

The test facility data acquisition systems collected data from the temperature, pressure, and MFA probes. These data were collected in conjunction with test facility transient and steady-state engine performance data. Multiple steady-state data points acquired during a steady-state engine condition were averaged and are reported in Appendix A for each engine condition described in Table 3.

3.2 GAS SAMPLING AND SMOKE

The gas sampling system is similar to systems used for commercial aircraft engine emissions certification testing, except for the effects of equally spaced sampling probes on spatial averages of the exhaust. Gas samples collected at the rake (12 cm downstream of the nozzle exit plane) were passed through heated lines to a sample distribution system that allowed any combination of probe samples to be directed to the gas analyzer systems. This allowed single- and multiple-point measurements within the exhaust flow field or recirculation region surrounding the exhaust flow field. As necessary during the test period, a stainless-steel metal bellows pump was valved in line between the sample distribution system and gas analyzers to raise the sample pressure slightly above atmospheric pressure, a requirement for gas analyzer operation.

A suite of analyzers was used to measure concentrations of gaseous constituents which are reported in percent or parts per million by volume, ppmv. Non-dispersive infrared analyzers (dry) were used to measure concentrations of CO and CO_2, a chemiluminescence analyzer (dry) for concentrations of NO, the same analyzer (dry) using an in-line catalytic converter for concentrations of NO_x, a flame ionization detector (wet) for concentrations of total hydrocarbons (THC), and a paramagnetic analyzer (dry) for oxygen. Dry indicates that the samples were passed through a gas

sample dryer before entering the analyzer. A cold mirror dew-point hygrometer was used for real-time monitoring of dryer efficiency. This hygrometer was independent of the one used to monitor the humidity of facility air supplied to the inlet of the engine.

The method of carbon balance was used to determine fuel/air ratio and combustion efficiency from the measured concentrations. This also produced estimates of exhaust H_2O and O_2. Thus, O_2 concentrations were both inferred from carbon balance and measured. Also, emission indices (defined as mass of constituent per 1000 pounds of fuel) were calculated and are presented for each gas sampling data point.

An SAE smoke meter was used for measurements of smoke and are reported as smoke number. However, due to lengthy sampling times (several minutes) required per smoke number measurement, only three were performed throughout the test period.

Data were obtained over the full set of test conditions at altitudes ranging from equivalent SLS to over 15 km and engine power levels from idle to takeoff. Spatial averages were obtained from combinations of sampling probes within the extent of the exhaust flow field: each radial arm of the horizontal and vertical bars, full horizontal and vertical bars, and the full cruciform (horizontal and vertical bar combined). Spatial profiles were obtained by sampling individual probes of each bar. Real-time comparisons of vertical and horizontal species concentration profiles and spatial averages early in the test period confirmed symmetry and gave confidence in representative sampling from either the horizontal or vertical bar. Thereafter, the horizontal bar was primarily assigned to the conventional gas sampling system which permitted more direct comparisons with data from non-intrusive optical techniques, while the vertical rake was assigned to the UMR-MASS (described below) for simultaneous particulate characterization. Sharing the rake in this manner substantially decreased data acquisition time per test condition and permitted data to be obtained at several test conditions that would not have been possible otherwise.

The complete set of emissions data obtained over the test period are presented in Appendix B along with corresponding engine performance data required for data analysis. These data will be summarized in Section 4.0.

3.3 OPTICAL NON-INTRUSIVE TECHNIQUES

Optical non-intrusive techniques provide measurements of gaseous species concentrations independent of extractive probe sampling methods and thus a means for comparison of these techniques. These optical techniques rely on a measure of spectral transmittance (of a known well-characterized radiation source) through the exhaust flow field and a characterization of the thermodynamic properties along the optical path. Radial profiles of static temperature, static pressure, and radial and axial components of flow velocities provide information for determination of the statistical population distribution of molecular energies, line broadening and shifting, and for the present data, mass flux for conversion of molecular densities to emission indices. These

11

properties were inferred from probe measurements as discussed earlier. Also, an analysis of optical transmittance data acquired at a single radial position requires an assumption on the spatial distribution of the species along the optical path, whereas radial inversion of measurements at multiple radial positions removes this requirement for radially symmetric flows.

The optical measurements were performed within the 7.6-cm gap between the engine nozzle exit and test cell diffuser. Figure 2 illustrates the optical beam paths relative to the entrance plane of the diffuser and approximate extent of the engine exhaust flow field.

Aerodyne Research, Inc. (ARI) used coincident infrared tunable diode laser (IR-TDL) beams for measurements of NO, NO_2, CO_2, and H_2O concentrations along an optical path through the center of the plume. The TDL system allowed simultaneous operation of two lasers with an option to switch one laser with a third. The interchange required only a few minutes, making data acquisition possible for all species during long duration steady-state engine test conditions, but restricting measurements to NO, H_2O, and NO_2 or CO_2 for many test conditions. Optical mirrors were used to guide the IR beam through an optical window into the test cell, along a purged path to the vicinity of the nozzle exit, across the exhaust flow field to a retro-reflector, and then trace a similar path back to the TDL system detectors. The optical window was calcium fluoride with a 1-deg wedge to suppress interference fringes. The spectral data, analysis process, and results are presented in Appendix D.

AEDC performed spectral UV absorption measurements using both NO-resonance and continuum lamps through several chords of the exhaust flow field and the surrounding recirculation gas region for determination of radial NO number density profiles. As illustrated in Fig. 2, optical fibers were used to conveniently transmit lamp radiation into the test cell and back out to the spectrometer/detector for each system. Inside the test cell, radiation exiting a lamp fiber was collimated, transmitted across the exhaust flow field to a mirror, and reflected back through the exhaust to the spectrometer/detector fiber. Line-of-sight (LOS) measurements at multiple radial positions were performed using slide tables to traverse the optical beam from the purged tube position to the centerline of the exhaust flow field. This provided spectral transmittance measurements at radial positions within the exhaust and surrounding gas-recirculation region for each engine test condition. A line-by-line radiative transfer model, calibrated and verified by laboratory measurements, was used to relate measured transmittances at the second bandhead of the NO gamma (0,0) band to NO number density. An "onion peel" radial inversion technique was used in conjunction with the radiative transfer model to determine radial NO number density profiles from the measured radial transmittance profiles. This provided a measure of NO density in the gas-recirculation region surrounding the exhaust flow field, and thus self-corrected for molecular NO absorption along LOS optical paths outside the exhaust flow field. Radial profiles of number density (cm^{-3}) were converted to profiles of fractional concentration (ppmv) and to NO emission indices. These data and processes are presented in Appendix C.

12

Additionally, AEDC used a frequency-scanned UV-laser system for measurements of OH number density along a fixed optical path, as illustrated in Fig. 2. The laser beam was transmitted into the test cell through a single-mode optical fiber. On exiting the fiber, the beam was split with a portion directed to a reference detector and the remainder directed through the exhaust flow field to the OH absorption detector. The resolution of the laser system allowed spectral detail of single OH absorption lines. These data are presented in Appendix F.

Comprehensive data are given in respective Appendices for each optical technique. The emission indices for NO are summarized in Section 4.2 and compared to probe sampling data.

3.4 PARTICULATES AND AEROSOLS

Appendix E contains details on the particulate and aerosol characterization system employed in this study—the University of Missouri-Rolla Mobile Aerosol Sampling System (MASS). A brief overview of the system is given here. For this test, the MASS was divided into two work stations. The first, located close to the extractive sampling probe selection manifolds, was used in conjunction with the extractive sampling system to acquire total condensation nuclei (CN) concentrations for all aerosols in real time and to fill and pressurize sample tanks. Exhaust samples were delivered to the MASS from individual and ganged (multiple) probe sources. An isobaric cooler for supersaturation pulse simulation, a laser aerosol spectrometer for real-time large diameter aerosol measurements (diameters from 1.0 to 30 (μm)), and a needle-to-grid electric precipitator for aerosol collection on electron microscope grids, were also located at the first work station. The second work station consisted of two Electrostatic Aerosol Classifiers (EAC's) configured in series. With this system the tank samples taken at the first work station were analyzed for size distribution and growth and/or hydration (critical supersaturation) information for aerosols in the submicron range, 10 nm to 500 nm. Comprehensive data presented in Appendix E are summarized in Section 4.3.

4.0 SUMMARY OF RESULTS

As mentioned earlier, the engine had a mixed flow exhaust with the hot core and fan bypass air exiting the same tailpipe. The degree of mixing of the two flow streams was not known before the test. Table 5 summarizes the data obtained from each of the conventional extractive gas analyzers at each engine set point. The gas sampling data presented in the summary table are spatial averages measured on the horizontal bar of the rake system, which more directly compare to optical measurements. The summarized MASS data are typical of particle and aerosol emission measurements for each engine condition and were obtained primarily on the vertical bar of the rake assembly. This section of the report provides an overview of the results. The reader, again, is directed to respective appendices for more complete data and detailed discussions.

13

4.1 GAS SAMPLING DATA

Figure 3 shows the spatial CO_2 concentration (percent by volume) distribution measured at individual probes along the horizontal bar for T3 = 733 K at the 9.1-km altitude, a condition typical for an engine on a commercial aircraft operating at cruise conditions. Radial positions are normalized to the nozzle exit radius, Re = 30 cm, so that the nozzle centerline is located at R/Re = 0. The fuel burned on a molar basis is the sum of the moles of the species containing all of the carbon atoms. Thus, neglecting carbon emitted in the form of particulates and trace chemical species, the CO_2 concentration is directly related to the local fuel/air ratio. As indicated in Fig. 3, CO_2 concentrations are high over the central region of the exhaust, comprised mainly of hot core flow, and drop off toward the outside where the fan air mixes with the core flow. At the outer edges of the exhaust, the flow is predominantly cooler fan bypass air. This is consistent with what one expects for a mixed flow exhaust with no forced mixing. The slight decrease in CO_2 at the center of the flow is expected based on the thermal design profile of the combustor exit. The radial profile data from the horizontal bar show good spatial symmetry about the centerline of the nozzle.

Figure 4 is the corresponding NO concentration profile for the same engine condition. The shape is similar to the CO_2 profile and again exhibiting good radial symmetry. The NO emission index, EI(NO), is proportional to the ratio of the NO concentration and fuel flow rate (CO_2 concentration). The radial profile of EI(NO), reported as NO_2, is presented in Fig. 5. The EI(NO) profile is flat across the entire radial extent of the exhaust. This behavior is consistent with a uniform engine core flow. Most of the variation in both NO and CO_2 concentration profiles is toward the outermost regions of the tailpipe radius, and this variation is attributed to dilution of the core flow with fan bypass air. The limited scatter exhibited in the data indicates that both the engine and gas sampling system were stable and did not exhibit temporal variations for the duration of an engine test condition period. This stability was further substantiated by small variations in repeated data points during selected engine test conditions throughout the test program.

The gas sampling profile data obtained on the horizontal and vertical bars for this and other engine test conditions are presented in Appendix B. Profiles for each constituent measured by the gas sampling system were radially symmetric and well behaved. This indicates that the gas sampling data could serve as a valid reference for comparisons of the species concentrations determined from optical techniques.

Fuel/air ratios (by weight) were calculated for each gas sample data point using the method of carbon balance. The fuel carbon-to-hydrogen ratio used in the calculations was obtained from the fuel analysis. The sampling (carbon balance) fuel/air ratios are given in Table 5 for horizontal bar averages corresponding to each test condition, and are compared to the engine performance core and mixed fuel/air ratios in Fig. 6. As expected, the sample fuel/air ratios are lower than the core

fuel/air and greater than mixed fuel/air ratios. A sampling bar with equally spaced probes (rather than at positions of equal area) across the extent of the exhaust of a mixed flow engine should give a fuel/air ratio lower than the core fuel/air ratio due to sampling of some fan bypass air. Also, the sampling fuel/air ratio should be higher than the fully mixed fuel/air ratio since the equally spaced samples bias the average toward the core. The sampling fuel/air ratios do fall closer to the core fuel/ air than the fully mixed fuel/air. Figure 6 comparisons again indicate that the engine and instrumentation operated in a consistent manner throughout the test period.

Figure 7 summarizes EI(NO) versus combustor inlet temperature (T3) for all test conditions, again presenting only horizontal bar averages. Of interest is the variation of EI(NO) as a function of altitude. At each altitude, the EI(NO) increases monotonically with increasing T3, while for any given T3, EI(NO) decreases with increasing altitude (decreasing P3). Figure 8 shows the pressure effect on EI(NO) for lines of constant T3. Preliminary curve fits of these data indicate that at constant T3, EI(NO) varies as P3 raised to a power in the range of 0.3 to 0.5. These trends are consistent with existing correlations based on theoretical and rig data measured on other test programs.

Figure 9 is a correlation of NO_x versus NO concentrations for all engine test conditions. Variation in the concentration ratio NO/NO_x is small. For all data measured, NO concentrations were on average 93 percent of the NO_x. It should be noted here that while both NO and NO_x were measured by the same instrument, measurements were always sequential and the sample passed through a catalytic converter for measurements of NO_x. The small amount of scatter about the linear curve fit of the data shown in Fig. 9 is indicative of the high level of engine and instrumentation stability at each engine test condition.

The International Civil Aviation Organization (ICAO) requires, for purposes of regulatory compliance of commercial engines, the measurement and reporting of gaseous pollutants in terms of D_p/F_{00}. The proper calculation and parameters involved are described in Volume II of the International Standards and Recommended Practices, "Environmental Protection," Annex 16 to the Convention of International Civil Aviation. D_p is the mass of the gaseous pollutant emitted during the reference emissions landing and take-off (LTO) cycle. F_{00} is the maximum power/ thrust available for take-off under normal operating conditions at International Standard Atmosphere (as defined in the manual, Document 7488) SLS conditions. These are the atmospheric conditions to which all engine performance data should be corrected. The sea-level-static NO_x data were corrected to Annex 16 reference specifications and applied to the performance conditions and LTO cycle of a midsize commercial engine of the 133-kN (30,000 lbf) thrust class. The subsequently calculated NO_x D_p/F_{00} for a one engine characteristic value (g/kN) is shown in Fig. 10 in relation to other late model engines. This calculation was for a pseudo-comparison of this engine with other engines operating in the current fleet. Data for a true D_p/F_{00} were beyond the scope of this test program.

Figure 11 shows EI(CO) determined from horizontal bar measurements of CO concentrations for all engine test conditions. The EI(CO) levels are highest for idle and off-idle engine power settings, represented by the lowest T3 values in the figure. Except for the idle conditions, EI(CO) levels were very low. For fixed T3 settings, EI(CO) appears to increase with altitude which is especially evident from data at the highest altitude (15.2 km).

Figure 12 summarizes the EI(THC) for all engine test conditions. In general the data are within the zero scatter (range of readings for clean air) of the instrument. At the lowest T3 there is an indication that EI(THC) increased slightly, but the concentration levels were too low to make definitive statements.

The smoke meter, recommended by SAE, was used to measure smoke from the engine during three high power points. The data are presented in the summary sheet, Table 5. Smoke was basically not measurable. All smoke numbers were less than 1.5, which is within the zero scatter (range of readings for clean air) of this technique.

4.2 COMPARISON OF OPTICAL AND GAS SAMPLING DATA

Species number densities, and subsequently concentrations, were deduced from the optical technique measurements. Thermodynamic properties along the optical paths were provided by probe measurements as discussed earlier. Further, emission indices were determined for respective species concentrations using exhaust velocity profiles inferred from probe measurements and fuel flow rates from test facility engine performance data.

UV resonance and continuum absorption measurements were performed at all engine test conditions. The resonance absorption system provided a measure of NO density over the full range of test conditions, whereas the less sensitive continuum system did not exhibit absorption features at test conditions with lowest NO concentrations. Preliminary analysis of the continuum absorption data indicated general agreement with resonance absorption results, but greater uncertainty. A complete analysis of the continuum absorption data will be published at a later date. The following discussions will be restricted to UV resonance absorption data.

UV resonance absorption measurements at multiple lines of sight allowed NO density determination without assuming spatial NO concentration profiles before the analysis. Radial inversions performed on the optical UV measurements through several chords of the exhaust flow and surrounding recirculation gas gave radial NO number density (cm^{-3}) profiles for each engine test condition. For more direct comparisons with the gas sampling data profiles, these densities were converted to volumetric fractions (ppmv) using static flow-field properties inferred from probe rake data and the ideal gas law. Comparisons with probe sampling data (Appendix C) show that NO concentration profiles determined by UV measurements within the exhaust region are similar in shape but with somewhat lower peak levels. Greatest differences were observed at simulated sea-level-static engine test conditions. UV and probe sampling NO concentrations agreed well for the gas-recirculation

region, both showing appreciably greater NO concentrations (relative to exhaust levels) for the sea-level-static condition.

NO-UV concentration profile comparisons were limited to the few test conditions for which probe sampling radial profile data were available. For comparisons over all engine test conditions, emission indices were calculated from NO-UV resonance absorption concentration profiles using exhaust flow velocity profiles derived from the rake data and fuel flow rates measured by test facility instrumentation. EI(NO) data, reported as equivalent NO_2, are presented in Table 5. UV EI(NO) data are in good agreement with probe sampling data, matching well within respective uncertainty bands. However, NO-UV EI(NO) tended to be lower (but not consistently) throughout the test period.

An engineering statistical analysis process was applied to determine confidence bands with respect to measurement precision. The variance-covariance matrix developed for a set of radial profile transmittances took into account codependency on lamp reference spectra, curve-fit correction factors, and the linear smoothing algorithm. This process produced one-sigma variances for NO number density at each radial location per set of data. Overall, uncertainty in NO number density per radial location for several test conditions investigated ranged from ±6 to ±18 percent, with the greater uncertainties observed for data acquired during higher engine power settings at the simulated SLS condition. Statistical uncertainty at radial positions in the surrounding gas-recirculation region ranged from ±15 to ±25 percent. Extending the statistical analysis to emission indices calculations, uncertainty ranged from ±7 to ±13 percent when not accounting for uncertainty in exhaust radial velocity profiles. It should be noted that absorption in the (0,0) band was fairly insensitive to static temperature and pressure, and thus contributed little to the uncertainty in NO number density. However, uncertainty in velocity, especially near the outer edge where abrupt changes were not quantifiable from the sparse rake measurements, increased the reported uncertainty in emission indices.

This test program has provided the first comprehensive set of simultaneous UV resonance absorption and probe sampling data for direct comparisons of NO concentrations since extensive studies performed in the late 1970's. The results reported here substantiate for a wide range of engine exhaust conditions that agreement will be achieved if probes are designed properly for the exhaust flow-field conditions, and proper measurement procedures are followed. Additionally, UV resonance absorption measurements performed in this test program demonstrate the maturity and robustness of this measurement system for turbine exhaust applications in harsh environments of altitude engine test facilities. Also, the use of fiber optics, a relatively simple traversing system, and linear array detectors significantly decreases the system complexity and increases system reliability for measurement applications.

The NO emission index values, given in Table 5 for the three techniques, IR, UV, and gas sampling, are plotted in Figs. 13 through 17 for respective altitudes and displayed as functions of combustor inlet temperature, T3. (In these figures, the dotted lines simply serve to connect points

17

and indicate changes in ordering of the three values.) The considerations involved in assigning uncertainty bars for each diagnostic technique are discussed in the appendices devoted to each measurement method. The widths of the uncertainty bar caps on the plots are different to help distinguish which uncertainty applies to each technique: the width is least for the gas sampling EI(NO), and largest for the IR diode laser absorption EI(NO).

All three techniques display similar trends and agree within their uncertainty limits. No systematic ordering among the values from the three methods is seen, even at levels within the error limits. In Fig. 14, EI(NO) for the higher engine power points in the sampling data set at 7.6 km seem to have unresolvable issues and have been omitted. As discussed in detail in the appendices, both spectroscopic methods derive emission indices from computations of mass fluxes of the chemical species of interest, a computation that required exhaust flow properties obtained from probe rake measurements. There is the potential for systematic errors in these conversions of number densities to emission indices, which might apply more or less equally over an entire altitude data set. It can be seen from an examination of the full IR diode laser absorption data set in Appendix D that in addition to the agreement with NO measurement techniques, neither the H_2O nor the CO_2 emission indices are systematically lower or higher than their theoretical values. The largest differences appear in the comparison of NO_2 values, to which we now turn.

Nitrogen species other than NO and NO_x were not measured by the extractive gas analysis (sampling) system. The probe sampling values for NO_2 concentrations, and thus EI(NO_2), were derived from the difference of NO and NO_x measurements with an implied assumption that no other nitrogen oxide species contribute to the NO_x measurement. On the other hand, measurements of NO_2 concentrations by IR-TDL absorption are direct and no inferences are required. However, as discussed in detail in Appendix C, the spectral region for this measurement has NO_2 and H_2O lines that are overlapped, such that a direct determination of the baseline (zero absorption) is not possible. Therefore, uncertainties may be large for IR measurements of NO_2 concentrations as well. IR measurements of NO_2 were made at only six engine test conditions, whereas the sampling measurements provide EI(NO_2) values for almost the entire range of engine conditions. A quantity that is expected to more directly correlate with engine conditions is the ratio of EI(NO_2) to total EI(NO_x). However, even for this ratio, variations between altitude data sets are such that at present the clearest trend is seen by plotting data for all altitudes and looking at the ratio as a function of T3. This plot, presented in Fig. 18, shows the NO_2 fractions for all but idle (lowest T3) conditions to be grouped around a canonical value of 0.1, with NO_2 at idle being substantially larger. Ratios between comparable cases for IR and sampling measurements range from 1 to 3. Ratios of absolute EI(NO_2) determined from IR and probe sampling measurements for the three lower altitudes with T3 = 733 K are 1.34, 1.23, and 1.03, agreeing well within the uncertainty limits. For two 15.2-km cases, the IR/sampling ratios of EI(NO_2) are 2 and 3, and for the 9.1-km idle case (where large differences exist for other species), the ratio is 2.5.

An important aspect is the first-time demonstration of the viability of the IR-TDL technique to obtain high-precision, high-resolution infrared absorption spectral measurements of an aircraft

engine exhaust over an extensive test period. Prior to the application of this technique to an earlier AEDC test, there was concern as to whether plume effects on the laser beam would allow measurements at all. Prior to the present test, it was still not certain that optical surfaces inside the test cell would remain clean and properly aligned. The harsh optical environment (including water spray, oil fumes, and high vibration and noise levels in the test cell) was not detrimental to providing quality measurements throughout the entire test period.

The viability of the TDL technique for exhaust measurements demonstrated in this test program means that it can be further developed to give high-sensitivity measurements of concentrations of a wide variety of trace (and major) species, some of which have yet to be measured in exhausts by any technique. As implemented in this test, its ability to produce quantitative values for exhaust species concentrations and emission indices is dependent on characterization of the optical path plume properties provided by other independent measurements, such as the probe rake measurements of temperature, pressure, and velocity. Other implementations of the TDL technique are possible, such as the use of multiple lines of sight (as was done with the UV measurements of NO), multiple absorption lines of a single chemical species to determine temperature, and the possibility of choosing lines of trace and major species with the same dependency on temperature and pressure, so that trace species emission measurements could be self-referencing in the way that sampling measurements now determine EI(NO) and EI(NO_x) by referencing to measured CO_2 concentrations.

The OH laser absorption instrumentation performed well throughout the test period. The laser system was isolated from the direct noise and vibration of the test cell by using a 30-m fiber optic cable to locate the laser in the basement of the test facility. The detectors and optics mounted inside the test cell survived the harsh test environment. The exhaust OH concentrations, however, were below the lowest detectable concentration for the exhaust conditions, 10^{12} cm^{-3}. The laser was tuned to several OH lines throughout the test period, but spectral absorption features were never observed. Throughout the test period, the laser beam was intermittently redirected through a discharge lamp containing OH, which verified functionality of the system and ensured that the spectral scanning range was tuned to an OH line. Even though OH was not quantified, an upper limit concentration was determined.

4.3 PARTICULATE AND AEROSOL CHARACTERIZATION

The UMR MASS was employed to characterize the aerosol emissions over the range of engine flight conditions described in this report. These data characterize the aerosol generated in the engine and that continued to exist at a distance of 12 cm downstream of the exit plane of the engine exhaust nozzle. This is the first database of its kind and provides particulate characterization (i.e., total concentration, aerosol, number- and mass-based emission indices, aerosol (soot) volume fraction, total aerosol and non-volatile aerosol size distributions and hydration (soluble mass fraction)) for such a cruise simulation. Using calculation techniques discussed in Appendix E, the mean aerosol number-based emission index calculated from all measurements is $(2.2 \pm 0.7) \times 10^{15}$;

the associated mean mass-based emission index is 0.012 ± 0.001, (where the quoted uncertainty in both cases is the standard deviation of the mean). There is no strong correlation between emission index and thrust (measured as CO_2 concentration), altitude or combustor inlet temperature (T3) and pressure (P3). However, there appears to be a correlation between combustion efficiency and aerosol emission index observed from the ground idle data points, where elevated emission indices for aerosols, CO, and unburned hydrocarbons are recorded. The particle concentrations and emission indices measured in this test program were small compared with those measured on other aircraft engines using the UMR MASS. This correlates well with the extremely small smoke numbers reported in this study. Typical size distributions are log-normal and peak in the vicinity of 20- to 40-nm diameter. The volatile component of the aerosol is measured to be small and in most cases can be considered negligible. Most of the ground testing to date using the MASS approach has shown similar log-normal distributions and small volatile components for a range of current engine configurations. A review of the soot inception literature indicates that aggregates of individual soot spheroids are usually found in probe-collected samples; it is generally assumed that the aggregates are formed during combustion as well. Electron micrographs of particles, which we have sampled by electroscopic precipitation from other combustion sources, do show aggregate character, with fractal dimension varying with combustion conditions. This characteristic of exhaust particle morphology warrants further study since it can influence the particulate's evolution in the atmosphere. A research project in which the MASS approach is combined with electron microscopy and optical analysis of soot particles extracted from the primary combustion zones of laboratory flames would yield insight on the nature and influence of soot morphology in engine particulate emission characterization.

A complete listing of the particulate characterization data on which this summary of results is based can be found in Appendix E.

As part of the aerosol measurement component of this project, a CO_2 detector designed and constructed by McDonnell Douglas was evaluated. The results were in excellent agreement with the AEDC gas sampling data, and the device will be used in conjunction with the UMR MASS for determination of emission indices directly in future ground tests.

5.0 CONCLUSIONS

This measurement program produced a comprehensive set of data that provides measurements of gaseous and particulate emissions at simulated sea-level-static and altitude conditions including cruise operation. This database can be used for atmospheric assessment studies, comparison of optical (IR and UV) non-intrusive diagnostics and conventional extractive gas sampling methods, and parametric measurements for SLS to altitude extrapolation studies.

Data from the gas sampling system indicated trends with parametric variation in combustor inlet pressure and temperature as expected. Most variations observed in the spatial emissions distributions were in the outer regions of the exhaust flow and result from fan bypass air mixing

with the engine core air stream. The emission indices showed little spatial variation. The gas sampling data should serve as a good reference data set for evaluation of the innovative optical techniques, also applied as a part of this test program.

The optical line-of-sight non-intrusive techniques provided chemical species concentration measurements independent of the probe sampling measurements. Overall agreement of the data collected from these independent measurement systems throughout the test period substantiates accuracy within respective uncertainty limits. Additionally, highly repeatable measurements during steady-state test conditions from all measurement systems provide evidence of engine operation stability, spatial uniformity, and radial symmetry of the exhaust.

The IR-TDL system performed reliably throughout the test period, providing a large body of data on NO, NO_2, CO_2, and H_2O concentrations. The method used to interpret observed infrared absorption optical depths (using a model of the single nonuniform line of sight) produced trace species emission index values that agree with the other measurement techniques to within expected uncertainty limits, as well as major species emission indices that agree with theoretical values within similar limits.

The NO-UV resonance absorption technique with multiple LOS measurements across the exhaust flow field provided radial profiles of NO concentrations slightly lower but in good agreement with radial profiles measured using single-point probe sampling. Agreement was achieved even in the surrounding gas-recirculation region. Emission indices agreed over all test conditions, well within uncertainty limits for respective measurement techniques.

Attempts at direct measurements of OH concentrations were unsuccessful due to nozzle exit OH concentrations below 10^{12} cm^{-3}, the detectable limit for the laser system as configured for these test programs. However, this measurement establishes an upper bound on OH concentration for these tests which is important information for near-field plume interaction studies. Also, since accurate OH concentration prediction models are not available, these results provide design criteria for developing accurate chemical mechanisms for OH production in turbine engine exhausts and designing experimental simulations of these environments.

It is important to note that each optical measurement syst. m produced precise and repeatable spectral data; individually predicted overall consistent trends; and agreed within stated uncertainties of each instrument and probe sampling technique. Although the uncertainties were reasonably low, the greatest uncertainty contribution was attributed to the characterization of the optical path properties required to deduce densities and emission indices for respective species.

The following major conclusions can be deduced from the aerosol characterization data. The engine studied in this test is representative of most of the engines characterized in ground tests, to date, with this approach. Namely, the nature of the size distributions, being log-normal, is typical, as is the mean size of the distribution and its width. The third parameter characterizing a log-normal

21

distribution, the total number of particles, is the lowest measured for any engine characterized to date. The similar result for smoke number measured for this engine suggests a correlation exists between smoke number and particle emission index, at least in the case where these numbers are small. In addition, the volatile component of the particles is small. This is also consistent for other ground-based measurements where the sampling probe was located less than 1 m from the exit plane of the exhaust nozzle.

The particle emission indices were not determined to be strongly dependent on either fuel/air ratio (as measured by CO_2 concentration), altitude, or combustor inlet pressure or temperature. Based on the limited data set for the ground idle condition, where the engine combustion efficiency is at its lowest, there appears to be an inverse relationship between the particle emission index and combustion efficiency. The implications of this result with respect to our understanding of particle production as a function of engine performance warrant further investigation. The apparent absence of aggregates in the particulate emissions detected with the MASS raises interesting and critical questions with respect to our understanding of the soot formation process and/or the ability of the MASS methodology to account for their presence.

Overall, this emission test program exceeded expectations in the quantity of data and engine test conditions achieved for the limited test period. The test demonstrated the viability of several diagnostic techniques to characterize critical emissions parameters of interest and thus provid. comprehensive set of turbine emissions data to the scientific community for aviation impact assessments on atmospheric chemistry. Further measurement programs will be required to develop a comprehensive database spanning all classes of engines in current and future aviation fleets.
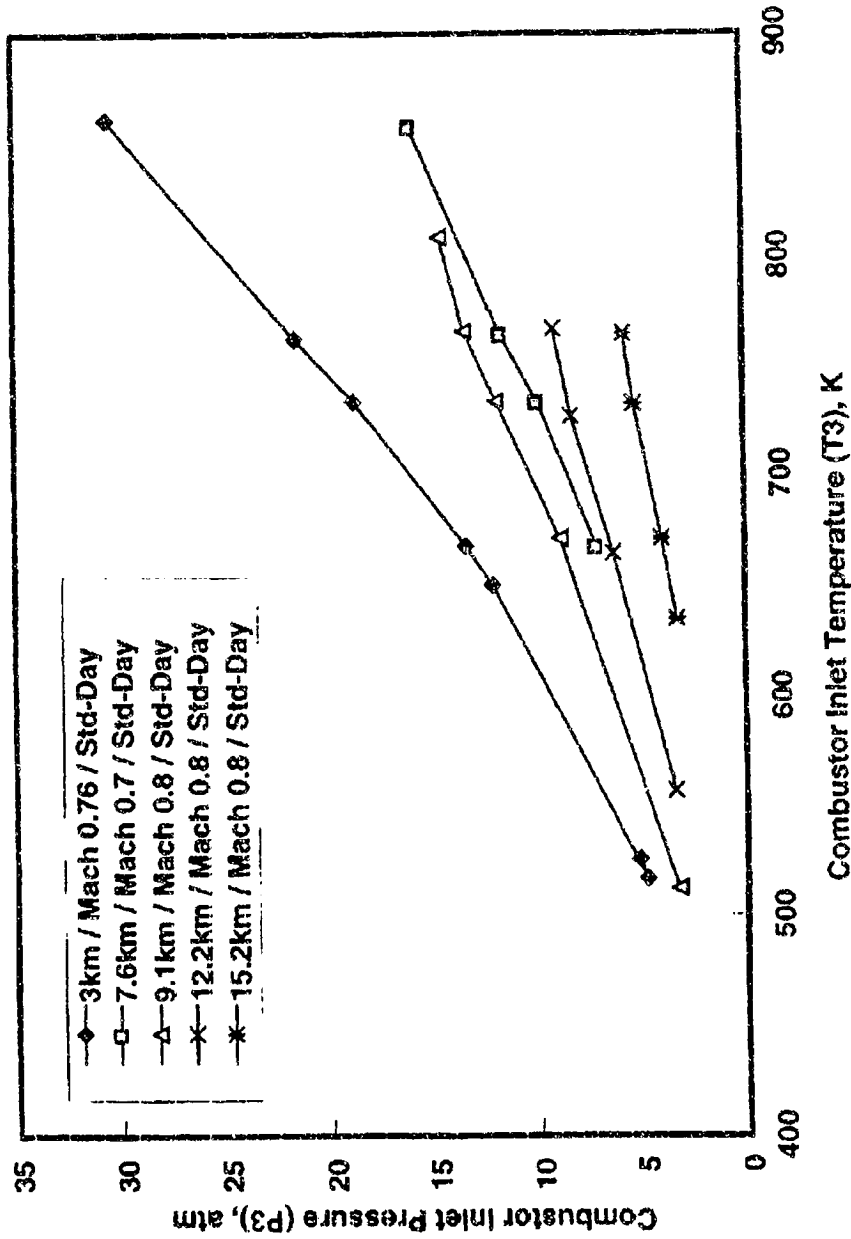
Figure 1. Combustor inlet pressure versus temperature for all test conditions.

Legend:
- 3km / Mach 0.76 / Std-Day
- 7.6km / Mach 0.7 / Std-Day
- 9.1km / Mach 0.8 / Std-Day
- 12.2km / Mach 0.8 / Std-Day
- 15.2km / Mach 0.8 / Std-Day

Combustor Inlet Temperature (T3), K

Combustor Inlet Pressure (P3), atm
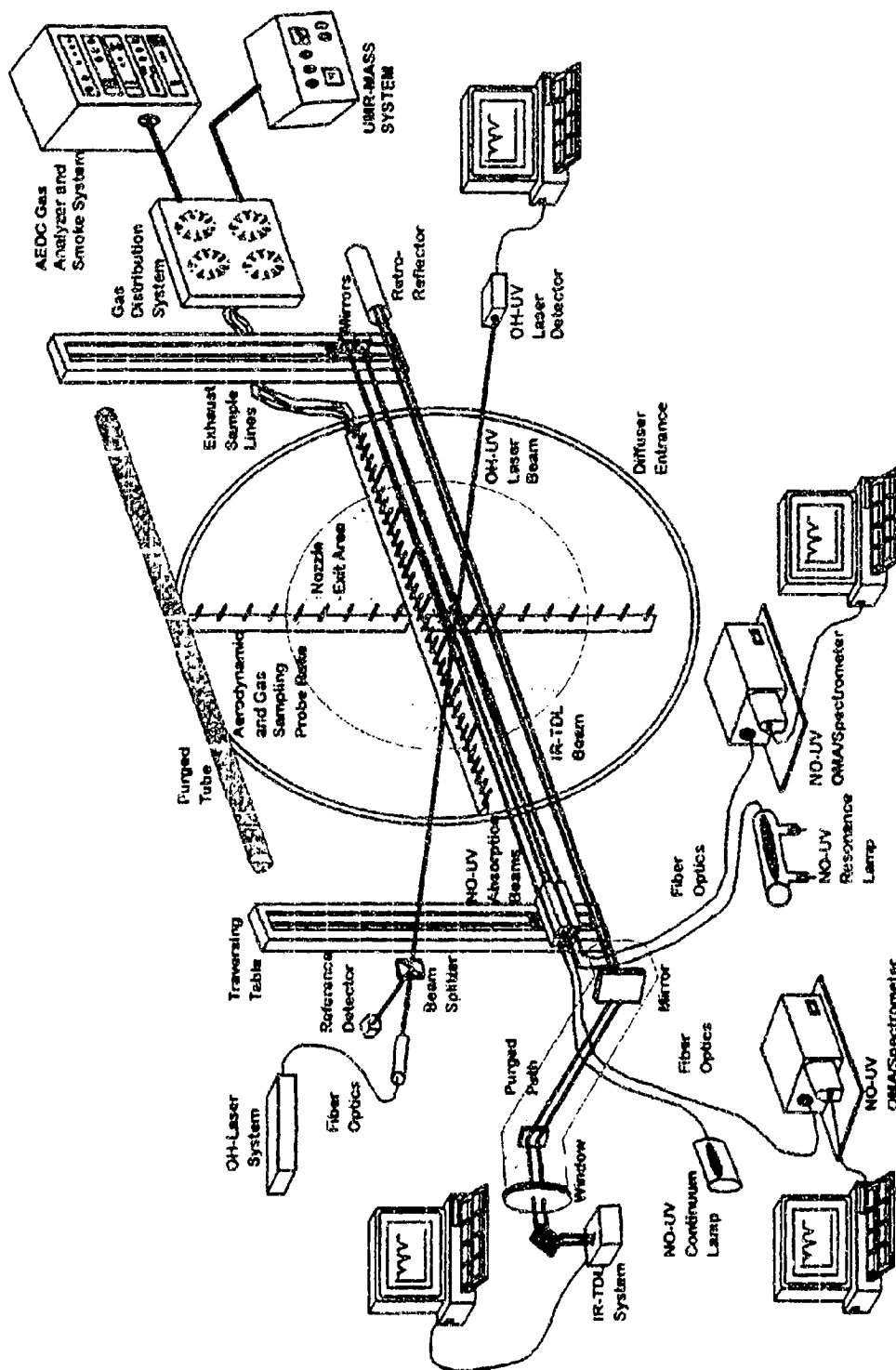
Figure 2. Turbine engine exhaust emissions measurements illustration.

24
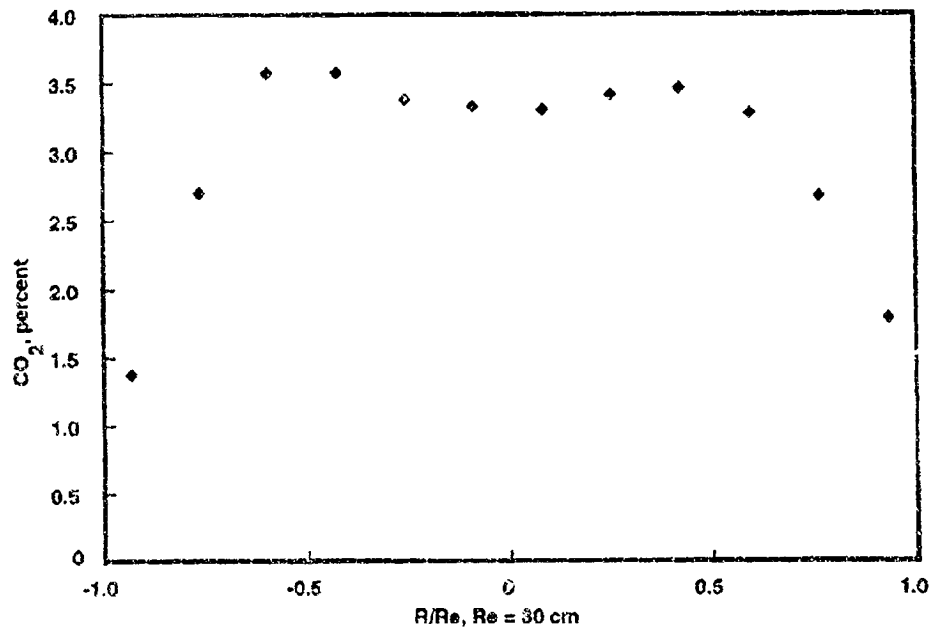
Figure 3. Horizontal CO_2 profile for T3 = 733 K at 9.1-km altitude.
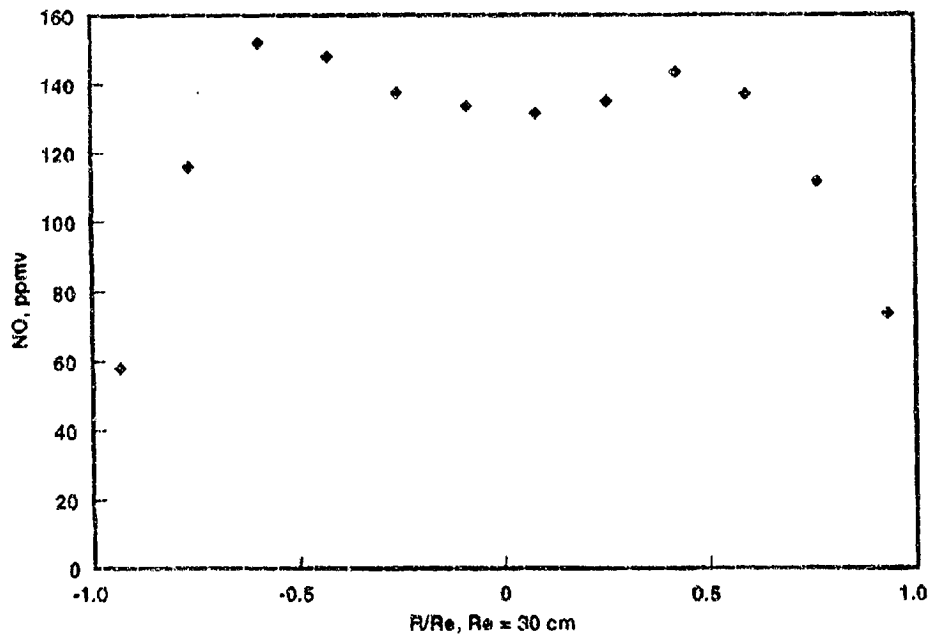
Figure 4. Horizontal NO profile for T3 = 733 K at 9.1-km altitude.
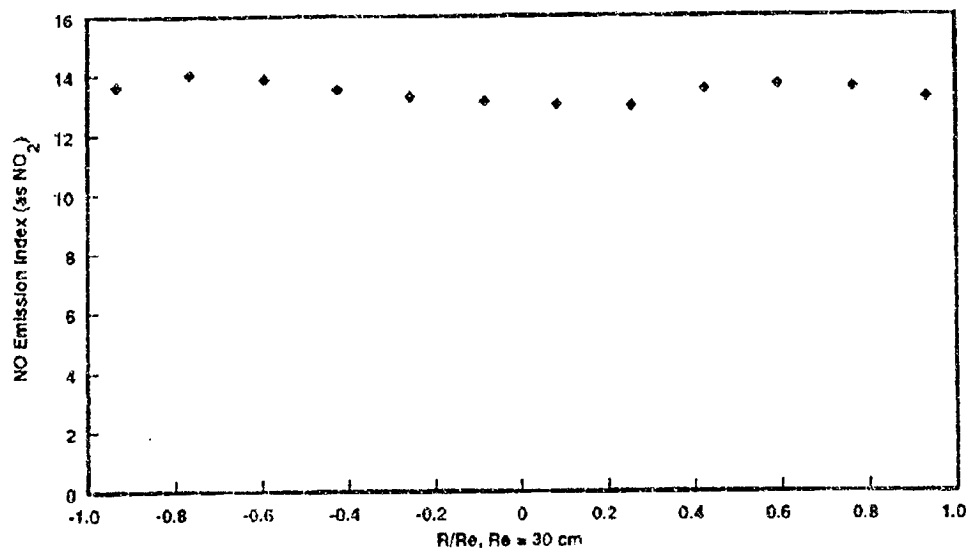
Figure 5. Horizontal EI(NO) profile for T3 = 733 K at 9.1-km altitude.
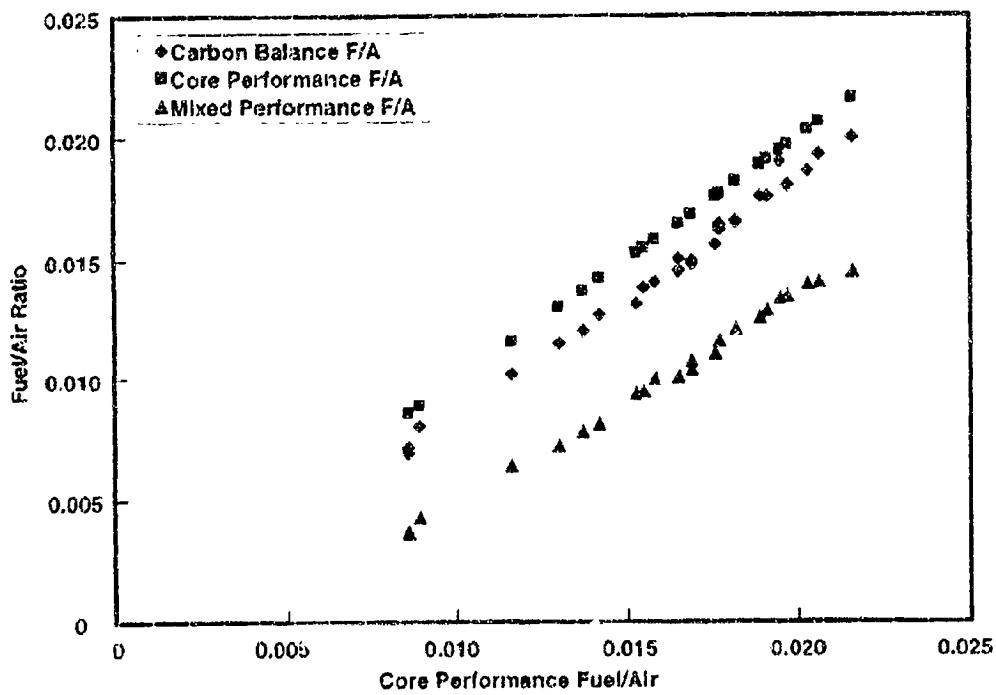
Figure 6. Horizontal bar fuel/air ratio summary.

26
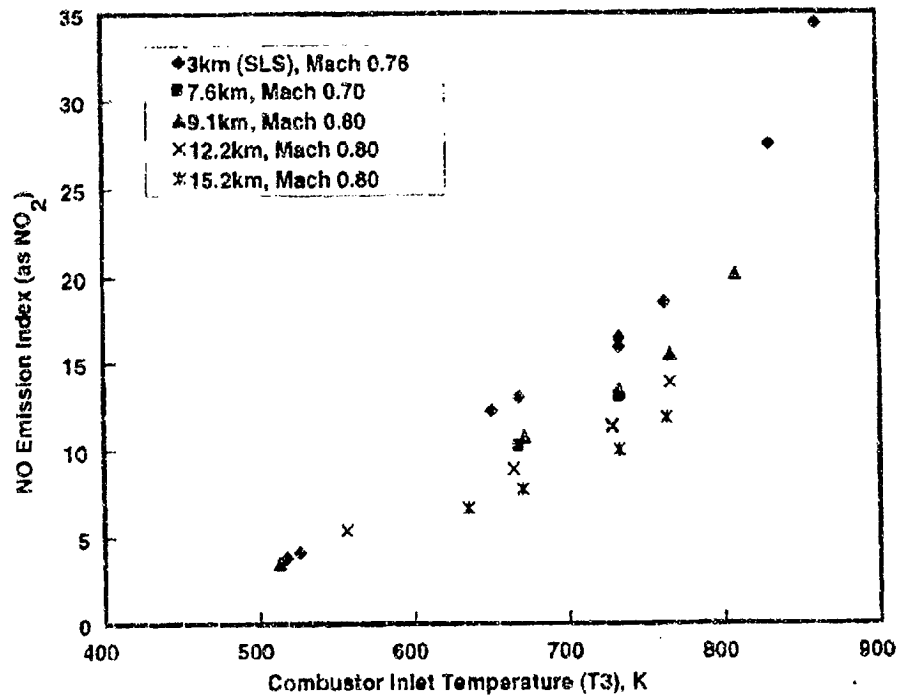
Figure 7. Horizontal bar EI(NO), as NO_2, summary for all test conditions.
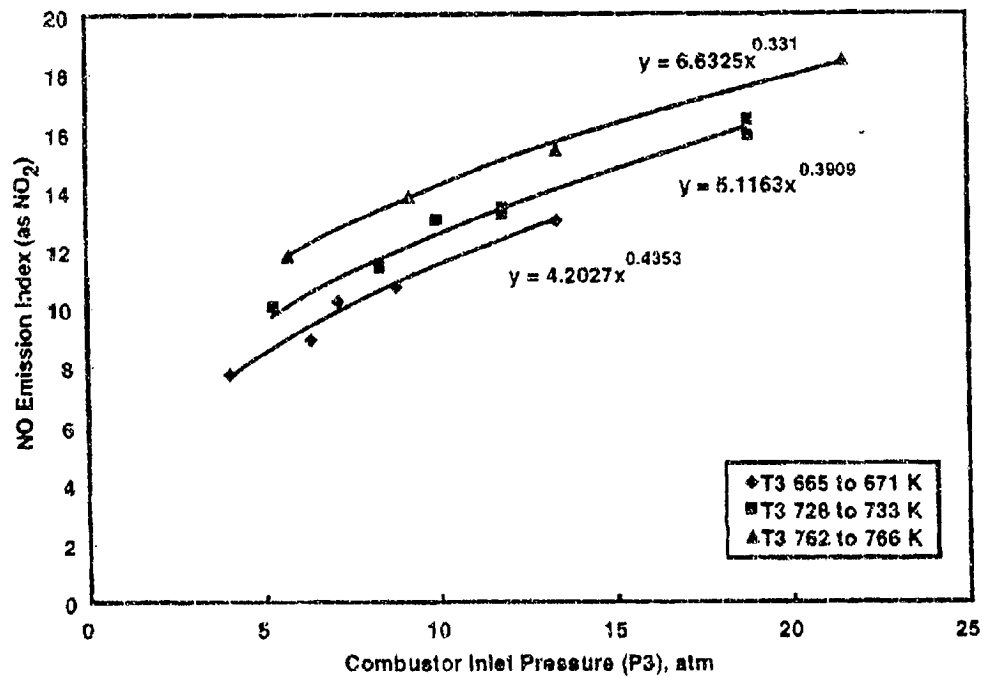
Figure 8. Pressure effect on EI(NO).

27
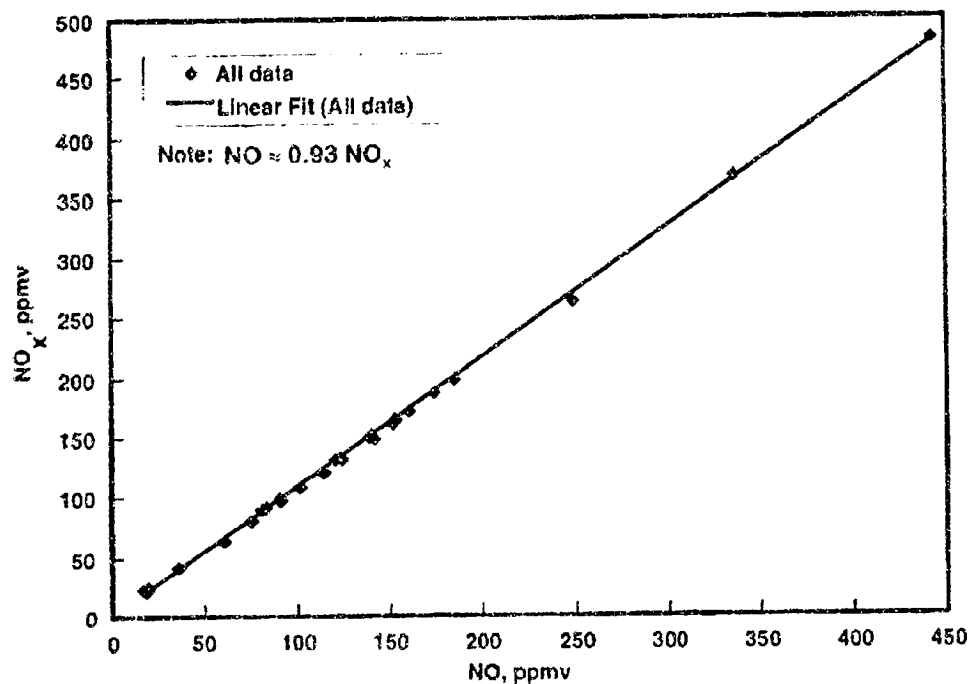
Figure 9. Horizontal bar NO_x versus NO.
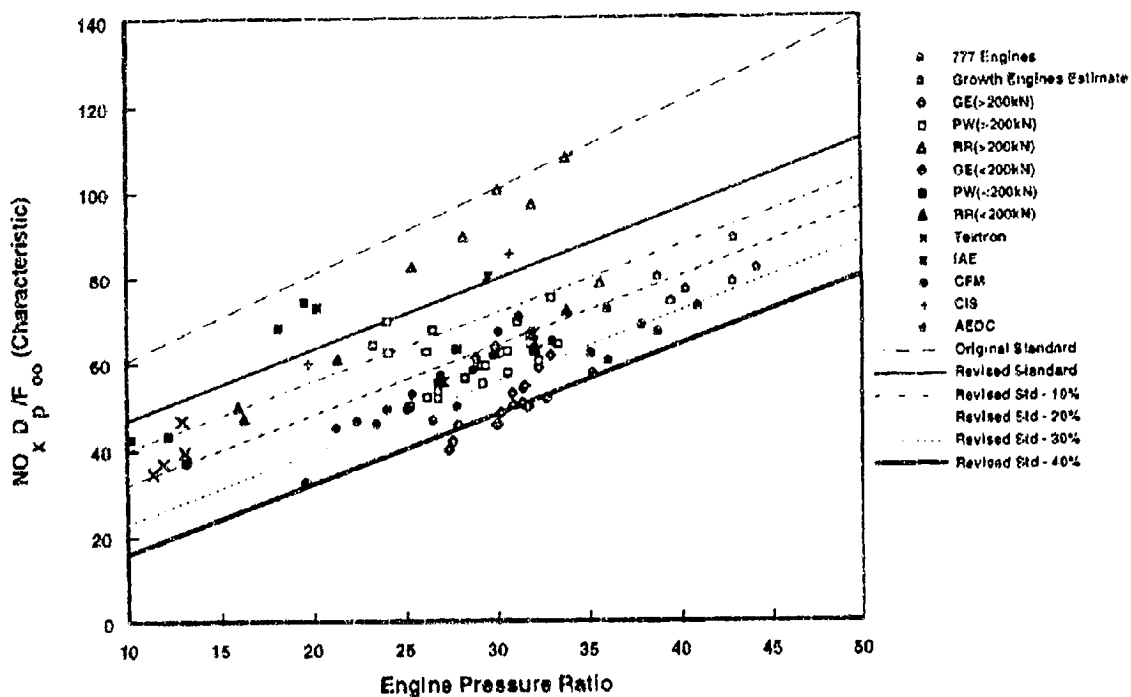
Figure 10. NO_x D_p/F_{oo} versus engine pressure ratio for late models (1980 and later).

28
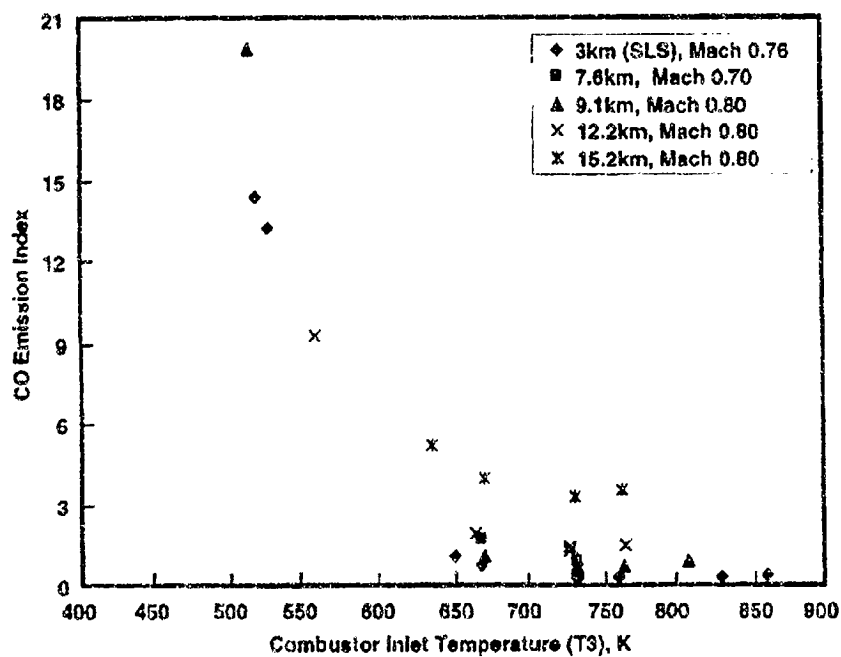
Figure 11. Horizontal bar EI(CO) summary for all test conditions.
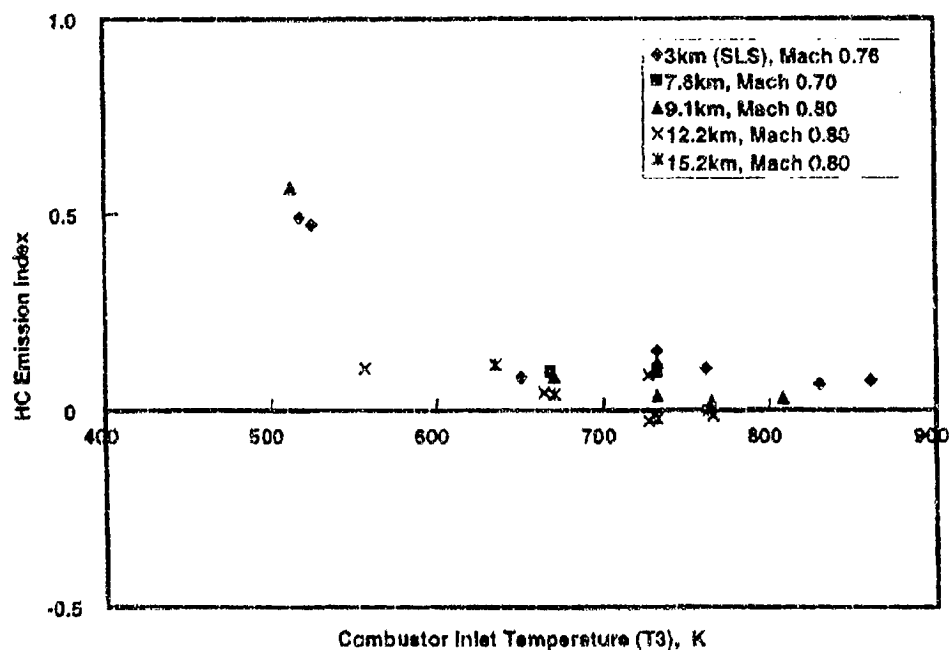
Figure 12. Horizontal bar EI(THC) summary for all test conditions.

29
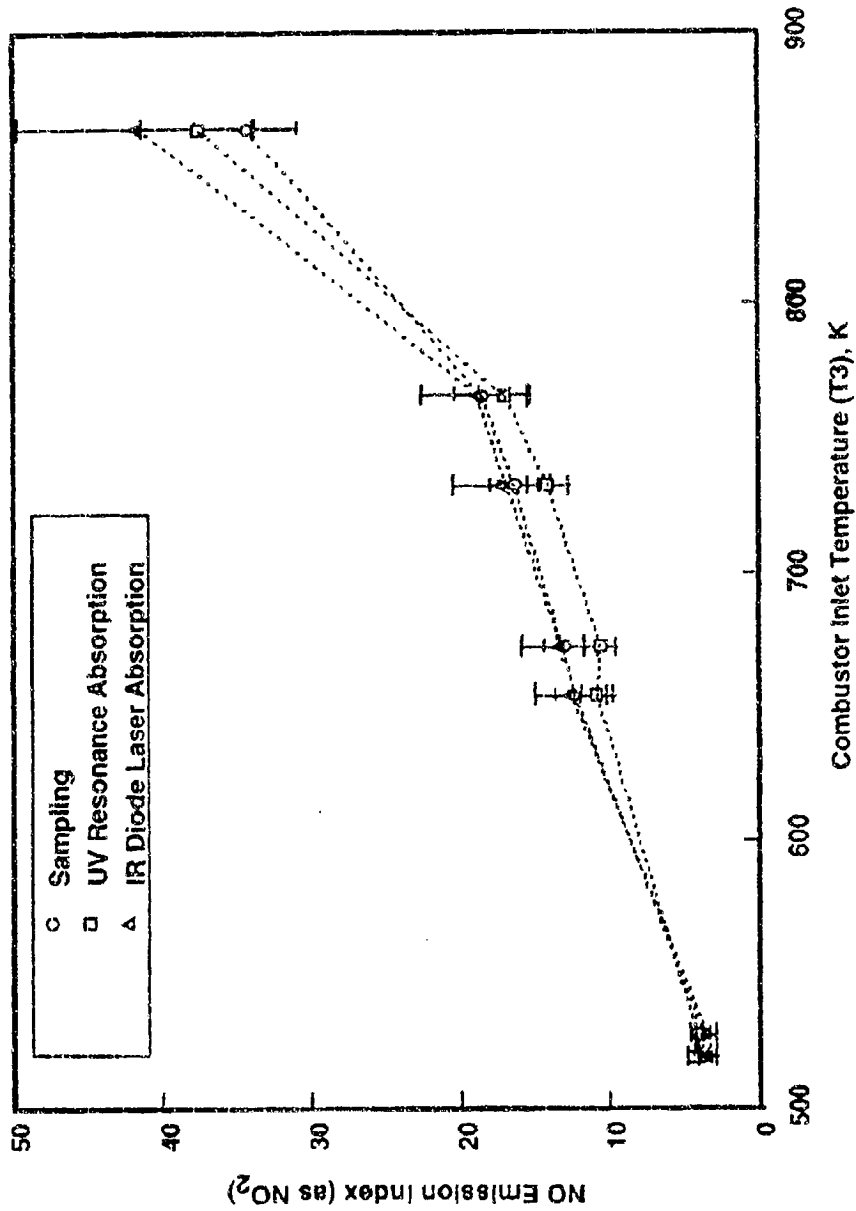
Figure 13. Comparisons of EI(NO) at simulated sea-level-static condition.
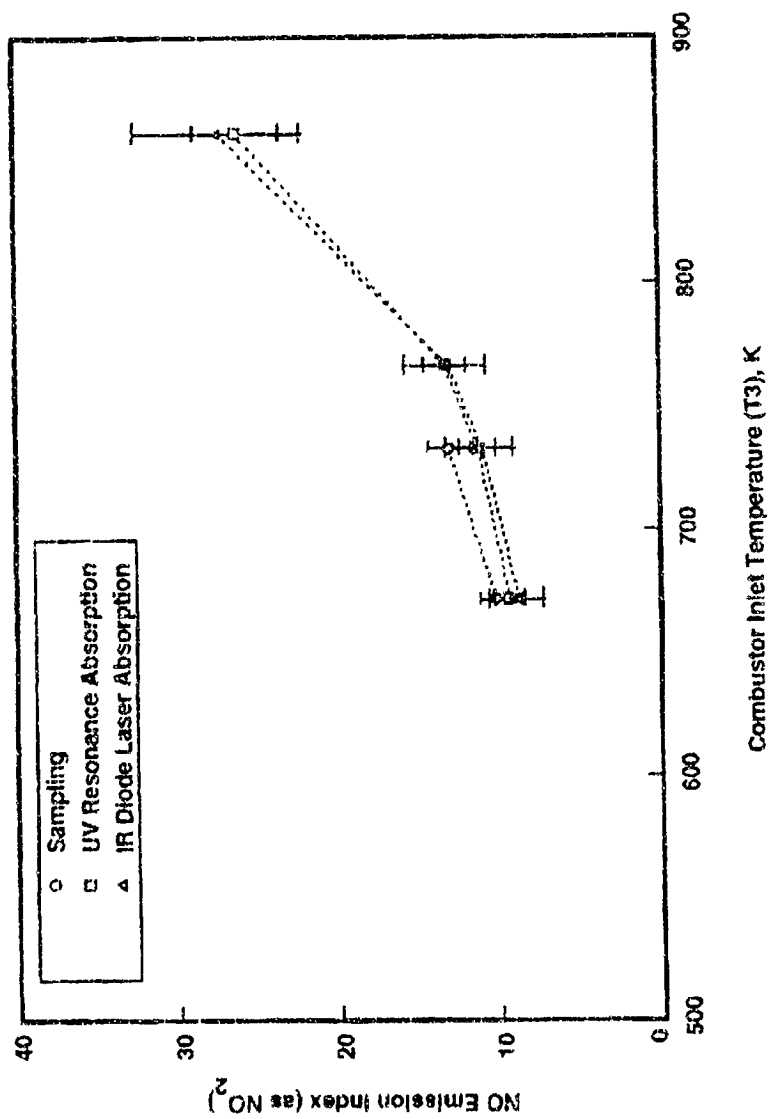
Figure 14. Comparisons of EI(NO) at 7.6-km altitude.

31
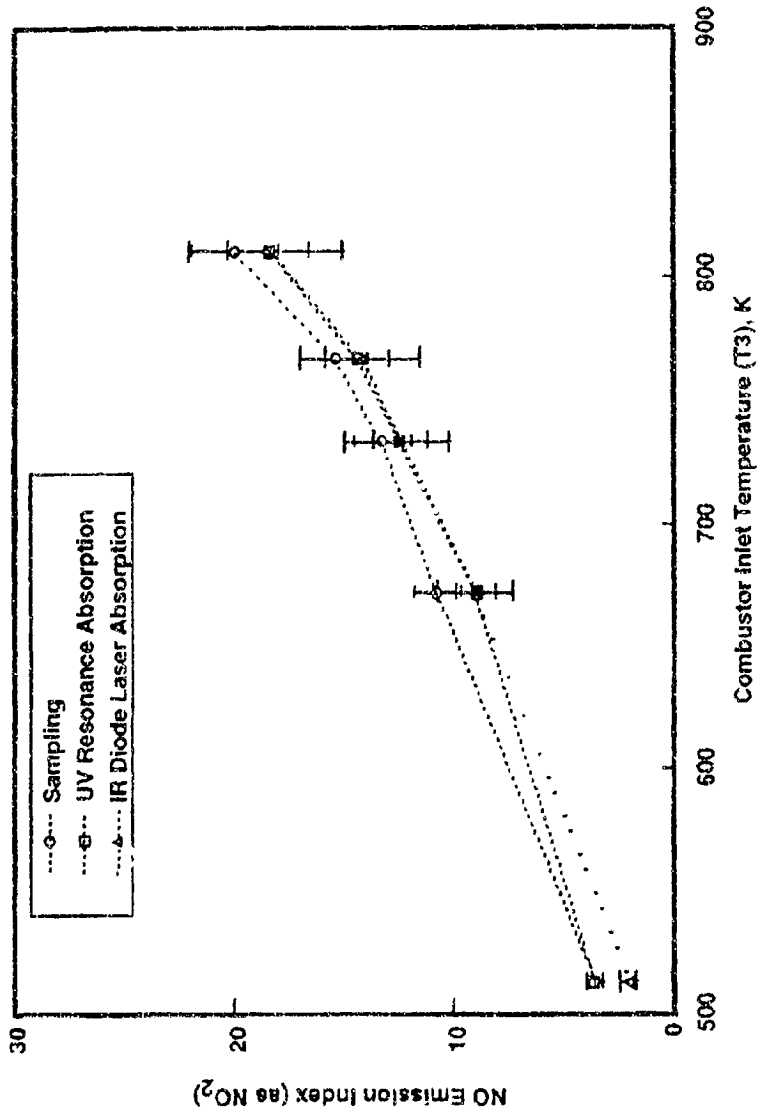
Figure 15. Comparisons of EI(NO) at 9.1-km altitude.

32
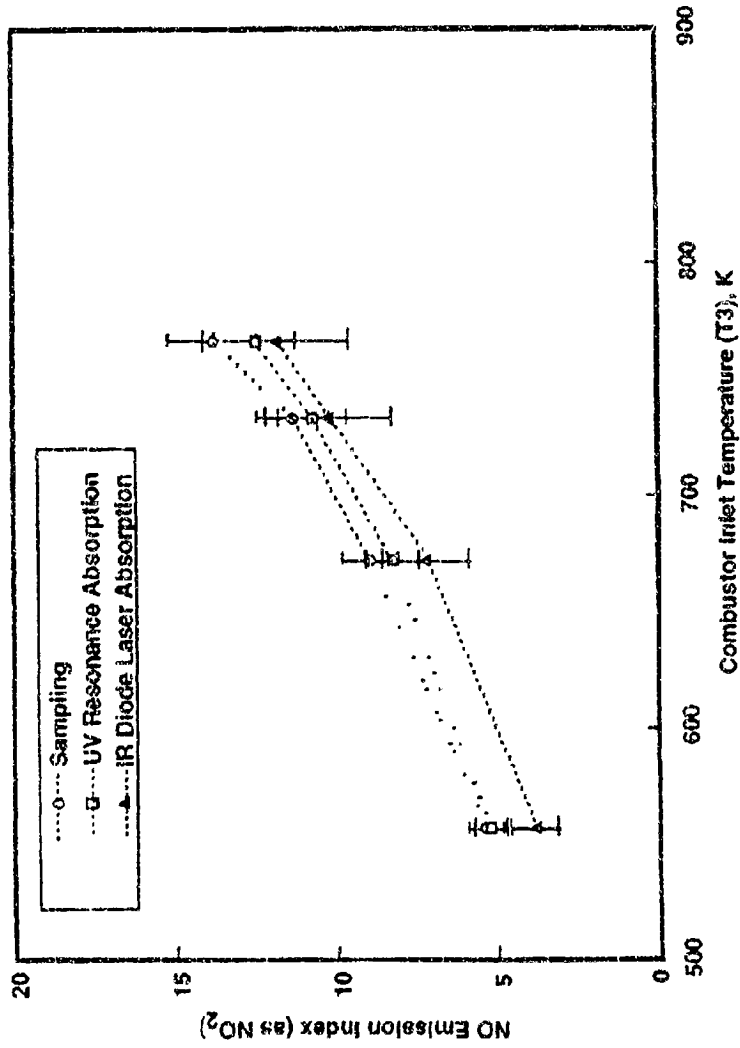
Figure 16. Comparisons of EI(NO) at 12.2-km altitude.

33
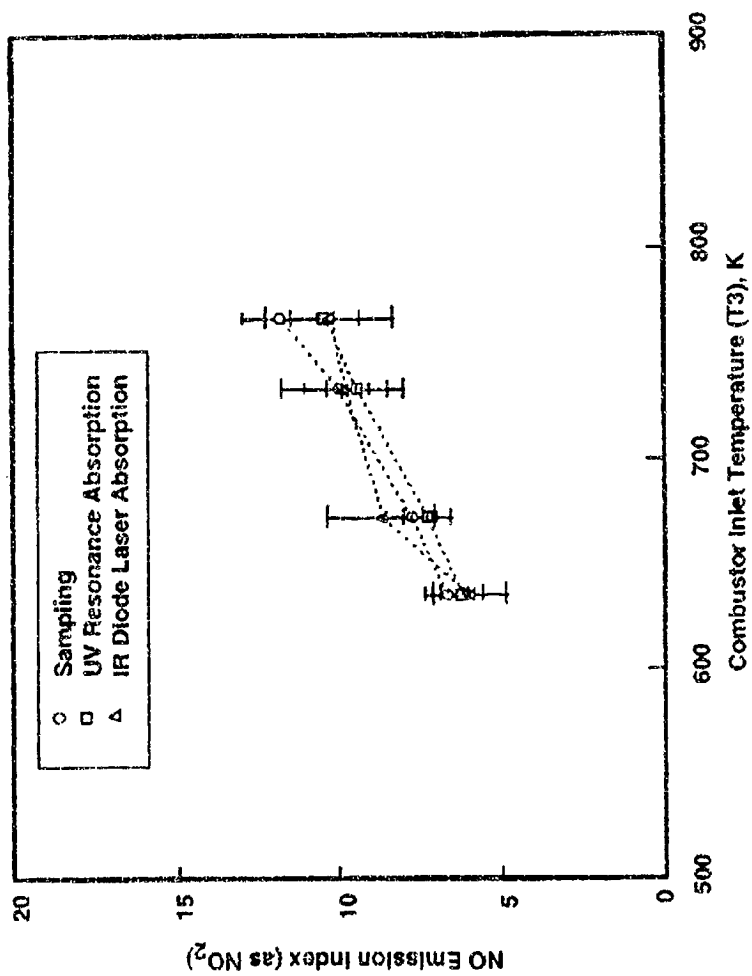
Figure 17. Comparisons of EI(NO) at 15.2-km altitude.
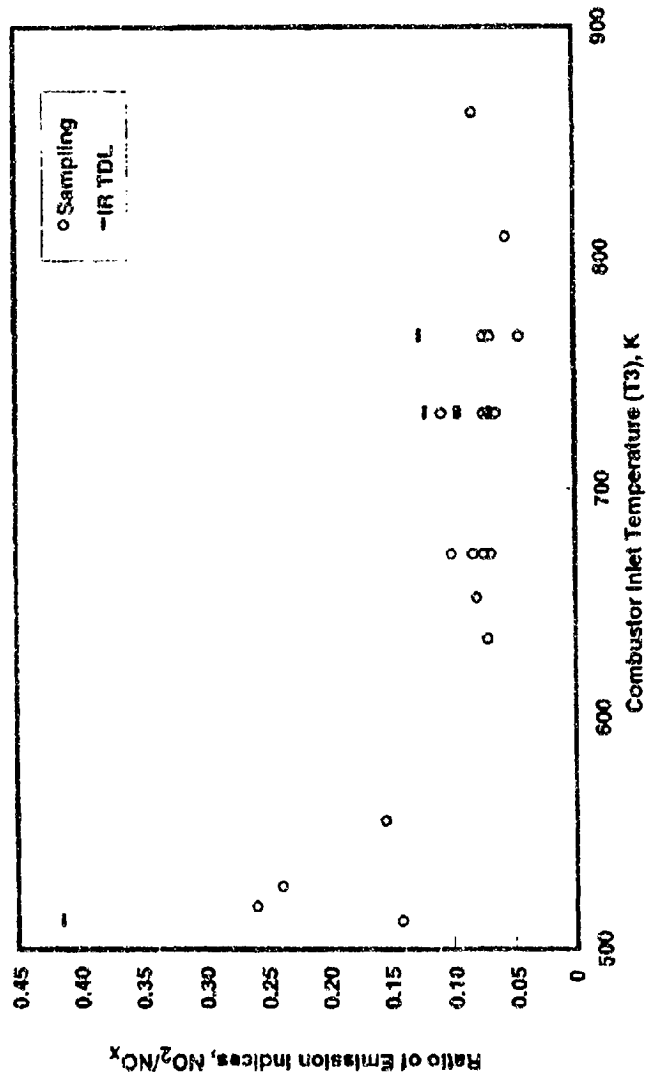
Figure 18. Ratio of emission indices NO_2/NO_x at all test conditions.

Table 1. AEDC Fuel Analysis Report

Laboratory Analysis Method	Laboratory Test	Laboratory Results		
		Pretest	Midtest	Posttest
ASTM[1] D2382	Heat of Combustion, btu/lbm Gross	19814.6	19818.0	19820.8
ASTM D2382	Heat of Combustion, btu/lbm Net Min.	18544.7	18547.2	18550.0
ASTM D3701	Hydrogen Content, percent by Wt.	13.92	13.93	13.93
ASTM D3828	Flash Point, °F	144	143	145
ASTM D4052	Specific Gravity (15C/4C), Min.-Max @ 60°F/4°C @100°F/4°C	08147 0.7985	0.8147 0.7986	0.8148 0.7987
ASTM D445	Viscosity @0°F, cs 70°F, cs 150°F, cs	5.710 2.159 1.114	5.723 2.163 1.115	5.730 2.165 1.117
TO[2] 42B-1-1	Free Water, PPM, max	0	0	0

[1] American Society for Testing and Materials

[2] Air Force Technical Order

Table 2. USAF Aerospace Fuels Laboratory Fuel Analysis Report

Laboratory Analysis Method	Laboratory Test	Laboratory Results
ASTM* D4176	Workmanship	pass
ASTM D3242	Total Acid Number, mg KOH/g	0.004
ASTM D1319	Aromatics, percent vol	14.0
ASTM D1319	Olefins, percent vol	0.9
ASTM D3227	Mercaptan Sulfur, percent wt	0.001
ASTM D4294	Total Sulfur, percent wt	0.06
ASTM D86	Distillation IBP, °C 10 percent 20 percent 50 percent 90 percent EP Residue, percent vol Loss, percent vol	176 197 204 219 249 271 1.3 1.5
ASTM D93	Flash Point, °C	60
ASTM D1298	Gravity, API	41.9
ASTM D2386	Freezing Point, °C	−48
ASTM D445	Viscosity @−20°C, cs	6.2
ASTM D3338	Heat of Combustion, MJ/kg	43.2
ASTM D3343	Hydrogen Content, percent wt	13.8
ASTM D1322	Smoke Point, mm	25.0
ASTM D130	Copper Strip Corrosion	1a

*American Society for Testing and Materials

Table 2. Concluded

Laboratory Analysis Method	Laboratory Test	Laboratory Results
ASTM D3241	Thermal Stability Tube Deposit visual Change in Press., mm of Hg	1 0
ASTM D381	Existent Gum, mg/100ml	0
ASTM D5452	Particulate Matter, mg/l	0.3
SPEC	Filtration Time, min	10
ASTM D1094	Water Reaction	2
ASTM D5006	FSII, percent vol	0.16
ASTM D2624	Conductivity, pS/m	244
ASTM D5001	Ball-On-Cylinder, mm	0.56
	Trace Metal Results Cu Fe Zn	69 ppb <5 ppb 67 ppb

*American Society for Testing and Materials

Table 3. Engine and Flight Conditions

Flight Parameters					Engine Parameters				Time-On Condition		
Simulated Altitude, km	Flight Mach Number	Engine inlet Temperature, K	Engine inlet Pressure, atm	Inlet Air Dew-Point Temperature, K	Combustor Inlet Total Temperature, K	Combustor Inlet Total Pressure, atm	Fuel/Air Core	Fuel/Air Mixed	Steady-State Data Point Numbers	Start	Stop
SLS* (3.13)	0.76	288	0.999	255	733	18.771	0.0166	0.0101	86-94	14:53	16:21
SLS* (3.13)	0.76	288	0.998	255	569	13.330	0.0138	0.0078	96,98	16:24	16:34
SLS* (3.12)	0.76	288	0.999	255	658	12.041	0.0130	0.0072	100,101	16:37	16:42
SLS* (3.12)	0.76	288	0.999	255	526	5.158	0.0086	0.0037	103,104	16:45	16:52
SLS* (3.12)	0.76	288	1.000	255	517	4.766	0.0086	0.0036	105-106	16:54	17:01
SLS* (3.12)	0.76	288	0.998	255	762	21.473	0.0177	0.0111	108-109	17:06	17:15
SLS* (3.12)	0.76	288	0.997	255	861	30.458	0.0216	0.0145	111-113	17:17	17:40
7.62	0.70	285	0.513	242	858	15.983	0.0219	0.0149	26	8:09	8:18
7.62	0.70	285	0.513	242	764	11.584	0.0181	0.0115	28	8:22	8:24
7.62	0.70	285	0.514	242	733	9.938	0.0169	0.0104	30	8:26	8:41
7.62	0.70	285	0.514	242	668	7.084	0.0142	0.0081	32	8:43	8:50
9.12	0.79	260	0.451	242.6	512	3.240	0.0089	0.0043	35	9:06	9:13
9.15	0.80	259	0.451	242.5	733	11.872	0.0178	0.0116	37,38,40-49	9:16	11:13
9.14	0.80	259	0.451	242.6	765	13.334	0.0190	0.0126	51-52	11:16	11:24

* Simulated sea-level-static engine inlet conditions, but cell ambient pressure was equivalent to about 3.1-km altitude.

Table 3. Concluded

Flight Parameters					Engine Parameters				Time-On Condition		
Simulated Altitude, km	Flight Mach Number	Engine Inlet Temperature, K	Engine Inlet Pressure, atm	Inlet Air Dew-Point Temperature, K	Combustor Inlet Total Temperature, K	Combustor Inlet Total Pressure, atm	Fuel/Air Core	Fuel/Air Mixed	Steady-State Data Point Numbers	Start	Stop
9.13	0.79	259	0.451	242.6	808	14.576	0.0207	0.0142	54-55	11:26	11:39
9.13	0.80	259	0.452	242.6	671	8.779	0.0153	0.0084	57-58	11:43	11:55
12.19	0.79	245	0.280	237	727	8.300	0.0182	0.0121	60-64	12:05	12:48
12.18	0.79	245	0.281	237	766	9.099	0.0197	0.0135	66-68	12:50	13:13
12.17	0.80	245	0.282	237	665	6.331	0.0158	0.0100	71-72	13:17	13:26
12.18	0.80	245	0.282	237	557	3.317	0.0116	0.0084	74-75	13:29	13:37
15.27	0.80	245	0.174	242	635	3.275	0.0156	0.0095	76-77	13:46	13:56
15.22	0.79	245	0.174	242	671	4.011	0.0169	0.0108	79	14:00	14:05
15.30	0.80	245	0.173	242	732	5.236	0.0191	0.0129	81	14:09	14:15
15.27	0.80	245	0.173	242	764	5.645	0.0204	0.0141	82-84	14:18	14:35

* Simulated sea-level-static engine inlet conditions, but cell ambient pressure was equivalent to about 3.1-km altitude.

Table 4. Measurement Systems Used to Characterize Exhaust Emissions

Measurement System	Measurement Quantity	Principal Agency
Optical Non-Intrusive		
IR Tunable-Diode Laser Absorption	NO, NO_2, CO_2, H_2O	Aerodyne Research. Inc.
NO-UV Resonance Absorption	NO	Sverdrup/AEDC
NO-UV Continuum Absorption	NO	
UV-Laser Absorption	OH	
Extractive Sampling		
ARP1256*	CO, CO_2, O_2, NO, NO_x, THC	Sverdrup/AEDC
Smoke Number Meter*	Plume Visibility (Soot)	
Hygrometer	Inlet Air Humidity	
Mobile Aerosol Sampling System (MASS)	Particulate/Aerosol: Total Mass, Size Distribution, Hydration Properties, Emission Indices	University of Missouri-Rolla
Extractive IR-Absorption	CO_2	
		McDonnell Douglas
Probes	Exhaust Sample Extraction	
Sample Probe		Sverdrup/AEDC
	Local Mach Number, Flow Angularity,	
Cone Static, Pitot Pressure, and Total Temperature Probes	Static Temperature, and Static Pressure	Sverdrup/AEDC

* Aerospace Recommended Practice (ARP) 1256B "Procedure for the Continuous Sampling and Measurement of Gaseous Emissions from Gas Turbine Engines"

Table 5. Summary of Exhaust Emissions Characterization

PERFORMANCE PARAMETERS						GAS SAMPLING DATA [2]							UV	IR	MASS [3]	SMOKE [4]
Simulated Altitude, km	Flight Mach Number	T3, K	P3, atm	Fuel/Air Core	Fuel/Air Mixed	(CO2) percent	EI(CO)	EI(THC)	EI(NOx) as NO2	Carbon Balance Fuel/Air	Comb. Eff. percent	EI(NO) as NO2	EI(NO) as NO2	EI(NO) as NO2	EI(CN) (Number)	Smoke Number
SLS [1] (3.1)	0.75	517	4.8	0.0086	0.0086	1.40	14.19	0.49	5.18	0.0069	99.61	3.84	4.73	3.43	7.70E-13	
SLS [1] (3.1)	0.76	526	5.2	0.0086	0.0037	1.45	13.27	0.47	5.44	0.0071	99.64	4.16	4.16	3.59	3.14E+12	
SLS [1] (3.1)	0.76	651	12.0	0.0130	0.0072	2.39	1.11	0.08	13.36	0.0115	99.97	12.30	10.77	12.59	1.89E+13	
SLS [1] (3.1)	0.76	669	15.3	0.0138	0.0078	2.50	0.80	0.09	14.05	0.0121	99.97	13.02	10.53	13.31	2.99E+13	
SLS [1] (3.1)	0.76	733	18.7	0.0166	0.0101	3.05	0.25	0.15	17.45	0.0146	99.98	16.44	14.08	17.19	1.35E+13	0.7
SLS [1] (3.1)	0.76	762	21.5	0.0177	0.0111	3.27	0.35	0.10	19.78	0.0157	99.98	18.44	16.96	18.94	1.89E+13	
SLS [1] (3.1)	0.76	831	28.4	0.0195	0.0114	4.00	0.35	0.07	29.93	0.0191	99.99	27.47	37.54			
SLS [1] (3.1)	0.76	861	30.5	0.0216	0.0145	1.21	0.37	0.07	37.14	0.0200	99.98	34.36	37.54	41.78	1.37E+13	1.3
7.62	0.70	668	7.1	0.0142	0.0081	2.15	1.72	0.10	11.22	0.0128	99.95	10.26	9.33	8.91	9.43E+11	
7.62	0.70	733	9.9	0.0169	0.0104	3.10	0.88	0.09	13.90	0.0149	99.97	13.09	11.20	11.15	4.04E+12	
7.62	0.70	764	11.6	0.0181	0.0115	3.14				0.0160			13.20	13.28		
7.62	0.70	858	16.0	0.0219	0.0149	4.31				0.0205			26.18	27.18		

(1) Simulated sea-level-static engine inlet conditions, but test cell ambient pressure was equivalent to about 3.1-km altitude.
(2) Gas sampling summary data are horizontal bar averages.
(3) MASS (Mobile Aerosol Sampling System) summary data are primarily vertical rake data
(4) Only three smoke data points are available

Table 5. Concluded

Simulated Altitude, km	Flight Mach Number	TT, K	PT, atm	Fuel/Air Gas	Fuel/Air Mixed	(CO₂) percent	EI(CO)	EI(THC)	EI(NOx) as NO₂	Carbon Balance Fuel/Air	Comb Eff percent	EI(NO) as NO₂	UV EI(NO₂) as NO₂	IR EI(NO) as NO₂	MASS EI(CN) (Number)	SMOKE Smoke Number
9.12	0.79	512	3.2	0.0089	0.0083	1.63	19.89	0.57	4.38	0.0080	99.48	3.52	7.60	2.06	4.82E+13	
9.13	0.80	671	8.8	0.0153	0.0094	2.74	1.10	0.08	11.77	0.0112	99.97	10.74	8.90	9.02	5.70E+12	
9.15	0.80	733	11.9	0.0178	0.0116	3.42	0.79	0.08	14.34	0.0164	99.97	13.26	12.40	12.55	8.96E+12	
9.14	0.88	755	13.3	0.0190	0.0126	3.69	0.69	0.02	16.58	0.0176	99.98	15.41	14.40	14.26	7.83E+12	
9.13	0.79	808	14.6	0.0207	0.0142	4.07	0.66	0.03	21.16	0.0194	99.98	20.01	18.40	18.53	6.45E+12	-11
12.18	0.80	557	3.3	0.0116	0.0084	2.11	9.33	0.11	6.38	0.0103	98.77	5.39	5.20	3.85	3.37E+12	
12.17	0.80	665	6.3	0.0158	0.0100	2.93	1.96	0.04	9.94	0.0141	99.95	8.96	8.20	7.20	1.03E+13	
12.19	0.79	727	8.3	0.0182	0.0121	3.49	1.12	0.09	12.44	0.0167	99.95	11.43	10.20	10.20	1.03E+13	
12.18	0.79	766	9.1	0.0197	0.0135	3.78	1.47	0.01	14.90	0.0180	99.97	13.84	12.50	11.55	1.23E+13	
15.27	0.80	635	3.3	0.0156	0.0095	2.87	5.22	0.12	7.21	0.0138	99.87	6.69	6.20	6.01		
15.22	0.79	571	4.0	0.0169	0.0108	3.13	1.99	0.04	8.34	0.0150	99.90	7.78	7.30	8.73	1.52E+12	
15.30	0.80	712	5.2	0.0191	0.0129	3.66	3.31	0.02	10.74	0.0176	99.93	10.03	9.40	9.58		
15.27	0.80	754	5.6	0.0204	0.0141	3.92	3.53	0.00	12.33	0.0187	99.92	11.79	10.40	10.29	3.79E+13	

(1) Standard sea-level static engine inlet conditions, heat-less cell ambient pressure was equivalent to about 11-km altitude

(2) Gas sampling summary data are horizontal bar averages.

(3) MASS (Mobile Aerosol Sampling System) summary data are primarily vertical rake data.

(4) Only three smoke data points are available.

43

APPENDIX A
PROBE RAKE SYSTEM

R. S. Hiers, Jr.

A cruciform configuration rake was located just downstream of the engine nozzle exit plane in the test cell diffuser/heat shield to provide extractive emission and jet plume aerodynamic data. A photograph illustrating the rake installed behind the engine is shown in Fig. A-1.

A-1.0 SAMPLE EXTRACTION PROBES

The primary function of the rake was to provide a well-resolved, spatial distribution of extractive gas samples to a suite of SAE qualified/standard emission instrumentation for characterizing engine emissions. For this purpose, the extractive gas sample probes were located on nominal 5.08-cm centers on both the vertical and horizontal members of the cruciform rake, 12.7 cm downstream of the nozzle exit plane. For completeness, extractive probes were positioned in the hot core flow, the bypass flow, and also in the test cell cooling flow external to the engine flow path.

A sketch of a gas sample extraction probe is shown in Fig. A-2, illustrating the probe's sharp-edged inlet orifice and nominal 10 to 1 area expansion just downstream of the inlet. These features eliminate mutual mass flow interference between interconnected (ganged) probes when suitable sample system back pressures are maintained on the extractive probes.

The sample transport lines from each extractive probe were routed individually to a valving system which permitted both individual gas samples or collective (ganged) gas samples from desired groupings of individual extractive probes to be obtained.

The sample transport lines were heated with steam tracing and insulated to maintain a temperature of approximately 422 K, from the location where the sample transport line emerged from the engine exhaust heated portion of the rake structure to the valving system, to prevent condensation. Of course, on the rake structure influenced by the hot engine flow, extractive sample lines are typically well above 422 K.

The valving system and the sample transfer lines connected directly to the emission analyzers were also maintained about 422 K with electrical heat tracing and insulation.

A-2.0 AERODYNAMIC PROBES

Mach/flow angularity and stagnation temperature probes were also employed on the rake for providing local pointwise static pressure, static temperature, density, and velocity along the line-of-sight (LOS) of both the UV and the IR optical instrumentation. The optical instrumentation provided "non-intrusive" measurements for comparison and validation with extractive probe data (NO concentration primarily).

In the past, computational model results were used to provide the local thermodynamic conditions in the LOS of optical instrumentation. Local gas properties are used for molecular pressure broadening corrections and energy level populations, and for computing relative density (e.g., ppm) from the absolute densities directly.

In the present work, the thermodynamic parameters were measured to eliminate the uncertainty inherent in using model results and consequently to provide better assessment of the fundamental accuracy of these optical techniques. A secondary by-product of these data is the ability to validate/assess the engine plume models by comparison with rake data.

Seven conventional Mach/flow angularity (MFA) probes and 10 stagnation temperature probes were mounted on the horizontal member of the rake, interspersed between the gas extraction probes. Design details of the MFA and stagnation temperature probe are shown in Figs. A-3 and A-4. The MFA probes and the total temperature probes were all located on 10.16-cm centers. The physical relationship and spacing (2.54-cm probe-to-probe) between the extraction, MFA and total temperature probes is illustrated in Fig. A-5.

A-3.0 DATA REDUCTION

The basic data reduction procedure for inferring the free-stream velocity and static thermodynamic flow properties from the combination of MFA, stagnation temperature, and extraction measurements is illustrated schematically in Fig. A-6.

Briefly a computational fluid dynamic (CFD) relationship was developed relating the ratio of average cone surface pressure to cone pitot pressure of the MFA probe to the free-stream Mach number. The relationship is strongly dependent on MFA probe configuration and as evident from Fig. A-5, MFA probe geometry was carefully controlled during manufacture and testing. The relationship of the cone surface to cone pitot pressure ratio to Mach number is much less sensitive to composition. Nevertheless, the composition determined from the extractive probes was used to precisely describe the gas internal energy characteristics for the correlation of MFA probe pressure data with Mach number.

46

Once the local Mach number just upstream of an MFA probe location was inferred from MFA probes as described, the local static pressure was inferred from the gas dynamic relationship between the measured cone pitot pressure and the now known Mach number.

Static gas temperature upstream of MFA probes was similarly inferred from the gas dynamic relationship between the now known Mach number and the measured total temperature (again accounting for the minor effect of gas composition).

Unfortunately, since the Mach number and stagnation temperature were not measured coincidentally in space, the total temperature that would actually exist at an MFA probe required estimation by interpolating from measured total temperatures on either side of the desired probe location.

Once temperature and pressure (along with composition) were determined, all the remaining thermodynamic properties, e.g., density, were unambiguously computed. Local stream velocity was also determined from Mach number and static temperature, completing the definition of the local state of the flow field at a discrete point in the LOS of the optical instrumentation.

A-4.0 RAKE DATA UNCERTAINTY

Typical uncertainties in the measured probe temperatures and pressures are of the order of 0.75 percent and 0.25 percent, respectively. The maximum uncertainty in any of the derived thermodynamic parameters is about 2 percent as a result of propagation of measurement uncertainties through the data reduction algorithms. The uncertainties are primarily bias errors. The use of a CFD-generated "calibration" for the Mach number probes, as previously described, introduces an additional source of uncertainty compared with the use of an actual aerodynamic calibration for the MFA probes. However, this technique has been previously used and validated at AEDC for similar conditions where "CFD calibrations" were compared with actual aerodynamic MFA probe calibrations. For larger MFA probes, typified by the present design where the external aerodynamic geometry can be precisely controlled during manufacture and test, CFD calibrations have been found to be essentially equivalent to aerodynamic calibrations for the spherically blunted class of conical MFA probes. Also in previous work, it was found that for other MFA probe geometries or much smaller probes, aerodynamic calibrations were required because smaller probes' geometries cannot be repeatably manufactured.

Since the large-scale class of MFA probes was used for these tests, the uncertainty introduced by the use of CFD calibrations is believed small and is conservatively estimated to result in a total uncertainty in any of the rake aerodynamic properties of no more than 5 percent, based on the historical experience described above.

A validation of the quality of the rake data is illustrated by comparing the mass flow integrated from rake-derived velocity and densities with the independent measurements of total air and fuel flow provided by the test facility instrumentation.

In spite of the interpolation required of the relatively sparse probe data and the extrapolation required in the region of high gradient near the edge of the engine nozzle, the integrated mass flow is clustered within ±15 percent of the total mass flow to the engine over the range of power and altitudes tested.

Because of the large extraneous uncertainties introduced into these comparisons by the interpolations and extrapolations required for the integration, the above comparisons suggest that the estimated uncertainty in individual rake properties of less than 5 percent is realistic.

Of course, if this becomes an issue in analysis of LOS optical data, the MFA probe may yet be calibrated aerodynamically and the uncertainty more accurately determined. The best use of an aerodynamic calibration would be to re-reduce the aerodynamic data with a concurrent lowering of the residual uncertainty. This remains an open, attractive option.

A-5.0 RAKE AERODYNAMIC DATA

Rake aerodynamic data for all test conditions are summarized in Table A-1. The location of the probes in the engine exhaust plume is relative to the nozzle exhaust coordinate system, shown in Fig. A-7.
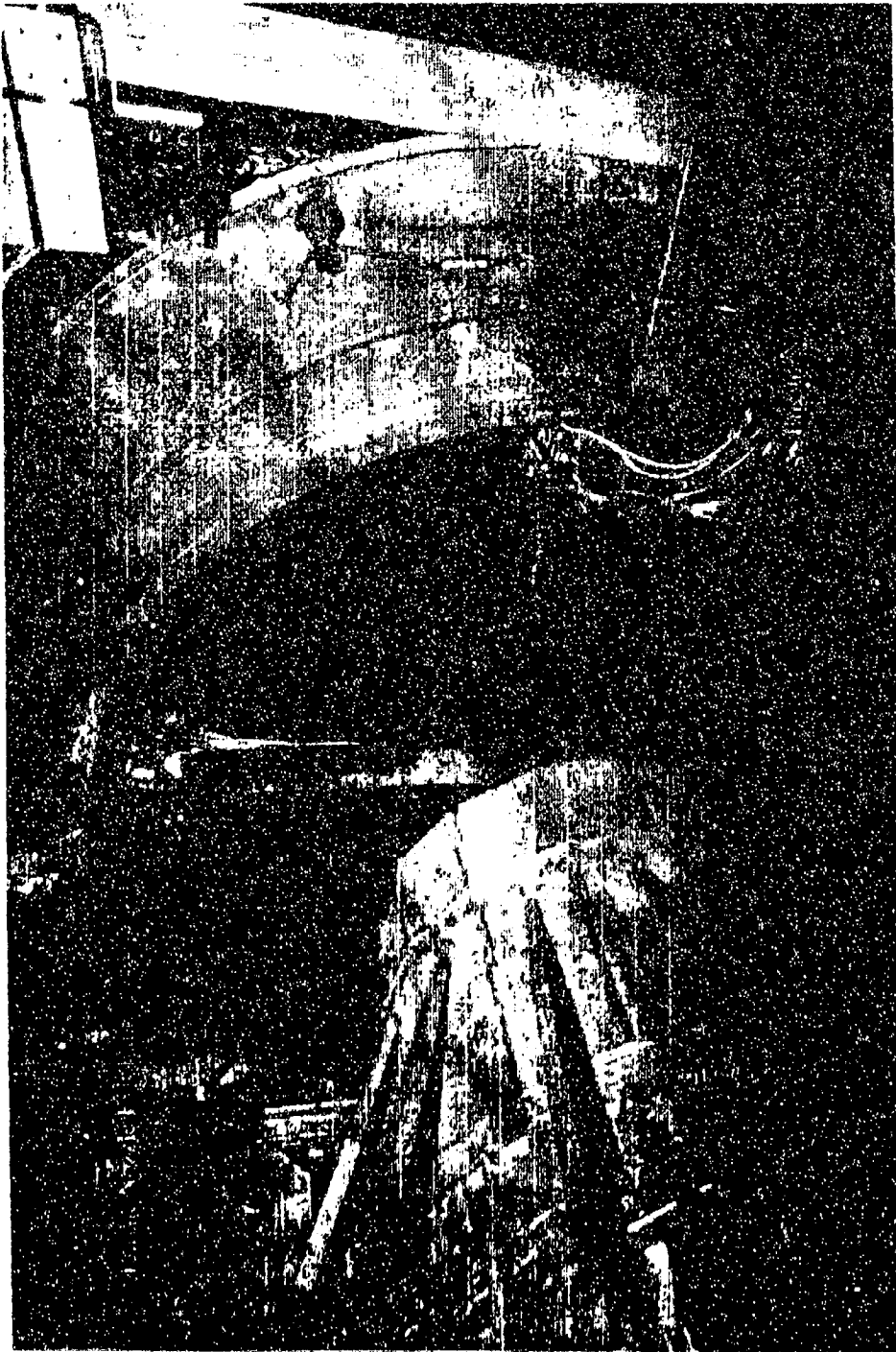
Figure A-1. Rake installation in engine exhaust.
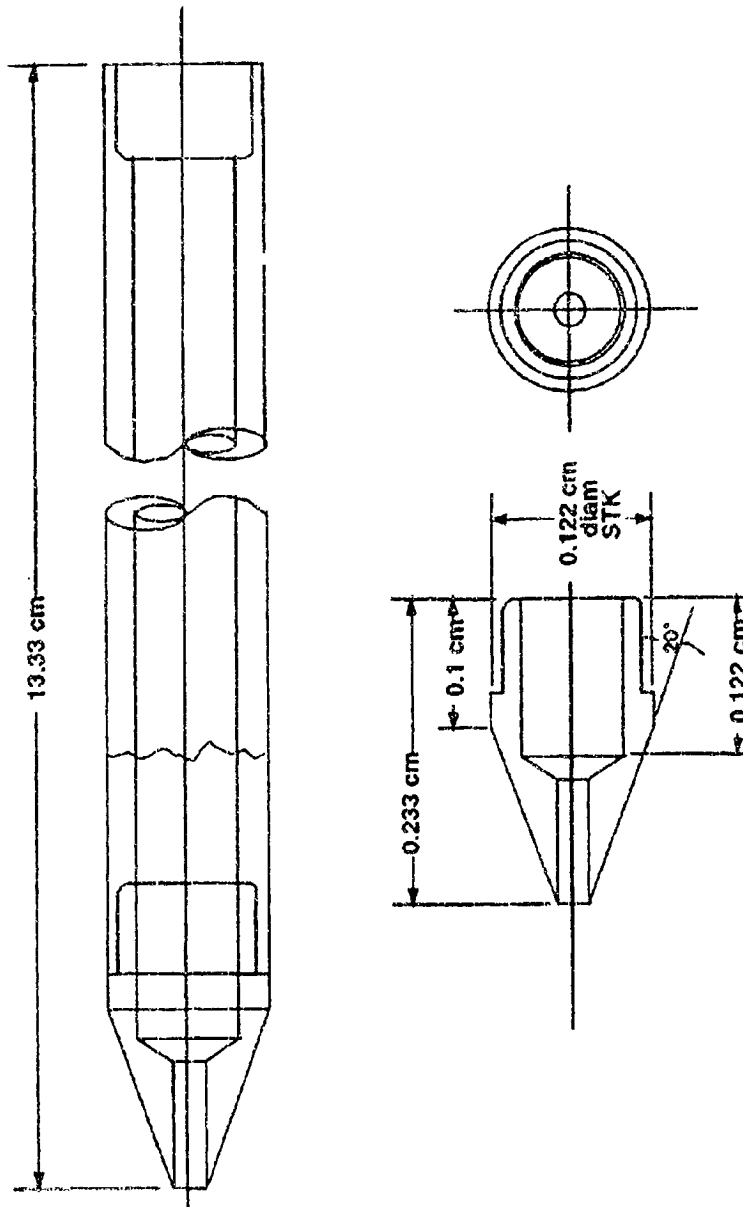
Figure A-2. Extractive sampling probe.

50
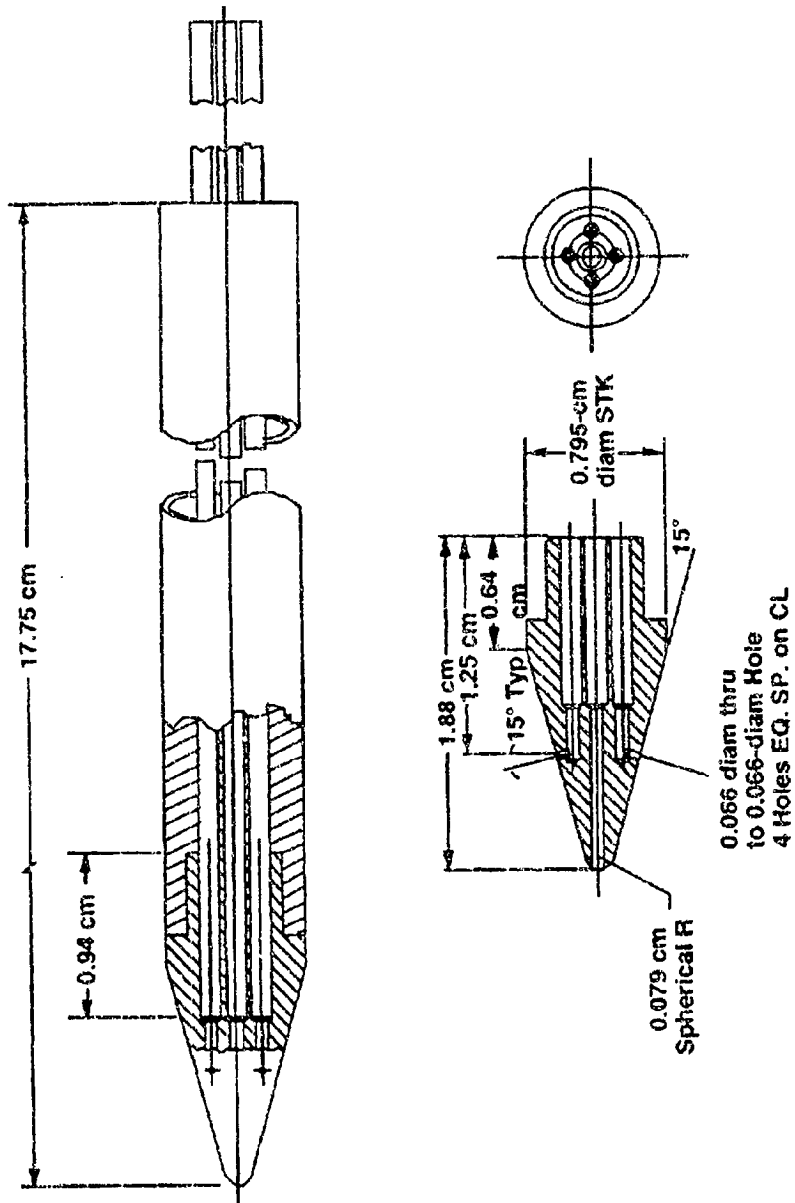
Figure A-3. Mach/flow angularity (MFA) probe.

51
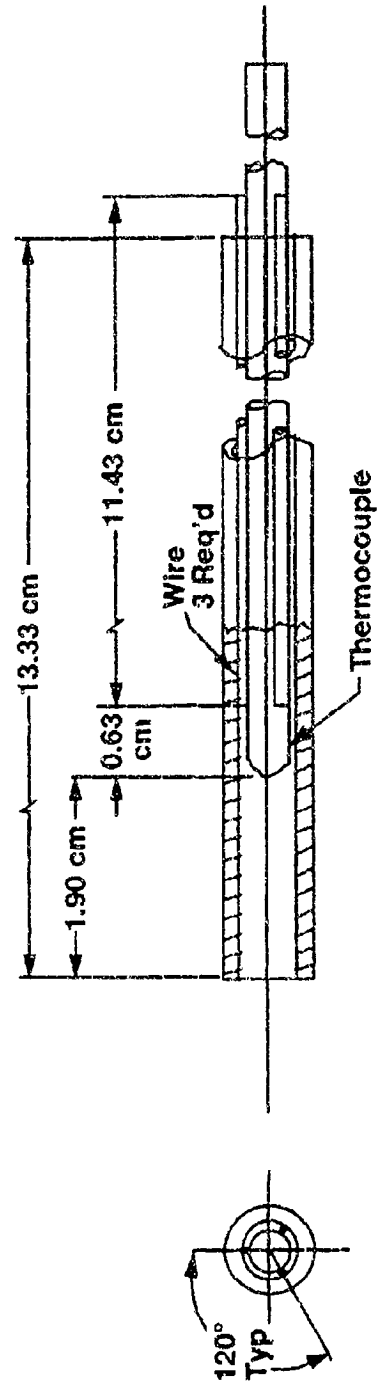
Figure A-4. Stagnation temperature probe.

13.33 cm

11.43 cm

0.63 cm

1.90 cm

Wire
3 Req'd

Thermocouple

120°
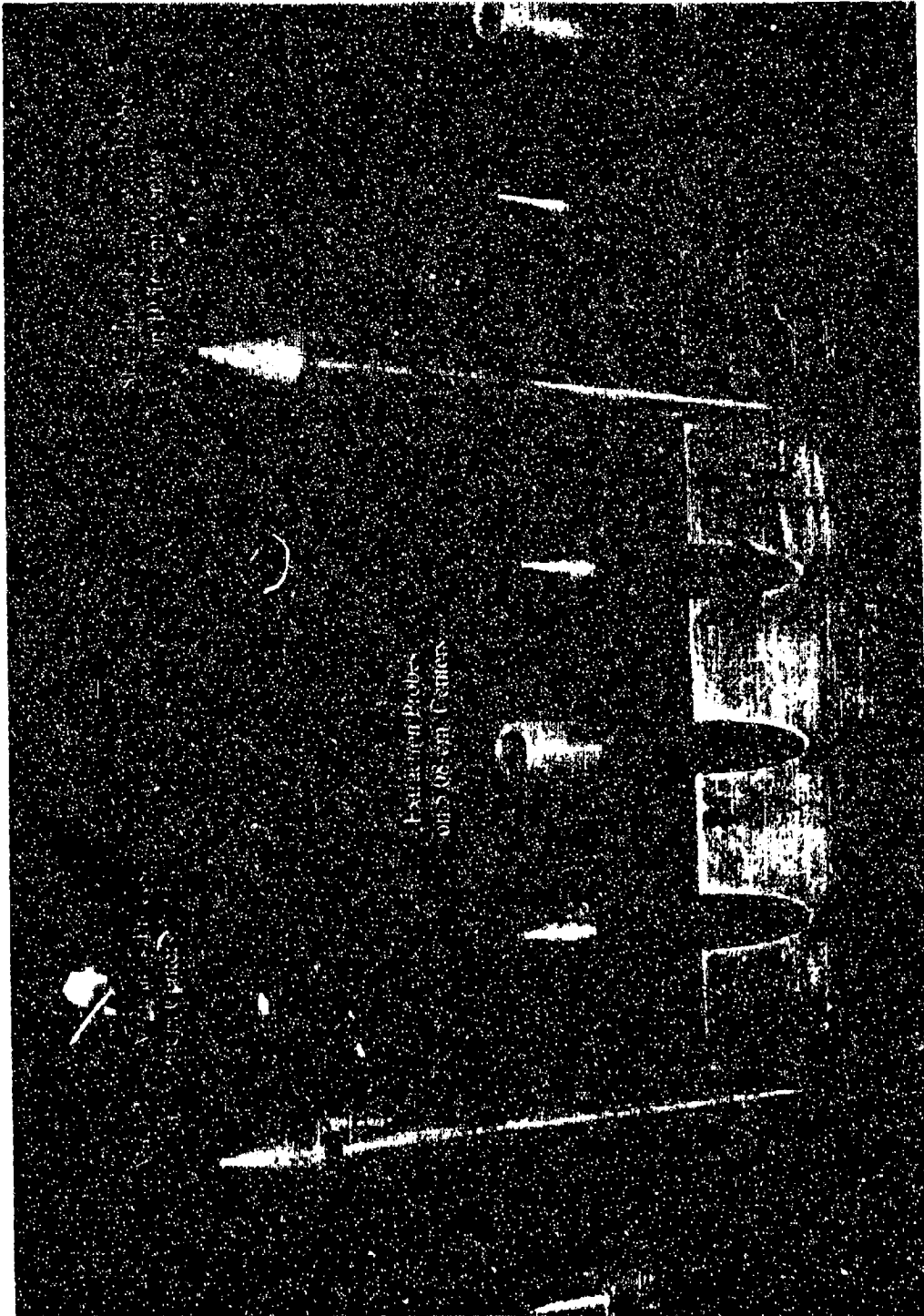Typ
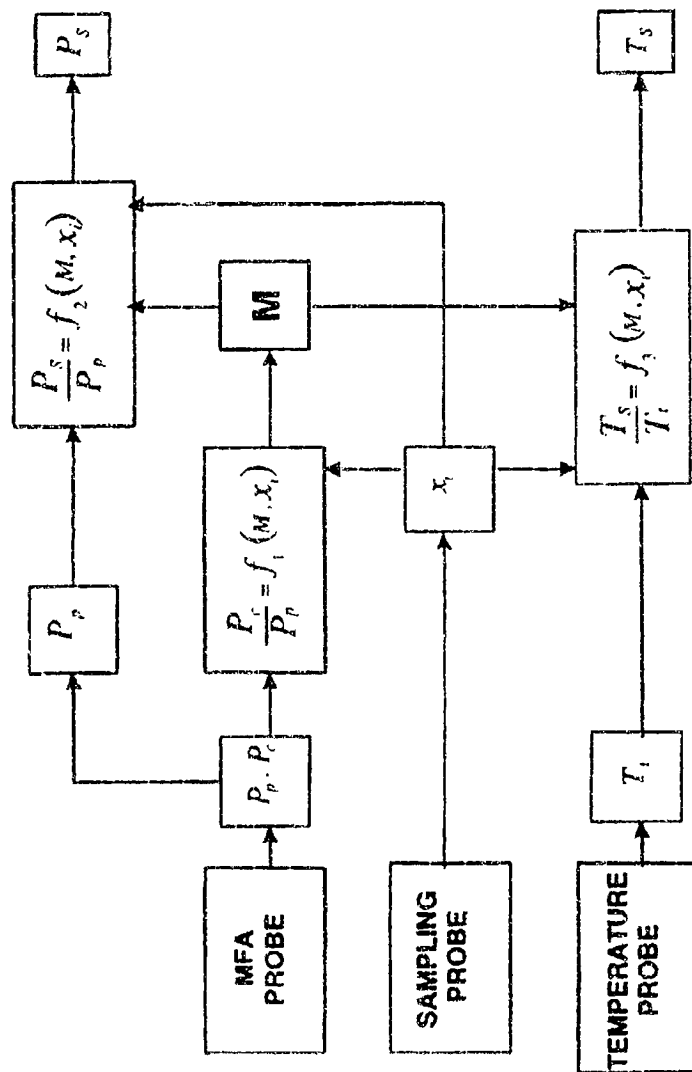
Figure A-5. Typical probe installation on horizontal rake.

Figure A-6. Flow diagram of probe data reduction.
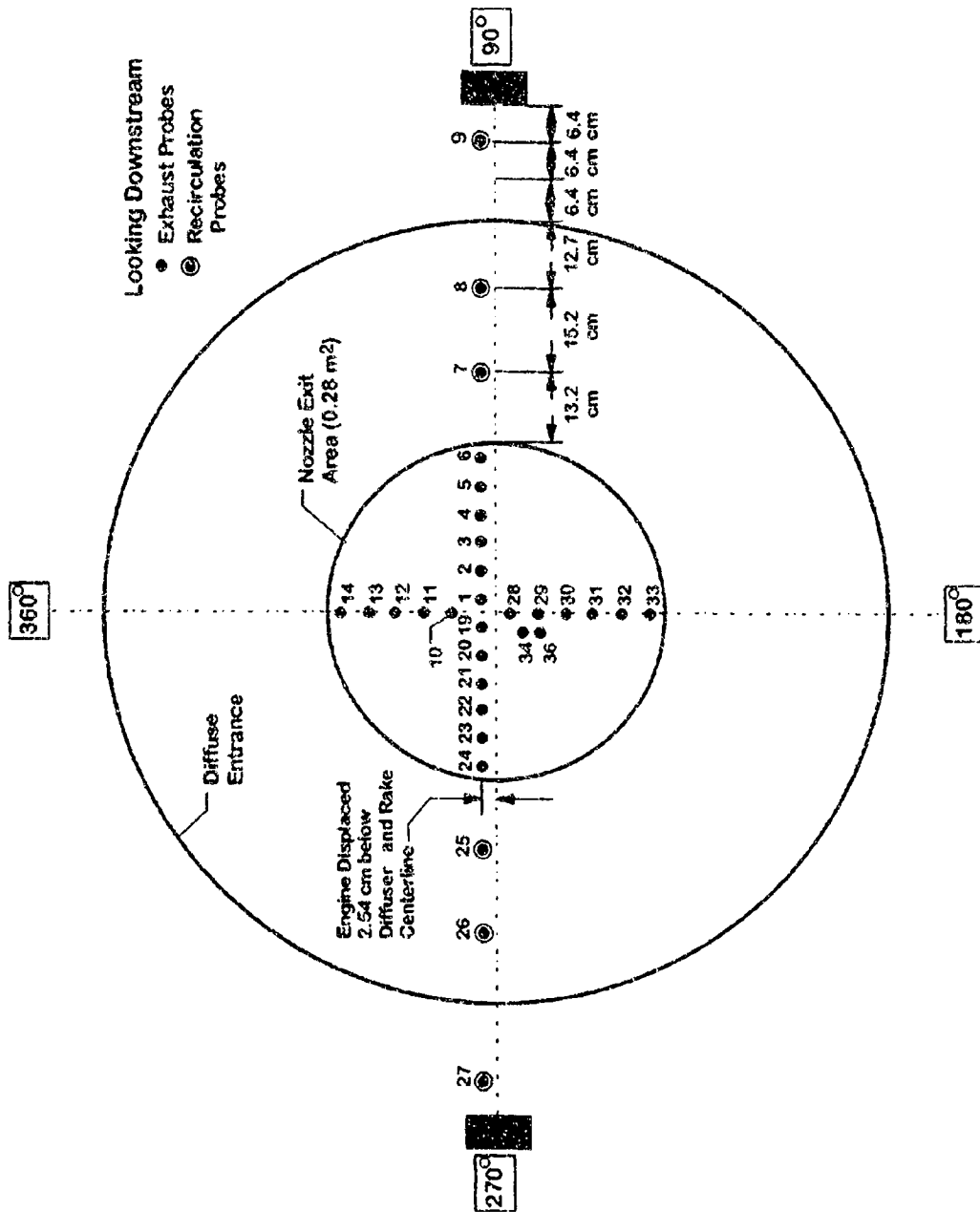
Figure A-7. Gas sampling probe locations near the nozzle exit.

Table A-1. Rake Data

TABLE A-1. Rake and Facility Data	22	23	25	26	29	30	32	33	34	35	Average 37,38, 40-43	Average 51-32	Average 54-55	Average 57-58	Average 59-64	Average 65-68
SSOP (Data Point Number)																
PRG TIME (HR-MIN-SEC) (Run)																
ALT (Altitude) (Run)																
ZMO (Mach Number)																
P7 (atm)																
T7 (K)																
P50 (atm)																
PIH (Combustor Inlet P) (atm)																
TIH (Combustor Inlet Temp) (K)																
FARSH (Core Fuel/Air)																
FARSMX (Mixed Fuel/Air)																
Test Cell Ambient Temp. (K)																
PROBE 1 TOTAL TEMP (K)																
PROBE 2 TOTAL TEMP (K)																
PROBE 3 TOTAL TEMP (K)																
PROBE 4 TOTAL TEMP (K)																
PROBE 5 TOTAL TEMP (K)																
PROBE 6 TOTAL TEMP (K)																
PROBE 7 TOTAL TEMP (K)																
PROBE 8 TOTAL TEMP (K)																
PROBE 9 TOTAL TEMP (K)																
PROBE 10 TOTAL TEMP (K)																
GAMMA																
MACH NUMBER																
PITOT PRESS, atm																
STATIC PRESS, atm																

56

Table A-1. Continued

TABLE A-1. Probe and Facility Data	22	23	26	26	28	29	30	32	33	34	35	Average 37.38 49.49	Average 51.52	Average 54.55	Average 57.58	Average 60.64	Average 66.68
SURF (Data Point Number)																	
-10.16 cm, 2.54 cm	0.55131	0.37425	0.47367	0.46775	0.35629	0.34297	0.35299	0.32968	0.25042	0.29437	0.35271	0.38470	0.42046	0.20243	0.24397	0.26470	
-20.32 cm, 2.54 cm	0.51116	0.08105	0.42495	0.42209	0.35799	0.40166	0.35336	0.30952	0.27464	0.27759	0.33318	0.36170	0.36065	0.31186	0.22680	0.29918	
-40.16 cm, 2.54 cm	0.55279	C.0863	0.5511	0.5241	0.37514	0.35323	0.35820	0.32104	0.29654	0.28722	0.27232	0.20021	0.28505	0.29907	0.18515	0.18175	
STATIC TEMP K																	
-30.48 cm, 2.54 cm	344.5	355.0	459.5	429.0	446.8	441.3	396.8	374.4	325.6	322.4	370.7	377.2	391.7	402.0	363.5	373.7	
-20.32 cm, 2.54 cm	413.1	410.0	557.9	551.9	587.4	567.6	489.1	523.1	382.9	382.4	535.5	568.1	611.3	493.2	543.4	582.7	
-10.16 cm, 2.54 cm	513.1	526.7	799.6	733.1	536.7	612.2	586.5	604.1	471.1	471.7	616.9	647.6	685.2	554.1	617.6	659.9	
0.0 cm, 2.54 cm	526.3	545.6	752.9	750.0	661.6	630.0	614.8	623.4	493.4	491.5	630.2	661.9	706.8	574.8	630.9	672.1	
10.16 cm, 2.54 cm	490.1	514.8	732.2	726.1	631.6	614.6	580.1	594.6	462.4	459.3	607.8	635.3	665.9	547.3	601.7	651.2	
20.32 cm, 2.54 cm	377.9	389.2	657.9	648.3	554.3	543.3	454.3	520.8	353.3	351.1	535.8	565.7	614.9	400.9	535.8	531.5	
30.48 cm, 2.54 cm	327.1	325.5	455.8	441.6	501.2	460.5	378.9	463.1	313.6	309.2	365.8	376.0	366.4	428.7	376.1	388.1	
VELOCITY, m/sec																	
-30.48 cm, 2.54 cm	81.08	192.69	566.59	565.47	547.17	262.74	89.98	497.85	121.07	121.69	516.45	551.14	990.85	295.99	548.93	503.40	
-20.32 cm, 2.54 cm	371.55	301.48	785.55	774.25	692.23	623.77	532.30	708.48	370.12	368.66	769.64	724.52	751.27	628.97	710.30	732.79	
-10.16 cm, 2.54 cm	398.77	322.46	824.18	817.84	762.00	735.33	595.03	745.21	369.26	364.51	745.05	782.41	794.92	708.98	744.94	763.09	
0.0 cm, 2.54 cm	364.64	320.31	795.01	792.18	703.30	703.30	568.57	710.64	363.23	378.90	717.94	732.40	798.42	669.62	715.01	739.98	
10.16 cm, 2.54 cm	377.92	313.30	806.53	795.41	753.80	709.16	591.46	737.83	379.26	376.09	799.37	749.37	772.90	680.56	732.54	752.86	
20.32 cm, 2.54 cm	337.93	282.70	800.92	787.94	868.66	608.20	518.07	710.32	342.87	335.65	709.95	731.06	766.37	612.89	708.42	743.39	
30.48 cm, 2.54 cm	71.96	86.17	601.65	807.13	137.19	101.71	87.97	285.14	82.94	53.13	515.82	569.97	628.48	129.57	540.20	595.79	
DENSITY, g/m3																	
-30.48 cm, 2.54 cm	0.43971	0.27704	0.25146	0.24212	0.22067	0.20191	0.25843	0.20114	0.26907	0.24828	0.22910	0.21989	0.20911	0.20127	0.14501	0.19658	
-20.32 cm, 2.54 cm	0.34059	0.22426	0.19005	0.19010	0.18753	0.20097	0.20036	0.16967	0.20204	0.20201	0.17838	0.16573	0.18188	0.17752	0.12053	0.12048	
-10.16 cm, 2.54 cm	0.29726	0.19666	0.17411	0.17199	0.15857	0.14797	0.11057	0.15413	0.17443	0.17622	0.16237	0.16813	0.16428	0.12209	0.11051	0.10905	
0.0 cm, 2.54 cm	0.25311	0.19369	0.17494	0.17378	0.15798	0.14874	0.17314	0.15375	0.17057	0.17263	0.15997	0.16665	0.16583	0.14289	0.10928	0.10952	
10.16 cm, 2.54 cm	0.31250	0.20564	0.18303	0.18226	0.15963	0.15747	0.17211	0.15683	0.17943	0.18136	0.16552	0.17577	0.17346	0.14599	0.11470	0.11500	
20.32 cm, 2.54 cm	0.38263	0.25030	0.18277	0.18419	0.18252	0.21276	0.22002	0.16762	0.22002	0.22398	0.17590	0.18005	0.17520	0.16348	0.11971	0.11633	
30.48 cm, 2.54 cm	0.46034	0.31841	0.22156	0.23223	0.21167	0.22311	0.26742	0.19613	0.25056	0.26279	0.19968	0.21691	0.20345	0.19530	0.13656	0.13315	

Table A-1. Continued

TABLE A-1 Rake and Facility Da	Average 71-72	Average 74-75	Average 76-77	79	51	Average 93-94	Average 95-96	Average 98-99	Average 100-101	Average 103-104	Average 105-106	Average 108-109	Average 111-113
SSDP (Data Point Number)													
RNS TIME (HR:MIN:SEC)	13202	13059	13475	14205	14106	14190	14517	12555	16304	19450	16556		17192
ALT (Altitude) (Das)	12.175	12.179	15.272	15.220	15.296	15.269	3.129	3.127	3.125	3.125	3.122	3.123	3.122
VMO (Mach Number)	0.798	0.798	0.801	0.791	0.802	0.798	0.761	0.760	0.761	0.761	0.761	0.760	0.758
P2 (atm)	0.28161	0.28195	0.17372	0.17352	0.17325	0.17326	0.99456	0.99797	0.99928	0.99919	0.99990	0.99837	3.99704
TT2 (K)	244.8	244.7	244.9	244.7	245.0	244.9	258.2	258.5	258.5	258.4	258.4	258.3	258.0
PS4 (atm)	0.16560	0.16546	0.11365	0.11479	0.11342	0.11394	0.68085	0.68004	0.68101	0.68101	0.68124	0.68114	0.68121
P3H (Combustor Inlet P) (atm)	6.33112	3.31679	3.27530	4.01085	5.25672	5.54494	18.74079	13.32994	12.04060	5.15770	4.76523	21.47252	30.46904
T3H (Combustor Inlet Temp) (K)	664.8	656.9	635.1	611.1	732.3	783.9	733.0	688.7	650.8	525.5	517.3	762.2	861.1
FARGH (Core Fuel/Air)	0.0158	0.0116	0.0156	0.0169	0.0191	0.0204	0.0168	0.0153	0.0199	0.0090	0.0095	0.0177	0.0219
FARBDC (Ribbed Fuel/Air)	0.0100	0.0064	0.0065	0.0100	0.0129	0.0141	0.0101	0.0076	0.0072	0.0037	0.0036	0.0111	0.0145
Test Cell Ambient Temp. (K)	293.4	293.2	294.0	293.6	293.8	293.9	298.5	299.3	296.9	297.8	297.5	298.6	299.7
GAMMA													
PROBE 1 TOTAL TEMP (K)	314.0	296.4	352.3	325.5	331.8	324.0	372.0	355.9	348.6	300.5	304.4	358.4	366.8
PROBE 2 TOTAL TEMP (K)	323.1	300.9	360.8	333.6	340.9	352.2	381.0	362.6	355.1	308.2	306.8	368.6	380.1
PROBE 3 TOTAL TEMP (K)	584.7	392.3	546.2	606.0	690.0	740.5	601.5	479.4	458.5	379.2	377.4	649.7	788.7
PROBE 4 TOTAL TEMP (K)	782.5	623.7	760.2	807.8	684.7	926.0	842.2	741.5	715.0	547.1	542.3	896.9	1025.8
PROBE 5 TOTAL TEMP (K)													
PROBE 6 TOTAL TEMP (K)	774.1	833.5	750.6	795.2	873.5	916.8	840.5	751.6	725.5	575.4	575.7	877.5	999.6
PROBE 7 TOTAL TEMP (K)	751.1	580.8	717.6	766.4	840.2	893.8	819.5	716.1	690.4	477.5	467.6	856.7	978.3
PROBE 8 TOTAL TEMP (K)	597.1	965.3	553.5	631.1	722.9	777.0	606.2	457.1	429.9	338.5	334.7	675.5	857.8
PROBE 9 TOTAL TEMP (K)	320.5	300.5	377.7	327.2	349.6	368.9	406.2	377.5	363.8	309.9	300.8	402.0	425.3
PROBE 10 TOTAL TEMP (K)	312.2	296.6	366.0	320.0	326.2	336.1	396.7	373.1	360.8	312.1	306.7	369.3	410.7
GAMMA						61							
(-30.48 cm, 2.54 cm)	1.360	1.369	1.360	1.378	1.373	1.370	1.376	1.363	1.364	1.368	1.368	1.374	1.366
(-20.32 cm, 2.54 cm)	1.354	1.374	1.358	1.352	1.342	1.338	1.350	1.363	1.365	1.379	1.379	1.345	1.331
(-10.16 cm, 2.54 cm)	1.344	1.361	1.346	1.341	1.333	1.330	1.337	1.346	1.350	1.368	1.370	1.333	1.322
(0.0 cm, 2.54 cm)	1.344	1.360	1.347	1.342	1.334	1.330	1.337	1.347	1.350	1.368	1.368	1.334	1.323
(10.16 cm, 2.54 cm)	1.345	1.353	1.349	1.343	1.336	1.331	1.336	1.349	1.352	1.372	1.373	1.335	1.324
(20.32 cm, 2.54 cm)	1.355	1.378	1.360	1.363	1.343	1.338	1.351	1.365	1.369	1.384	1.385	1.345	1.330
(30.48 cm, 2.54 cm)	1.379	1.390	1.379	1.377	1.371	1.367	1.374	1.383	1.385	1.390	1.391	1.371	1.359
MACH NUMBER					61								
(-30.48 cm, 2.54 cm)	1.253	0.339	0.777	1.274	1.392	1.443	0.909	0.218	0.231	0.309	0.274	0.732	1.432
(-20.32 cm, 2.54 cm)	1.550	1.151	1.400	1.564	1.559	1.555	1.356	1.243	1.164	0.706	0.683	1.497	1.554
(-10.16 cm, 2.54 cm)	1.561	1.158	1.492	1.534	1.520	1.525	1.465	1.278	1.208	0.698	0.673	1.537	1.581
(0.0 cm, 2.54 cm)	1.435	1.203	1.412	1.429	1.454	1.461	1.385	1.192	1.240	0.692	0.670	1.404	1.416
(10.16 cm, 2.54 cm)	1.529	1.157	1.447	1.513	1.532	1.521	1.442	1.285	1.203	0.694	0.669	1.507	1.514
(20.32 cm, 2.54 cm)	1.500	1.200	1.366	1.574	1.552	1.560	1.338	1.252	1.196	0.690	0.674	1.528	1.558
(30.48 cm, 2.54 cm)	0.615	0.223	0.319	0.302	1.207	1.455	0.504	0.248	0.213	0.219	0.228	0.660	1.264
PITOT PRESS, atm				79	61								
(-30.48 cm, 2.54 cm)	0.19715	0.18594	0.18032	0.25524	0.37323	0.38725	0.75763	0.60336	0.63306	0.69104	0.69155	0.93911	2.08993
(-20.32 cm, 2.54 cm)	0.05907	0.02437	0.03190	0.41681	0.51404	0.54496	2.11771	1.65665	1.55106	0.93128	0.90692	2.28826	2.09503
(-10.16 cm, 2.54 cm)	0.07913	0.04309	0.05133	0.42093	0.52416	0.55346	2.06164	1.57941	1.57102	0.93369	0.90757	2.28792	2.94345
(0.0 cm, 2.54 cm)	0.06222	0.41052	0.03660	0.39673	0.49020	0.51691	1.87539	1.58620	1.50177	0.92577	0.90093	2.07866	2.63376
(10.16 cm, 2.54 cm)	0.06506	0.42736	0.06231	0.42073	0.52473	0.55494	2.06915	1.67360	1.56710	0.93250	0.90682	2.23312	2.93346
(20.32 cm, 2.54 cm)	0.65409	0.41855	0.36231	0.41236	0.50701	0.53515	2.11601	1.84924	1.53369	0.93676	0.58605	2.26315	2.91852
(30.48 cm, 2.54 cm)	0.22551	0.18628	0.11934	0.12629	0.26899	0.37075	0.75112	0.68012	0.67917	0.64478	0.89485	0.90995	2.00691
STATIC PRESS, atm				79	61								
(-30.48 cm, 2.54 cm)	0.15593	0.17505	0.10802	0.09778	0.12500	0.12245	0.59202	0.65763	0.65604	0.64664	0.65656	0.68144	0.67021
(-20.32 cm, 2.54 cm)	0.17821	0.18986	0.12682	0.11568	0.14514	0.15446	0.74422	0.66306	0.68210	0.67040	0.66634	0.68876	0.82420
(-10.16 cm, 2.54 cm)	0.18090	0.18652	0.10632	0.12194	0.15467	0.16182	0.63153	0.64689	0.66025	0.67982	0.67080	0.66311	0.83549
(0.0 cm, 2.54 cm)	0.20094	0.17243	0.11211	0.12902	0.15555	0.16321	0.64293	0.67992	0.60922	0.67638	0.67060	0.69949	0.88442

Table A-1. Concluded

TABLE A-1. Points and Facility Da	Average T1-72	Average 74-76	Average 76-77	79	81	Average 83-84	Average 86-84	Average 86-95	Average 100-101	Average 103-104	Average 105-106	Average 108-109	Average 111-113
SSDP (Data Point Number)													
(10.16 cm, 2.54 cm)	0.19005	0.18661	0.11510	0.12459	0.15256	0.16365	0.67056	0.54154	0.56114	0.67948	0.57492	0.68604	0.89027
(20.32 cm, 2.54 cm)	0.17820	0.17539	0.12568	0.11377	0.14392	0.15256	0.76151	0.65239	0.64900	0.66297	0.65634	0.59927	0.82762
(30.48 cm, 2.54 cm)	0.17532	0.17991	0.11136	0.11833	0.11200	0.11565	0.58917	0.65188	0.65521	0.66246	0.65597	0.67185	0.68214
STATIC TEMP X													
(10.48 cm, 2.54 cm)	543.6	330.1	406.3	353.4	364.8	364.4	459.2	414.3	462.7	337.8	337.1	462.8	424.8
(20.32 cm, 2.54 cm)	479.5	407.1	483.6	494.3	558.9	591.4	545.7	476.9	470.5	423.1	422.5	554.1	647.9
(10.16 cm, 2.54 cm)	560.2	502.5	547.1	574.3	635.7	687.8	613.7	579.7	571.9	508.7	507.4	634.5	731.8
(N.1 cm, 2.54 cm)	573.5	500.5	559.8	581.8	647.7	679.9	635.5	601.1	569.8	522.4	524.1	662.3	759.4
(10.16 cm, 2.54 cm)	543.3	495.5	537.8	590.5	614.7	653.0	614.0	570.0	560.4	453.1	481.2	626.3	721.0
(20.32 cm, 2.54 cm)	487.0	377.9	475.9	486.3	552.9	582.7	542.5	456.0	459.3	373.6	368.9	546.3	665.4
(30.48 cm, 2.54 cm)	428.1	329.7	454.7	470.7	422.2	412.0	473.8	412.4	393.4	321.2	317.9	496.3	477.4
VELOCITY, m/sec													
(10.48 cm, 2.54 cm)	406.34	124.24	311.98	460.49	541.81	563.26	259.28	112.56	92.17	113.22	100.25	312.59	584.34
(20.32 cm, 2.54 cm)	669.28	461.19	607.54	95.01	723.32	741.24	624.51	156.75	499.61	289.04	279.32	692.48	773.24
(10.16 cm, 2.54 cm)	718.95	517.24	669.00	721.13	750.33	789.74	720.49	695.00	567.81	310.99	303.08	757.44	822.58
(N.1 cm, 2.54 cm)	674.dn	531.91	658.54	662.29	724.08	743.66	683.72	574.43	562.27	313.35	303.00	708.57	761.48
(10.16 cm, 2.54 cm)	700.22	505.68	680.23	703.30	743.82	759.78	700.36	603.20	560.65	302.76	291.50	739.32	792.42
(20.32 cm, 2.54 cm)	673.33	490.11	586.55	684.08	716.46	739.55	313.66	529.19	498.73	265.91	257.85	701.33	779.44
(30.48 cm, 2.54 cm)	253.27	30.73	135.30	133.11	491.55	584.96	261.17	100.37	84.19	78.32	86.35	300.24	597.15
DENSITY, grams/cm³													
(10.48 cm, 2.54 cm)	0.13120	0.14604	0.07514	2.07694	0.09197	0.08786	0.36493	0.44839	0.46320	0.54139	0.55095	0.40454	0.44630
(20.32 cm, 2.54 cm)	0.10505	0.15120	0.07064	0.06615	0.07347	0.07385	0.39577	0.39335	0.41005	0.44820	0.44815	0.35165	0.35995
(10.16 cm, 2.54 cm)	0.09613	0.10609	0.05651	0.08011	0.05872	0.08659	0.29109	0.31885	0.32657	0.37867	0.37986	0.28546	0.32286
(N.1 cm, 2.54 cm)	0.09916	0.09749	0.05854	0.06185	0.06795	0.06708	0.29817	0.32202	0.30242	0.36632	0.36208	0.29837	0.32941
(10.16 cm, 2.54 cm)	0.10070	0.10982	0.06020	0.08294	0.07026	0.07029	0.30898	0.31841	0.33376	0.39785	0.39657	0.30891	0.34926
(20.32 cm, 2.54 cm)	0.10853	0.13345	0.07475	0.08815	0.07360	0.07283	0.30712	0.40472	0.41725	0.50176	0.50324	0.34140	0.35724
(30.48 cm, 2.54 cm)	0.11385	0.15402	0.08897	0.07116	0.07501	0.07657	0.35173	0.44711	0.47311	0.58345	0.58377	0.36082	0.40417

APPENDIX B
EXTRACTIVE GAS ANALYSIS SYSTEM

V. A. Zaccardi, D. G. Gardner, R. P. Howard, D. J. Gonnion,
P. A. Jalbert, J. A. Ready, R. S. Hiers, Jr.

B-1.0 INTRODUCTION

Conventional extractive gas sampling techniques are used for engine emissions certification and thus are accepted as standard methodology (Refs. B-1, B-2, B-3) for characterization of gaseous constituents. The system used for this NASA test program is similar to a system that would be used for commercial aircraft engine emissions certification testing and therefore should provide reliable data for this study and comparisons to optical techniques also used for species concentration measurements.

B-2.0 INSTRUMENTATION

Concentrations of gaseous species contained in the engine exhaust were measured using a suite of gas analyzers mounted outside the test cell. Constituents measured were nitric oxide (NO), oxides of nitrogen (NO_x), carbon monoxide (CO), carbon dioxide (CO_2), oxygen (O_2), and total unburned hydrocarbons (THC). Nitrogen dioxide (NO_2) concentrations reported in the main body were inferred from the difference of NO_x and NO concentration measurements, assuming other oxides of nitrogen were negligible. In addition to gaseous components, measurements of black smoke were measured and reported as smoke number.

A cruciform multi-point rake, described in Appendix A, was used to obtain exhaust samples at individual and combined probe groupings that provided radial profiles of species concentrations as well as spatial averages. An illustration of the rake mounted just inside the test cell diffuser is presented in Fig. 2 of the main text. The cruciform rake was mounted inside the diffuser with the tips of the gas sampling probes located about 12 cm downstream of the nozzle exit plane. The rake system and design of the probes used for sampling are described in Appendix A. Probe locations with respect to the diffuser and nozzle exit area (approximating exhaust flow-field area) are presented in Fig. B-1, a view looking downstream. Probe numbers in Fig. B-1 were used to designate probes sampled during data acquisition. The rake was made of two bars, one mounted vertically and containing only gas sampling probes, and the other mounted horizontally with sampling probes interspersed among Mach/flow angularity (MFA) and total temperature probes. The center of the rake, and thus the horizontal bar, was 2.54 cm above the centerline of the nozzle. The sampling probes were equally spaced at 5.08-cm centers, except for a 10.16-cm distance between the center-most probes (numbers 10 and 28) on the vertical bar. There were six

probes on each radial arm of the horizontal bar and lower radial arm of the vertical bar contained within the exhaust flow field. Only five probes of the upper radial arm of the vertical bar were within the exhaust flow field.

Probes 7–9 and 25–27 were used for measurements of species concentrations in the region surrounding the exhaust flow field where exhaust recirculation gases could interfere with optical technique measurements. Probes 7 and 25 were part of the horizontal bar assembly. Samples at the other locations (outside the exhaust flow field) were extracted through stainless-steel tubing mounted either to the rake braces or other hardware in the test cell.

Gas samples collected at the probes were transported through stainless-steel lines to a gas distribution system. The gas sampling lines (one for each probe) were heated, insulated, and wrapped to maintain the temperature at 422 K. Inside the cell, the sample lines were heated with steam lines. Outside the cell, the lines were electrically heated using heat tape. The total length of the sampling lines from the rake probes to the gas distribution system was about 15 m.

The gas distribution system had four manifolds, one for each radial arm of the horizontal and vertical bars. These manifolds were designated as 90°, 180°, 270°, and 360° as illustrated in Fig. B-2. Each sample line contained a valve that either directed the sample into a manifold, or into a sample bypass line where the sample was discharged and discarded. The output of each manifold was directed to either the AEDC gas sampling instrumentation (discussed here), to the University of Missouri-Rolla Mobile Aerosol Sampling System (UMR-MASS) discussed in Appendix E, or to the sample discharge line. Simultaneous measurements with independent samples were achieved for gaseous and particulate characterization with the restriction that AEDC and UMR would not simultaneously select the same radial arm (manifold). As stated earlier, this arrangement allowed single-point and multiple-point averages for each measurement system simultaneously. The entire gas distribution system was heated and maintained at 422 K.

Gas samples were transported a short distance from the gas distribution system to the suite of gas analyzers through a single heated line. The gas sample was branched into several analyzers simultaneously for test conditions that provided enough flow. Otherwise, measurements were made sequentially by flowing the gas sample into subgroups or individual analyzers.

Manufacturers, instrument model numbers, and span gas concentrations are given in Table B-1 for the analyzers used for measurements of gaseous species in the exhaust samples during this test program. Non-dispersive infrared (NDIR) analyzers (dry) were used for measurements of CO and CO_2 concentrations. An analyzer (dry) using a paramagnetic detector (PMD) was used for measurements of O_2 concentrations. Chemiluminescence (CLD) analyzers (dry) were used for measurements of NO and NO_x, with the sample passed through a catalytic converter for NO_x measure-

ments. One of the two chemiluminescence analyzers failed early in the test period requiring that both NO and NO_x be measured sequentially on the one working analyzer for each data point. Total unburned hydrocarbons (THC) were measured (wet) using a heated flame ionization detector (FID). Except for THC, all measurements were performed on dry samples. Dry indicates that the samples were passed through a gas sample dryer (Perma Pure Dryer-Model PD-1000) before entering the analyzer. A cold mirror dew-point hygrometer was used for real-time monitoring of dryer efficiency and provided humidity correction factors for carbon balance calculations.

National Institute of Standards and Technology (NIST)-traceable calibration gases were used for routine verification and adjustment of the analyzer response for each instrument. Gaseous nitrogen (GN_2) was used to establish the zero or non-response of the analyzer. The primary measurement ranges and calibration gas concentrations used to adjust the analyzer response are presented in Table B-1.

The black smoke meter was a standard Aircraft Gas Turbine Engine Exhaust Smoke Measurement system meeting the requirements of the SAE Aerospace Recommended Practice (ARP1179B, Ref. B-2). The schematic in Fig. B-2 shows the system in relation to the gas analyzers. Gas samples collected by the probe rake were metered through a filter paper. The change in reflectance of the paper due to the smoke particles was related to a smoke number (SN).

B-3.0 DATA ACQUISITION

Maximization of the number of engine test conditions without sacrificing data quality was achieved through diligent real-time examination of the gas sampling data. Strategic data points planned early in the test period provided assurance of engine and gas sampling system stability and radial symmetry in the exhaust flow field. Radial symmetry was observed independently on the vertical and horizontal sampling bars during detailed mapping of the engine core, fan bypass, and intermediate mixed regions at steady-state engine test condition. This level of detail was repeated at priority engine test conditions at each of the several altitudes. Otherwise, the horizontal bar was devoted to gas sampling data, while the vertical bar was devoted to particulate characterization measurements, described in Appendix E.

The ambitious test matrix planned for a single test period required automation of the electronic data acquisition system to provide real-time concentrations for step-by-step decisions throughout the test program. Automation was achieved using LabVIEW* to control data acquisition of each analyzer system. Raw data from the gas analyzers were saved to the hard drive of the data acquisition personal computer (PC) and to the hard drive of the data reduction PC via an RS232 line. The separate computer allowed data reduction without interruption of LabVIEW during analyzer monitoring and data acquisition. The LabVIEW data file was accessed directly by the PC

supporting Microsoft Excel* for immediate data reduction (Fig. B-3). An Excel spreadsheet was used for calculation of the emissions parameters. In addition to reducing raw data voltages to respective species concentrations, preliminary carbon balance calculations were performed for each gas sampling data point. The Excel-calculated emissions parameters were printed immediately and a copy provided for real-time data assessment as explained earlier. The raw voltages and standard deviations of the measured species data set were included in the report for assessment of the analyzer calibrations and sample stability, respectively.

B-4.0 RESULTS

All emissions data are presented in Table B-2 which also contains the performance data required for analysis and designation of engine conditions. The data are presented in order of acquisition during the test period. The first two columns show the sample probe configuration related to the gas sampling data point (DP) number in column three. The radial arms of the cruciform rake are referred to as the left (270°) and right (90°) horizontal arms, and the upper (360°) and lower (180°) vertical arms; abbreviated LH, RH, UV, and LV, respectively. An "x" in the table designates active sampling from the respective probe position (looking downstream), and "o" indicates the probe was not sampled for that data point. The brackets [ ] enclose probe positions within the nozzle exit region. Thus, the first data point in the table indicates that all left horizontal (LH) sampling probes within the exit area were sampled simultaneously for DP6. Probe designators outside the bracket in the first column correspond to probe positions outside the engine exit, but in the same horizontal plane. The physical positions of these probes relative to the nozzle exit plane and entrance lip of the diffuser are given in Fig. B-1. Vertical probes outside the engine exit diameter were not sampled and thus probe designators were not necessary outside the vertical arm brackets in column two.

The clock time for each data point is given in column four. The altitude (ALT), Mach number (MACH), combustor inlet total temperature (T3), and combustor inlet total pressure (P3) relate the data point to the steady-state engine condition. Species concentrations are reported as fractional densities by volume with major species in percent and minor species in parts per million volume (ppmv). The species concentrations $[O_2]m$, $[CO_2]$, $[CO]$, $[C_xH_y]$, $[NO_x]$, and $[NO]$ were measured. The quantities $[O_2]c$, $[H_2O]$, and $[N_2]$ were calculated from the method of carbon balance described in Ref. B-3. Since oxygen values were both measured and calculated, these values were denoted using "m" and "c", respectively. The measured $[O_2]m$ data agree well with the carbon balance calculations. Although agreement does not guarantee accurate data, significant deviation would have indicated a problem for the respective data point. The emission index (EI) for each measured minor species was calculated according to Ref. B-3 with EI(NO) reported as the NO_2 equivalent, as defined in Ref. B-3. The fuel-to-air (fuel/air) ratio and combustion efficiency (percent) were determined by the method of carbon balance for each gas sampling data

63

point. Fuel/air ratios were determined independently from engine performance data for both the engine hot core and mixed core and fan bypass air and are presented in the table for comparisons. Finally, smoke number, measured at only three engine test conditions, are given in the last column. All smoke numbers were less than 1.5, which is within the zero scatter of this technique; thus indicating that smoke was not measurable.

REFERENCES

B-1. Procedure for the Continuous Sampling and Measurement of Gaseous Emissions from Aircraft Turbine Engines, SAE ARP1256, Rev. B, August 1, 1990.

B-2. Aircraft Gas Turbine Engine Exhaust Smoke Measurement, SAE ARP1179, Rev. B, April 19, 1991.

B-3. Procedure for the Calculation of Gaseous Emissions from Aircraft Turbine Engines, SAE ARP1533, April 30, 1982.
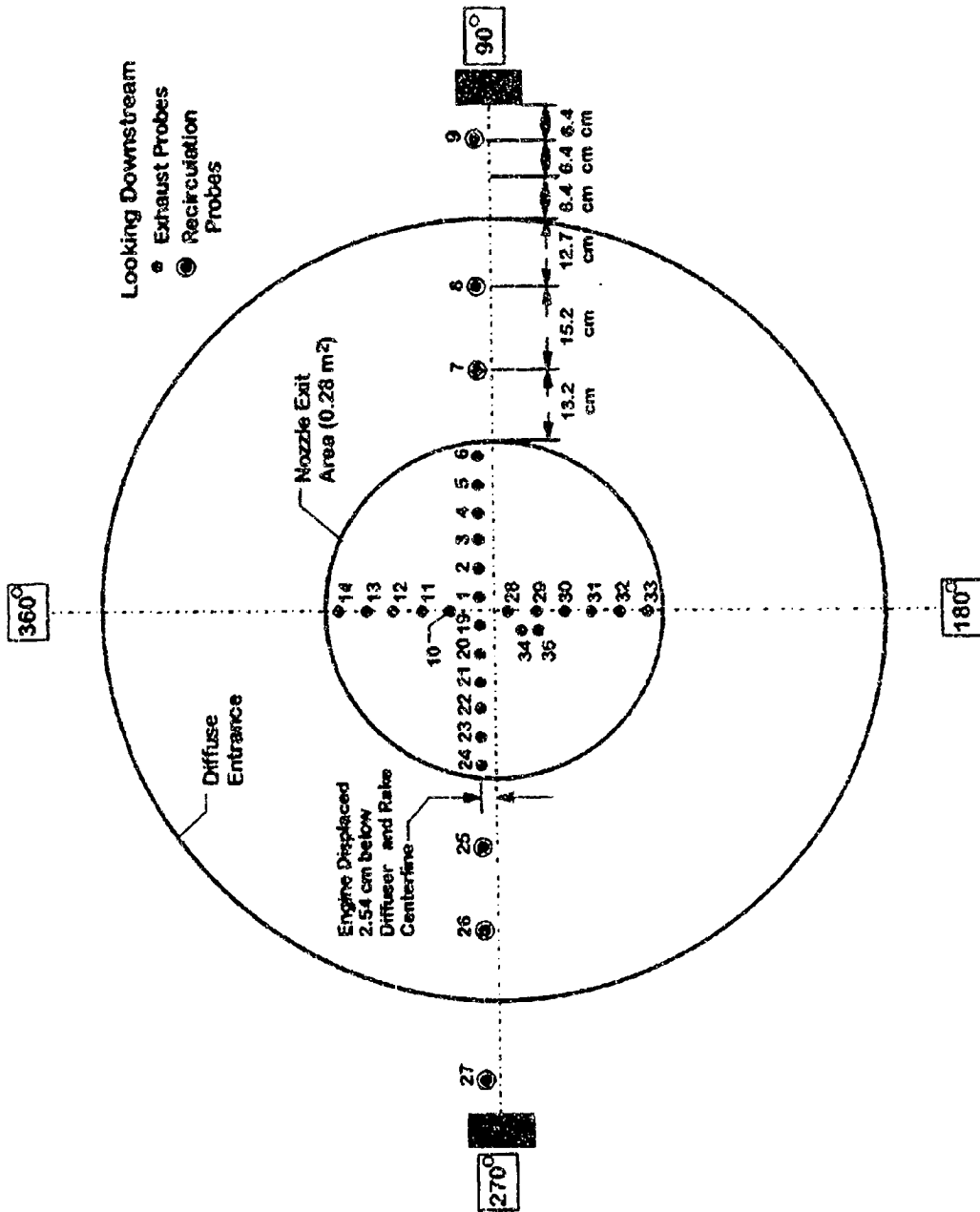
Figure B-1. Gas sampling probe locations near the nozzle exit.

Figure B-2. Typical emissions measurement system schematic.

66
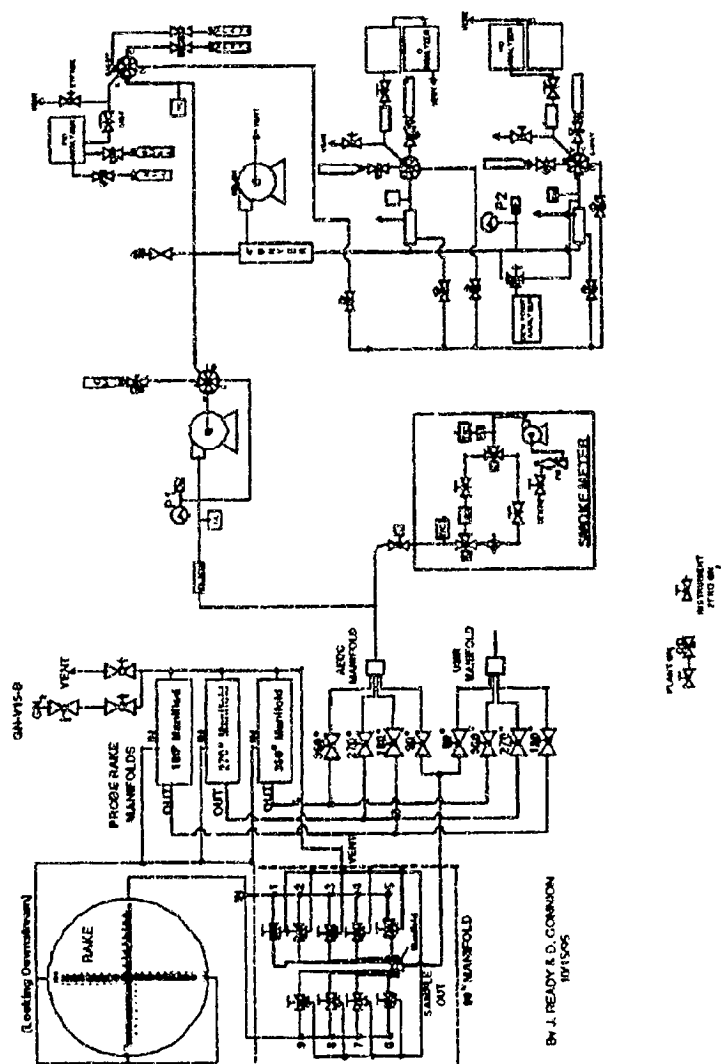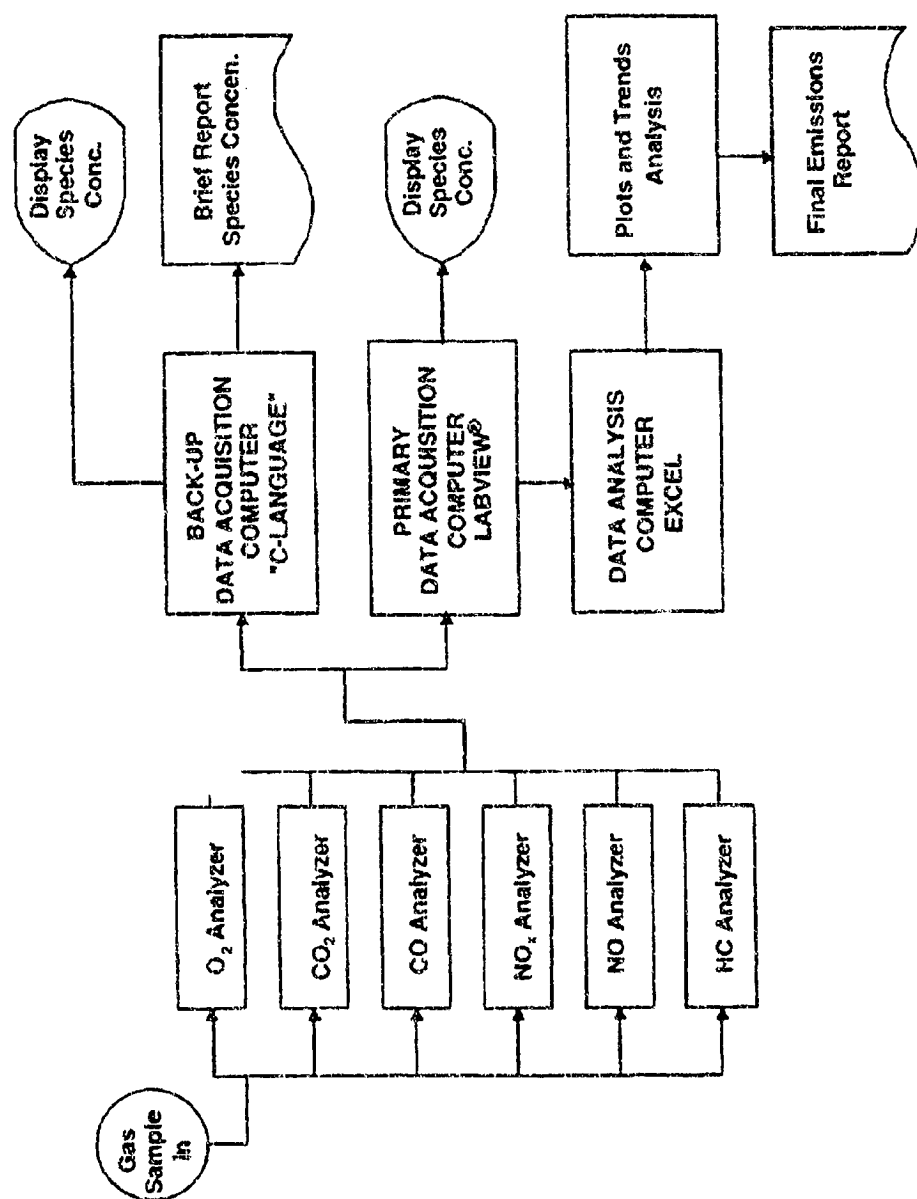
Figure B-3. Data acquisiton and analysis system schematic.

67

Table B-1. Summary of Emissions System Analyzers and Span Gases

TYPE	MODEL	RANGE	CALIBRATION SPAN GAS
CO-NDIR	California Analytical, Inc. Model ZRH	0–1000 ppmv	826 ppmv
CO_2-NDIR	California Analytical, Inc. Model ZRH	0–5 percent	3.99 percent
NO-CLD	Thermal Electron Corp. Model 10	0–25 ppmv 0–250 ppmv	20.3 ppmv 202 ppmv
NO_x-CLD	Thermal Electron Corp. Model 10	0–25 ppmv 0–250 ppmv	20.3 ppmv 202 ppmv
THC-FID	Beckman Model 402	0–100 ppmvC 0–1,000 ppmvC	89.7 ppmvC 885 ppmvC
O_2-Paramagnetic	California Analytical, Inc. Model 5000	25 percent	20.8 percent

Table B-2. Gaseous Emissions and Smoke Summary

Gaseous Emissions and Smoke Data

NOTES:

Data points not given were either voided, acquired during a transition, or were calibration data.
Data points where two point numbers are given had different instruments active at each point.
CP1, P2 and P1C*, SC2, is averaged, not measured.

Gas Delivery Data Point	Time	ALT. m	MACH	TS K	P.T. ATB	Inferred [CO] percent	Measured [CO2] percent	Inferred [O2] percent	Measured [O2] percent	Measured [CO2] percent	Measured [CO] ppm
6	08:27:12	7.6K	0.70	733	9.9	3.04	15.72	15.53	3.17	15.1
7	08:29:30	7.6K	0.70	733	9.9	2.91	16.94	16.83	2.95	14.0
8	08:31:33	7.6K	0.70	733	9.9	3.01	15.74	15.57	3.10	13.7
9	08:34:27	7.6K	0.70	733	9.9	3.04	16.59	16.67	3.13	13.7
10	08:36:38	7.6K	0.70	733	9.9	3.09	16.77	16.55	3.16	14.4
11	08:38:18	7.6K	0.70	733	9.9	0.18	20.84	20.84	0.10	0.8
12	08:43:11	7.6K	0.70	659	7.1	2.59	17.40	17.29	2.58	23.1
13	08:45:50	7.6K	0.70	733	9.9	0.17	20.72	20.84	0.09	0.5
14	09:05:03	9.1K	0.56	513	3.3	1.58	18.51	18.70	1.63	166.6
15	09:08:15	9.1K	0.88	513	3.3	1.64	18.72	18.72	1.61	157.9
16	09:10:34	9.1K	0.90	513	3.3	0.51	20.42	20.21	1.54	40.4
17	09:16:38	9.1K	0.80	733	11.8	3.30	16.29	16.22	3.42	16.9
18	09:17:14	9.1K	0.80	733	11.8	3.37	15.71	15.20	3.44	15.7
19	09:21:09	9.1K	0.80	733	11.8	3.12	16.26	16.19	3.44	16.6
20	09:22:45	9.1K	0.80	733	11.8	3.35	15.25	15.75	3.47	15.1
21	09:24:10	9.1K	0.80	733	11.8	3.26	16.22	16.74	3.46	15.4
22	09:29:51	9.1K	0.80	733	11.8	3.21	16.39	16.28	3.38	14.9
23	09:28:34	9.1K	0.80	733	11.8	2.25	15.42	15.36	3.32	12.2
24	09:32:09	9.1K	0.80	733	11.8	3.44	15.42	15.29	3.36	14.0
25	09:34:48	9.1K	0.80	733	11.8	3.44	15.12	15.01	3.58	
26	09:37:47	9.1K	0.80	733	11.8	2.64	17.30	15.00	2.58	
27	09:41:00	9.1K	0.80	733	11.8	2.53	17.19	17.23	2.70	
28	09:44:10	9.1K	0.80	733	11.8	3.79	18.19	18.07	1.37	5.5
31	09:48:00	9.1K	0.80	733	11.8	3.29	16.35	16.39	3.50	11.8
32	09:43:52	9.1K	0.90	733	11.8	3.14	16.32	16.24	3.41	12.0
33	09:45:51	9.1K	0.80	733	11.8	3.18	16.20	16.16	3.47	12.3
35	09:47:51	9.1K	0.80	733	11.8	3.61	15.53	15.43	3.27	12.4
36	09:52:52	9.1K	0.80	733	11.8	2.51	17.33	17.26	2.67	3.7
37	09:54:48	9.1K	0.80	733	11.8	1.79	18.36	18.48	1.79	6.5
38	09:55:01	9.1K	0.80	733	11.8	2.59	17.93	17.90	2.71	6.3
39	09:57:47	9.1K	0.80	733	11.8	2.59	17.35	17.31	2.64	7.9
40	10:01:43	9.1K	0.80	733	11.9	3.28	16.24	16.42	3.28	
41	10:04:47	9.1K	0.80	733	11.8	3.51	16.27	16.25	3.43	
42/43	10:05:49	9.1K	0.80	733	11.8	0.14	20.75	20.84	0.10	
47	10:10:90	9.1K	0.80	733	11.8	3.15	20.73	20.88	0.07	
53	10:13:15	9.1K	0.80	733	11.8	3.15	20.20	20.87	0.07	
54	10:37:12	9.1K	0.80	733	11.8	3.30	20.72	20.87	0.07	
55	10:39:48	9.1K	0.80	733	11.8	3.31	16.36	18.22	3.82	
56	10:42:38	9.1K	0.80	733	11.8	3.27	16.37	18.21	3.43	16.0
57	10:45:01	9.1K	0.80	733	11.8	3.22	16.45	18.27	3.35	17.6
							16.52	15.54	3.14	12.8

69

Table B-2. Continued

Table B-2. Continued

Table B-2. Continued

Horizontal Rake Left 5 Right 21-25(24-49 + 1-6)7-9	Vertical Rake Upper + Lower (10-14 + 20-37)	Gas Assay Data Point	Time	ALT. m	MACH	TS K	PT ATM	Predicted [H2O] percent	Measured [O2]m percent	Predicted [O2]E percent	Measured [O2] percent	Measured [CO] ppm
		B55	04:54:20	3K (SLS)	0.76	518	4.5	0.33	20.36	20.14	0.09	7.3
		B56	04:55:42	3K (SLS)	0.76	518	4.5	0.58	20.35	20.14	0.45	25.2
		B57	04:59:03	3K (SLS)	0.76	518	4.5	1.58	19.16	19.02	1.40	103.4
		B58	05:08:02	3K (36.5)	0.76	762	2.15	3.31	16.48	16.43	3.27	7.5
		B59	05:10:58	3K (SLS)	0.76	762	2.15	2.61	17.35	17.59	2.50	4.2
		B60	05:14:14	3K (36.5)	0.76	762	2.15	0.50	20.45	20.60	0.27	0.2
		B62	05:23:04	3K (36.5)	0.76	861	30.5	0.47	20.53	20.54	0.73	-0.1
		B63	05:23:10	3K (SLS)	0.76	861	30.5	4.95	15.18	15.11	4.21	7.8
		B64	05:25:40	3K (SLS)	0.76	861	30.5	3.02	16.37	16.87	2.95	6.3
		B65	05:28:43	3K (SLS)	0.76	861	30.5	0.74	20.20	20.25	0.32	0.3
		B66	05:31:13	3K (SLS)	0.76	861	30.5	0.58	20.35	20.48	0.35	0.8
		B67	05:33:72	3K (SLS)	0.76	861	30.5	0.36	20.77	20.79	0.13	-0.7
		B68	05:37:16	3K (SLS)	0.76	861	30.5	4.05	15.44	15.29	4.09	7.3
		B69	05:42:03	3K (SLS)	0.76	831	28.6	3.97	15.57	15.40	4.06	7.1

AEDC-TR-96-3

Table B-2. Continued

Table B-2. Continued

Table B-2. Continued

Table B-2. Continued

Table B-2, Concluded

Ca-AGY Data Point	Measured TC[HA] ppm	Measured [NOx] ppm	Measured [NO] ppm	Inferred [N2] percent	EI[CO]	EI[HC]	EI[NOx] as NO2	EI[NO] as NO2	Carbon Balance Fuel/Air	Combustion Efficiency percent	Fuel/Air Core	Fuel/Air Mixed	Smoke Number
B55	10.5	1.3	1.1	79.07	10.41	0.68	4.84	3.80	0.0023	99.69	0.0066	0.0036	
B56	7.7	7.1	5.6	79.21	14.59	0.49	5.18	3.84	0.0069	99.61	0.0066	0.0036	
B57	7.1	22.7	16.8	79.57	0.35	0.40	19.78	18.32	0.0157	99.98	0.0176	0.0111	
B58	3.4	198.5	185.1	80.28	0.33	0.15	19.82	18.09	0.0121	99.98	0.0176	0.0111	
B59	3.8	151.3	186.1	79.99									
B60	11.2	155	140	79.13									
B62	11.6	24.1	21.8	79.12									
B63	3.1	481.3	482.9	80.63	0.37	0.07	37.34	34.36	0.0200	99.98	0.0216	0.0145	
B64	3.5	335.6	318.1	80.15	0.42	0.12	37.09	35.16	0.0142	99.98	0.0216	0.0145	
B65	9.3	56.1	52.3	79.23									
B66	10.0	34.0	35.3	79.46									
B67	10.2	10.2	11.2	79.04									
B68	3.1	459.2	421.5	80.58	0.06	0.08	36.11	33.70	0.0195	99.98	0.0216	0.0145	
B69	2.7	367.0	336.8	80.55	0.35	0.07	29.93	27.47	0.0191	99.99	0.0195	0.0134	1.3, 1.3

APPENDIX C
NO-UV RESONANCE AND CONTINUUM ABSORPTION SYSTEMS

R. P. Howard and A. G. Davis

C-1.0 INTRODUCTION

Spectral interrogation of nitric oxide (NO) resonance electronic (A←X) transitions using ultraviolet (UV) absorption allows determination of NO density and under appropriate conditions, thermodynamic state. NO-UV absorption techniques, developed in the 1970's (Ref. C-1) for measurements of low NO concentrations in gas turbine combustors and engines, were modified and enhanced in response to new requirements for non-intrusive measurements in high enthalpy test facility flows (Refs. C-2 and 3), exhausts of liquid-propellant rockets (unpublished), and for automobile exhausts (Ref. C-4). The hardware was made robust and more reliable using spectrometer focal plane array detectors, fiber optics, and pulse-start power supplies for the resonance lamps. The line-by-line radiative transfer model, previously limited to the NO gamma (0,0) band, was extended to include the (0,1) band and thus allowed simultaneous determination of NO number density and ground electronic state-vibrational population distribution (reported as ground state-vibrational temperature) in many of the aforementioned applications. Renewed interest in effects of turbine-powered aircraft on atmospheric chemistry has again prompted exhaust characterization studies and new requirements for measurements of NO in turbine engine exhaust.

For this test program, NO-UV resonance and continuum absorption techniques offered in-situ non-intrusive optical measurements of NO number density in the engine exhaust over the full set of operation conditions. The NO-UV line-by-line radiative transfer model coupled to a radial inversion scheme was used to determine radial NO number density profiles from spectral transmission measurements through several chords of the turbine exhaust.

These measurements were sponsored by NASA under the Atmospheric Effects of Aviation Project (AEAP) as a part of a parametric study of exhaust emissions of a gas turbine engine operated over a wide range of engine conditions at each of several simulated altitudes. NO-UV resonance absorption and continuum absorption measurements were made at each steady-state condition. Described here are the measurements, data reduction to transmittances, application of the NO radiative transfer model and inversion scheme for determination of NO number density profiles, and determination of an NO emission index for each steady-state test condition. Descriptions of the engine and facility parameters for each steady-state flight condition are detailed in Section 2.0 of the main text of this report. The resonance and continuum absorption system components were similar except for radiation sources. The system and technique

similarities make it convenient to describe system components, data acquisition, and data analysis for both systems simultaneously while pointing out differences only as necessary.

C-2.0 INSTRUMENTATION

The resonance and continuum system instrument components differed only in lamp types. Primary components per system included a lamp, a lamp shutter with an electronic controller, two fiber optics cables, collimating and focusing optics, a grating spectrometer, an optical multichannel analyzer (OMA$^\varepsilon$) detector system with a computerized controller, and a personal computer for data acquisition and storage. The systems shared stepper motor driven slide tables for traversing the optical beams across the exhaust flow field.

The resonance lamp, a source of NO resonant radiation, was a DC-excited capillary discharge tube operated at 12 ma using a 5,000-V power supply with a 220-kohm ballast resistance. A gas mixture of argon:nitrogen:oxygen, at a 12:3:1 ratio by volume, was flowed through the lamp tube while maintaining a static pressure of 10 torr. The capillary discharge tube was water cooled to tap water temperatures. Resonance lamp intensity characterization is discussed in Section 3.0 below. The continuum system lamp was a constant voltage 100-W, water-cooled deuterium lamp.

Each detector system consisted of a 0.32-m Czerny Turner spectrometer with a variable-width entrance slit, a 2,400 groove/mm grating (used in first order), and an EG&G Princeton Applied Research Model 1421-B silicon-diode array detector. The detector was UV-enhanced and intensified over the full 1,024 pixel elements. The detector and detector controller (model 1461) are referred to as the OMA. The spectral range was 214 to 245 nm with a 0.029-nm per detector-element spectral dispersion and 0.16-nm spectral resolution (full-width-half-maximum). The instrument response function for a single array element, $g(\lambda)$ in Eq. (C-1) of Section C-3.0, is presented in Fig. C-1 for the resonance absorption system.

The spectral region reported for the continuum absorption measurement deserves explanation. First, this measurement system was developed and installed with intentions of measuring OH resonance absorption near 300 nm. After successfully incorporating a UV spectral-scanning laser for OH absorption and having failed to detect OH absorption during an engine checkout run, this system was reconfigured to allow NO continuum absorption measurements. The combination of system spectral throughput (primarily the long fiber cables) and the deuterium lamp characteristics resulted in detector saturation in the region of the (0,1) band for detector integration times required for sufficient signal-to-noise ratio at the (0,0) band. Therefore, the less important (0,1) spectral region was moved off the detector. Also, there was insufficient lamp signal for meaningful measurements at wavelengths below the (0,0) band. The

useable spectral range was about 222 to 228 nm with a 0.029-nm per detector-element spectral dispersion and 0.21-nm spectral resolution (full-width-half-maximum). The instrument response function for one array element of the continuum system, corresponding to g(λ) in Eq. (C-1), is also presented in Fig. C-1.

C-3.0 RADIAL INVERSION-RADIATIVE TRANSFER MODEL AND RELATED PARAMETERS

A computer model based on the theoretical line-by-line radiative transfer for the NO gamma (0,0) band was used to determine NO number density from spectral absorption measurements. The theoretical physics of NO molecular absorption, details of the model, and extension of the model from earlier work can be found in the references (Refs. C-1, 2, 5, 6). A brief overview is presented here to describe and document model parameters used for analysis of the present data. Basically, the fractional lamp radiation within the wavelength interval, Δλ, transmitted through a medium of length, L, is given by the equation of radiative transfer,

$$
\tau_{\Delta\lambda} = \frac{\displaystyle\sum_j \int_{\Delta\lambda} \left(I_C + I_{\lambda_i}^{\circ}(\lambda) \right) e^{-\sum_j \int_L k_{\lambda_i}(\lambda)dL} g(\lambda)d\lambda}{\displaystyle\sum_j \int_{\Delta\lambda} (I_C + I_{\lambda_i}^{\circ}(\lambda)) g(\lambda)d\lambda}
\tag{C-1}
$$

where

$g(\lambda)$ = spectral instrument response function,

$k_{\lambda_i}(\lambda)$ = molecular absorption transition (line),

$I_{\lambda_i}^{\circ}(\lambda)$ = relative intensity of a resonance lamp transition, and

I_c = Lamp radiation factor, modeled as continuum radiation.

The interval Δλ is limited by the spectral extent of g(λ), the spectral response for an individual element of the linear array detector. Absorption in the test media is modeled by molecular absorption transitions, $k_{\lambda_i}(\lambda)$, which are described by Voigt line-profiles that allow for pressure or collision broadening. The summation over i includes all transitions of the NO gamma (0,0) or (0,1) band wholly or partially falling within Δλ. The absorption coefficient is a function of the

79

static temperature, static pressure, directed velocity line center shifts (Doppler shifts), line center pressure shift parameter, broadening parameter (discussed later), and NO number density along the measurement path, L. For a single homogeneous path, the flow-field parameters are input to the model, and the NO number density is varied until the calculated (Eq. (C-1)) and corresponding measured transmittances agree. Calculations were compared to peak absorption at the second bandhead, 226.23 nm and 236.3 nm, respectively, for the (0,0) and (0,1) bands using the resonance lamp and 226.18 nm for the (0,0) band of the continuum absorption technique. The (0,1) band was not measured with the continuum absorption system, as discussed in Section C-2.0.

Absorption media line center shifts with respect to the fixed lamp radiation line positions are important to the NO densities derived from the model. Two shift mechanisms are modeled in the code. Shifts from the Doppler effect were negligible for these measurements due to small exhaust flow velocity components in the direction of the source beam. Collision-induced shifts were modeled according to the collisional shift parameter, $\delta = -0.18^*P(295/T)^{0.56}$, as quantified in Ref. C-7. Here P is static pressure in atmospheres and T is static temperature in Kelvin.

The resonance lamp radiates several lines within the spectral interval, $\Delta\lambda$, of Eq. (C-1). Line intensities, $I_{\lambda_i}^c(\lambda)$, are modeled by Doppler profiles broadened to 950 K. The relative lamp line intensities were measured and characterized according to the upper-state population distribution, Fig. C-2. Results for the (0,0) and (0,1) bands were similar, as expected, since the upper states are common to both bands. The lamp emits low-level radiation (I_c) in addition to gamma band radiation. This radiation was not directly quantifiable from lamp characterization measurements, but was modeled as constant continuum radiation, I_c, over the spectral range, $\Delta\lambda$, with excellent results.

The lamp radiation for the continuum absorption technique was modeled as a simple spectral constant, achieved in Eq. (C-1) by setting $I_{\lambda_i}^c(\lambda)$ to zero and I_c to some arbitrary constant value.

For the resonance technique, the molecular broadening parameter, $a' = C^*P/T^n$, and I_c have been treated as instrument-dependent code calibration factors (Ref. C-2) selected to minimize differences in calculated and measured transmittances at controlled laboratory conditions. Here, C is referred to as the broadening constant and n the temperature-dependent exponent. The broadening parameter, $a' = 31800^*P/T^{1.5}$, was reported in 1981 (Ref. C-5) but did not include a low-level lamp radiation factor. When this technique was reinstated in the late 1980's using the intensified array detector and a modified electronic lamp power supply, the radiative transfer model required a factor, $I_c = 22$, (relative to coded values in Fig. C-2) to accurately match laboratory-measured transmittances down to 0.2. Without I_c, the model

predicted transmittances fairly accurately down to about 0.8 but underpredicted at lower transmittances with increasing deviation. Since I_c had little effect on transmittance calculations above 0.8, a′ was determined from a wide range of laboratory conditions (P and T) approximately independent of I_c. The results for a′ were consistent with the 1981 reported value. Also, a two parameter non-linear least squares fit to all the laboratory data with the temperature exponent, n, fixed at 1.5 gave $I_c \approx 22$ and again a′ consistent with the 1981 values. The study concluded that radiative transfer model calculations and laboratory data were in great agreement over the full range of laboratory conditions for $I_c = 22$ and a′ = $31800*P/T^{1.5}$. In recent years, the broadening parameters for individual lines have been measured directly (Ref. C-7) and reported as a′ = $6927*P/T^{1.25}$. It is both important and gratifying that this agrees extremely well with a′ = $31800*P/T^{1.5}$. Using the Ref. C-7 value in the code, $I_c = 22$ was still the best fit value. Relative to the Fig. C-2 lamp characterization values, I_c and a′ were about equivalent for both the (0,0) and (0,1) bands.

The instrument-dependent code calibration parameter, a′, was determined independently for the continuum absorption system using continuum lamp transmittance measurements over a similar range of laboratory measurements. For the continuum absorption system, the broadening constant, C = 23250, gave the best overall fit to laboratory data with the temperature-dependent exponent, n, fixed at 1.5.

A radial inversion scheme, referred to as an onion peel, was used to determine a radial profile of NO number density from a series of LOS measurements made at several radial locations, as illustrated in Fig. C-3 during a steady state-test condition. The flow field was modeled as concentric "homogeneous" zones, one for each measurement. The density in the outer zone was determined using the outermost measurement. Stepping inwardly, a new zone NO density was determined for each successive measurement. The static temperature and static pressure along the optical path were inferred from probe measurements as discussed in Appendix A. Probe measurements at similar radial positions on opposite sides of the plume were averaged and radial symmetry then assumed. Measurements of ambient test cell temperature were assigned to positions beyond the lip of the diffuser, and ambient pressure assigned to radial positions just beyond the nozzle exit radius, Re = 30 cm. Radial distance was normalized to the nozzle exit radius so that the extent of the engine exhaust was R/Re = 1.0 or a little beyond, depending on exhaust expansion for each test condition. The probe measurement grid was sparse, and thus interpolation was required to determine the path average temperature, pressure, and axial flow velocities for each homogeneous zone along each LOS measurement path. Averages were area weighted over the width of the optical beam within respective zones. Figure C-4 shows representative plots of zone-averaged temperatures, pressures, and axial velocity for an LOS through the center of the exhaust. Probe-inferred values used to determine the zone averages are superimposed on the plot. These data were acquired for the engine test condition described by

81

the combustor inlet temperature T3 = 733 K at 9.1-km altitude. Refer to Table 3 in the main text for summarized engine/facility test conditions. The zone path segments are obvious in the plot with approximately 2.54-cm segment lengths from the center to just outside the exhaust flow field, and about 5.08-cm segment lengths in the test cell gas-recirculation region. Zones beyond the nozzle exit radius represent measurements through the test cell air, which contained small quantities of recirculated exhaust gases.

C-4.0 TEST CELL INSTALLATION AND MEASUREMENTS

The relative placement of the NO-UV instrumentation and optical beam paths relative to other measurement and facility components in the test cell are illustrated in Fig. 2 of the main body of the report. Preliminary measurements during engine checkout verified that recirculated exhaust gases containing NO would be present at low levels in the test cell. Since even low levels of NO over rather long paths can have a significant effect on the results, measurements were also performed outside the exhaust flow field to quantify recirculated NO concentrations. Quantification, of course, assumed cylindrical symmetry for recirculated gas components surrounding the exhaust flow field.

The source radiation was transmitted through a 9-m length, 400-μm-diam, fused silica fiber to a collimating lens mounted onto a traversing table near the engine exhaust. The radiation was imaged through the exhaust to an aluminum-surfaced mirror (mounted on a second traversing table) and reflected back through the exhaust to a second lens-fiber combination mounted on the traversing table. The beam diameter was approximately 2 cm. The transmitted and reflected beams were within the first 12 cm of exhaust from the nozzle exit plane. The resonance lamp beam was about 6.35 cm above that of the continuum lamp. The reflected radiation was transmitted to the entrance slit of the spectral detector system. All optical lenses and fibers were made of UV grade fused silica.

The slide tables traversed the collimated beam across the flow field in a plane parallel to the nozzle exit plane, as illustrated in Fig. 2 of the main text. Each set of traversed data, for the resonance absorption system, consisted of measurements through the purged path at the top of the diffuser (with and without the shutter closed) and measurements at fixed radial positions from R = 70 to 36 cm in 5.08-cm increments and from R = 36 to 0 cm in 2.54-cm increments. The set of continuum absorption measurement positions were offset about 6.35 cm below the resonance absorption measurements, except, of course, for measurements through the purged tube. A traversing system output voltage was monitored by each OMA system for posttest determination of memories (spectra) acquired while the tables were in motion.

During an earlier engine checkout run, measurements with the lamp shuttered were found

to be indistinguishable from background signal levels. Therefore, acquisition time was significantly reduced by not shuttering the lamp except at the centerline position. These centerline data were used to verify that exhaust radiation levels were negligible for each engine condition. It is also significant that the measurements were not affected by ambient lights within the test cell. Background levels were primarily integrated detector noise as discussed in OMA operation manuals.

C-5.0 DATA REDUCTION

Spectral lamp transmission measurements, $I_T(\lambda_i)$, at a particular LOS (radial) position were reduced to spectral transmittance according to the equation

$$\tau_{\Delta\lambda} = \frac{I_T(\lambda_i) - I_e(\lambda_i)}{I_0(\lambda_i) - I_b(\lambda_i)} \approx \frac{I_T(\lambda_i) - I_b(\lambda_i)}{I_0(\lambda_i) - I_b(\lambda_i)} \qquad (C-2)$$

where λ_i denotes the spectral center of the ith element of the detector array. $I_0(\lambda_i)$ and $I_b(\lambda_i)$, respectively, are measurements of lamp reference and background at the purged path location. As mentioned earlier, measurement of lamp-shuttered signal levels at the exhaust, $I_e(\lambda_i)$, were indistinguishable from background, so $I_e(\lambda_i)$ can be approximated by $I_b(\lambda_i)$. Lamp and transmittance spectra (background subtracted) are presented in Figs. C-5 and C-6 for the resonance and continuum absorption systems, respectively. Prominent NO gamma band regions are labeled in the figures. Absorption features at the (0,0) band are readily evident, but further corrections were necessary to remove position-dependent lamp signal variations and attenuation effects of the exhaust and gas recirculation. These effects are exhibited as overall attenuation at spectral regions away from the (0,0) band absorption feature. A curve fit through spectral regions just above and below the (0,0) band feature served as the base line to quantify (0,0) absorption, as illustrated by the "corrected" curve in Figs. C-5b and C-6b. Thus, the transmittance at the second bandhead of the NO gamma (0,0) band can be read directly from the "corrected" curves.

Formerly, spectral bandhead transmittances were determined using pretest lamp reference spectra acquired at each radial position and then corrected for test media attenuation effects. Data were reduced both ways and gave equivalent results; i.e., differences in second bandhead transmittances from the two processes were far less than statistical uncertainties. The purged-path lamp spectra allowed an independent measure of lamp reference per data set and all the advantages that go with measuring lamp reference spectra within seconds of acquiring transmission measurements. Statistical uncertainty is discussed later.

Resonance absorption system radial profiles of (0,0) second bandhead transmittance, acquired at the five engine power settings at 9.1-km altitude, are presented in Fig. C-7a. These

83

profiles were smoothed using a linear 3-point smoothing algorithm before insertion into the radial inversion scheme. The two bottom curves, almost coincident, show smoothed and unsmoothed transmittance profiles for the same engine test point, illustrating representative affects of the smoothing algorithm on these profiles. Although random-like variations were reduced, changes in transmittance values were generally much smaller than statistical measurement uncertainty. Multiple sets of transmittance profiles were acquired at engine conditions held at steady state for several minutes. Several sets of transmittance profiles acquired at the same engine condition were extremely repeatable with variations less than statistical measurement uncertainty. Multiple transmittance profiles acquired during a steady-state test condition were averaged before application of the radial inversion.

Continuum absorption system radial profiles of second bandhead (0,0) transmittance, also acquired at the five engine power settings at 9.1-km altitude, are presented in Fig. C-7b. Comparing these profiles with resonance absorption profiles in Fig. C-7a, it is obvious that the continuum absorption system was less sensitive to equivalent NO density at the same test conditions. Additionally, continuum absorption was not observed for several low-power engine settings which produced low NO densities. Preliminary results on selected data sets indicate higher uncertainties than results obtained from the resonance absorption data. The higher quality and more complete resonance absorption data were analyzed and reported herein. The continuum absorption data will be further reduced and analyzed for publication in a later report.

C-6.0 ANALYSIS AND RESULTS

The radiative transfer model, Eq. (C-1), incorporated into the onion-peel radial inversion scheme was applied to radial transmittance profiles for each steady-state engine test condition. Static temperature and pressure profiles, required for the radiative transfer model, were inferred from probe and facility measurements and averaged along "homogenous" zones for each LOS optical path. This measurement technique determined NO number density (molecules per volume) profiles. For a more direct comparison to probe sampling measurement profiles, radial NO-UV number density (cm^{-1}) profiles were converted to volumetric fractions (parts per million by volume, ppmv) using the ideal gas law. Profile comparisons are presented in Figs. C-8 through C-10 for the same combustor temperature setting, T3 = 733 K, at three different altitudes, 3.1 (SLS), 9.1, and 12.2 km, respectively. The NO-UV densities tend to be similar in shape to the sampling, but lower by 10 percent for 9.1 and 12.2 km, and about 18 percent for SLS. The stronger deviation might be expected at higher engine power settings for the SLS condition because of the combined effects of greater quantities of NO recirculation in the test cell and possible non-radial symmetries (especially top to centerline) in the recirculation region.

The more direct comparisons of density profiles were limited to the few test conditions for which spatial probe sampling profiles were measured. For comparisons over the full set of test conditions, emission indices were calculated from NO-UV resonance absorption density profiles, aerodynamic flow-field properties derived from the rake data, and fuel flow rates measured by the test facility. An NO emission index EI(NO), using the molecular weight of NO_2, was determined for each engine condition according to

$$EI(NO) = \frac{1000 * M_{NO_2}}{N_A * (\text{fuel flow rate})} \sum_{j} (n_{NO})_j \, V_{xj} A_j \qquad (C\text{-}3)$$

where N_A is Avogadro's number and M_{NO_2} is the gram molecular weight of NO_2. The quantities n_{NO_j} and Vx_j are average zone NO number density and exhaust velocity, respectively, and A_j is the zone area. These EI(NO) values are presented here in Table 5 and in Figs. 13–17 in Section 4.0 of the main body of the report for comparisons to probe sampling and infrared tunable-diode laser technique results.

UV EI(NO) values were in good agreement with probe sampling data, matching well within respective uncertainty bands. However, NO-UV EI(NO) values were usually lower throughout the test. This is consistent with the density profiles compared earlier. A contribution of uncertainty not yet addressed in these comparisons relate to aerodynamic flow-field properties determined from rake data. As mentioned, total temperature and Mach/flow angularity probes were sparsely spaced giving a coarse definition of property profiles. The slow varying nature of these properties across the exhaust flow field gives good confidence in values reported, except near the edge where changes are more abrupt, especially in velocity. The product of velocity and large zone area near the edge can result in a variation of a few percent of EI(NO) in Eq. (C-3) calculations, for just centimeters uncertainty in the radial position for which velocity drops abruptly.

An engineering statistical analysis process, described in Ref. C-8, was applied to steady-state test conditions for which several repeat measurements were performed to give confidence bands for the NO-UV resonance absorption results. Lamp reference and position-wise lamp transmission spectra were treated as independent measurements with random statistical uncertainty. The variance-covariance matrix developed for a set of profile transmittances took into account codependency on lamp reference spectra, curve-fit correction factors, and the linear smoothing algorithm. Measurement uncertainty and a matrix of partial derivatives of NO number density with respect to transmittance for each zone of each LOS measurement path produced one sigma variances for NO number densities at each radial location per set of data.

85

Independently, statistical analyses were performed on the multiple data sets acquired at steady-state engine conditions, treating each set of spatial transmittances as independent measurements with random uncertainty. The resulting NO number density uncertainty was similar, tending to validate assumptions used for the lengthy and tedious engineering statistical analysis process required for single data sets for many of the engine conditions.

The position-wise number density uncertainties within the exhaust flow for several test conditions investigated ranged from ± (6 to 18) percent, with the higher uncertainties relating to data at upper T3 values for the simulated sea-level-static (SLS) condition. Statistical uncertainty on position-wise densities determined for the recirculation region were on the order of ± 15 to ± percent. Statistical uncertainty for emission indices ranged from ± (7 to 13) percent assuming accurate velocities from the rake data.

For completeness, resonance absorption was also observed at the (0,1) band for a couple of the higher temperature conditions. Absorption at this band and the (0,0) band will allow simultaneous determination of NO density and ground-state vibrational temperature (which in this case should be equivalent to kinetic gas temperature) in the inversion process. Results of this analysis will be detailed in a later report.

C-7.0 SUMMARY AND CONCLUSIONS

NO-UV resonance absorption measurements were performed at all test conditions throughout the test period consisting of several engine power settings at simulated altitudes ranging from SLS to 15.2 km. Spectral transmission measurements at multiple radial stations across the exhaust flow field and surrounding region containing low-level recirculated exhaust gases were radially inverted to provide radial profiles of NO number density without prior assumptions on radial species concentration profiles, required for analysis of single line-of-sight optical measurements. Radial NO number density (cm^{-3}) profiles were converted to radial profiles of concentrations (ppmv), and subsequently to emission indices, using radial profiles of static temperature, static pressure, and exhaust flow velocity inferred from probe rake data. The NO emission index is a single value for an engine test condition.

The NO-UV measurement system proved to be reliable and robust. Measurements were extremely repeatable during steady-state test conditions, indicating temporal stability of engine and test facility parameters.

NO-UV radial concentration profiles were compared with radial profile gas sampling data and agree well (within uncertainty limits) with probe sampling measurements, for both the exhaust flow field and the surrounding gas-recirculation regions. The NO-UV concentrations tended to be lower than probe sampled levels within the exhaust region. NO emission indices determined from NO-UV profile concentrations deviated only a few percent from the probe sampling results.

The NO-UV resonance absorption technique performed well throughout the test program, produced results consistent and in good agreement with probe sampling and infrared tunable-diode laser techniques, and is recommended for future test measurement programs.

REFERENCES

C-1. Few, J. D., McGregor, W. K., and Glassman, H. N. "Resonance Absorption Measurements of NO Concentration in Combustor Exhausts." AIAA Progress in Astronautics and Aeronautics-Experimental Diagnostics in Gas Phase Combustion Systems. B. T. Zinn, ed., AIAA Press, Princeton, NJ, 1977.

C-2. Howard, R. P., Dietz, K.L., McGregor, W.K., and Limbaugh, C.C. "Nonintrusive Nitric Oxide Density Measurements in the Effluent of Core-Heated Airstreams." AIAA 21st Fluid Dynamics, Plasma Dynamics and Lasers Conference, AIAA-90-1478, June 18–20, 1990, Seattle, WA.

C-3. Roberts, W. L., Allen, M. G., Howard, R. P., et. al. "Measurement and Prediction of Nitric Oxide Concentration in the HYPULSE Expansion Tube Facility." 18th AIAA Aerospace Ground Testing Conference, June 20–23, 1994, Colorado Springs, CO.

C-4. Howard, R. P. and Phillips, W. J. "UV Absorption Technique for Monitoring Mobile Source NO Emissions." 86th Annual Meeting & Exhibition, June 14–18, 1993, Denver, CO.

C-5. Few, J.D. and Lowry, H. S., III. "Reevaluation of Nitric Oxide Concentration in Exhaust of Jet Engines and Combustors." AEDC-TR-80-65, August 1981.

C-6. Davis, M.G, McGregor, W. K., and Few, J. D. "Utilizing the Resonance Line Absorption Technique to Determine the Collisional Broadening Parameters of a Diatomic Molecule: NO γ-Bands as an Example." Journal of Quantitative Spectroscopy and Radiative Transfer, Vol. 16, No. 12, December 1976, pp. 1109–1118.

C-7. Chang, A. Y., DiRosa, M. D., and Hanson, R. K. "Temperature Dependance of Collision Broadening and Shift in the NO $A \leftarrow X$ (0,0) Band in the Presence of Argon and Nitrogen." Journal of Quantitative Spectroscopy and Radiative Transfer, Vol 47, No. 5, 1992, pp. 375–390.

C-8. Limbaugh, C. C. "An Uncertainty Propagations Analysis for an Infrared Band Model Technique for Combustion Gas Diagnostics." AEDC-TR-76-155, April 1977.
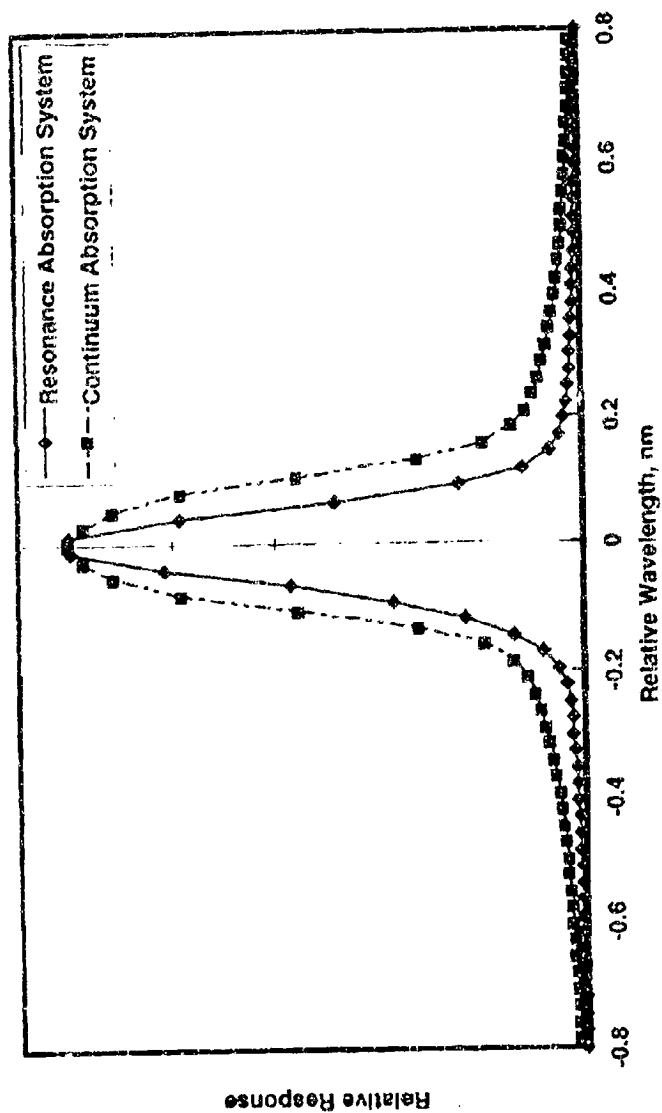
Figure C-1. Instrument response function.

Upper-State Total Energy, cm^{-1}
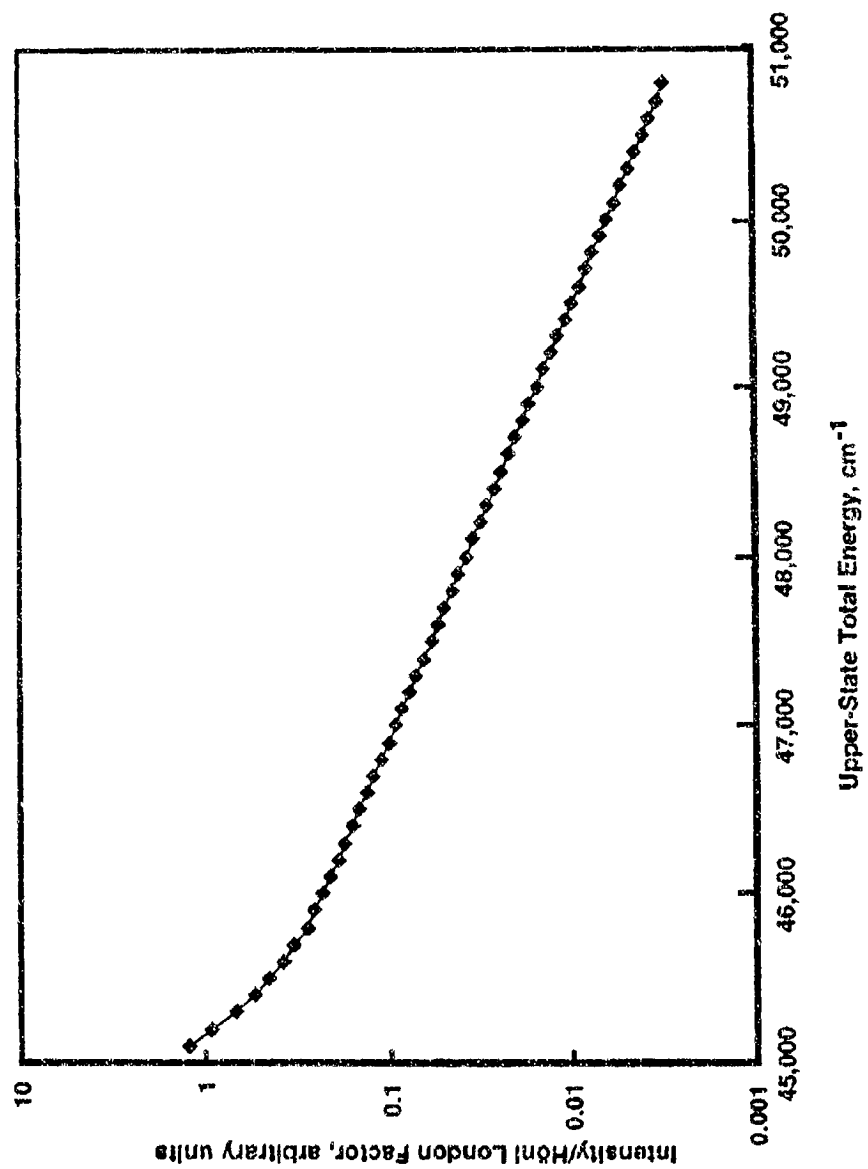
Figure C-2. Resonance lamp line intensity distribution.

89
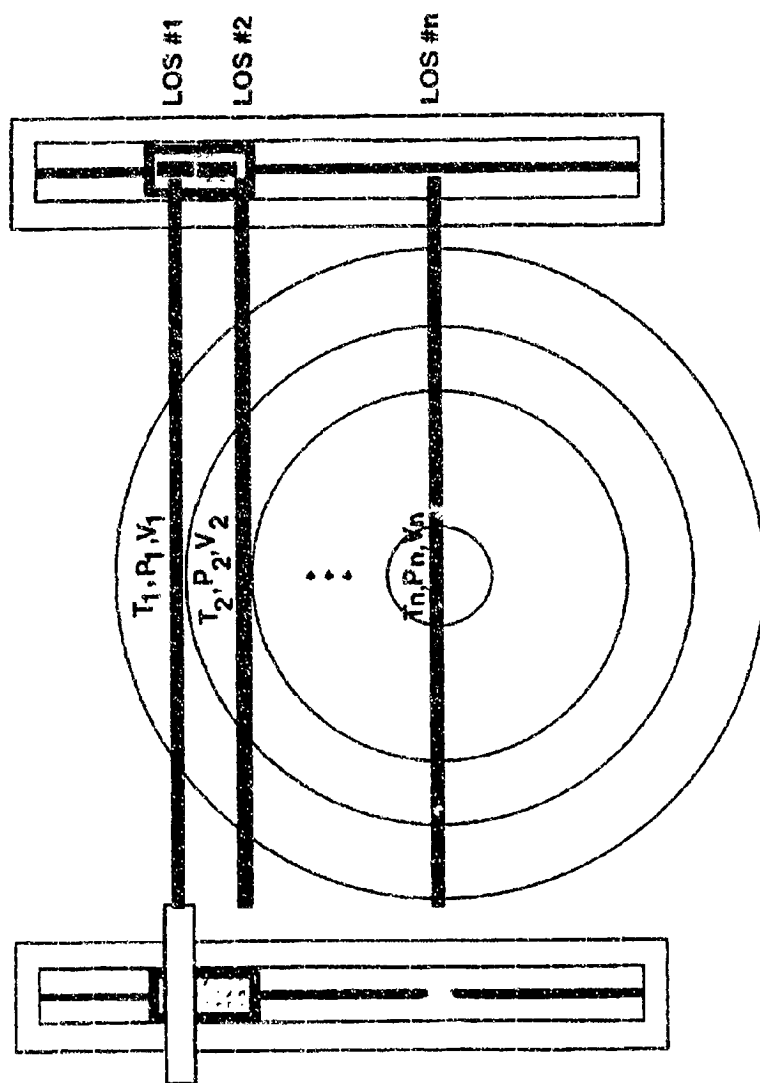
Figure C-3. Measurements through homogeneous zones.
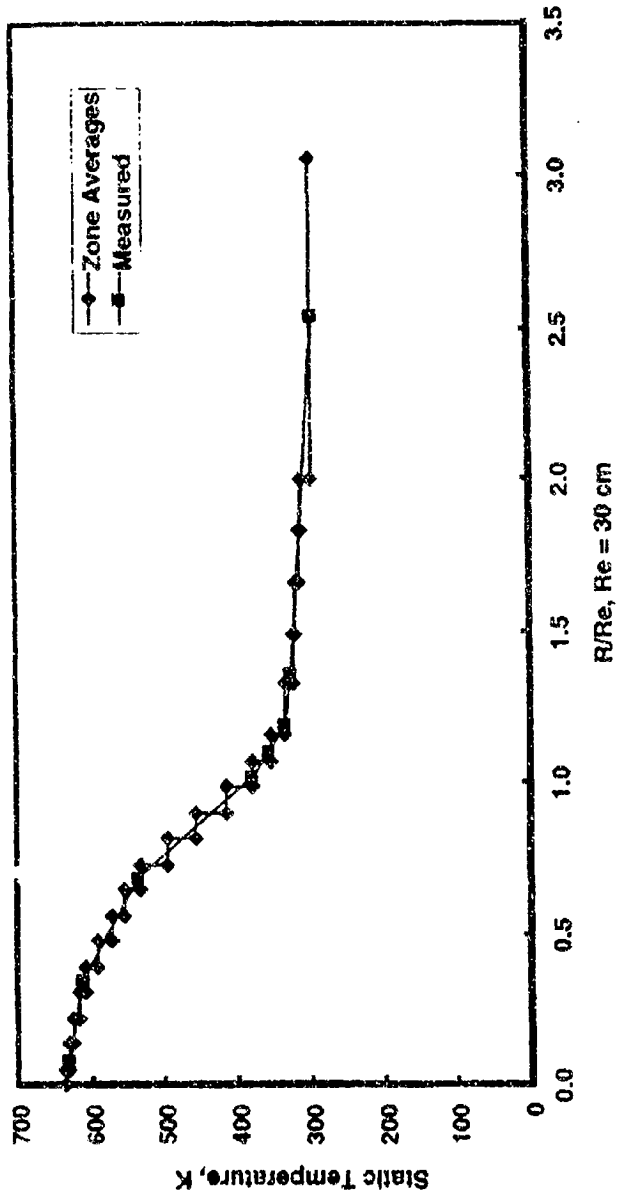
a. Static temperature

Figure C-4. Measured and zone-averaged optical path characterization profiles.
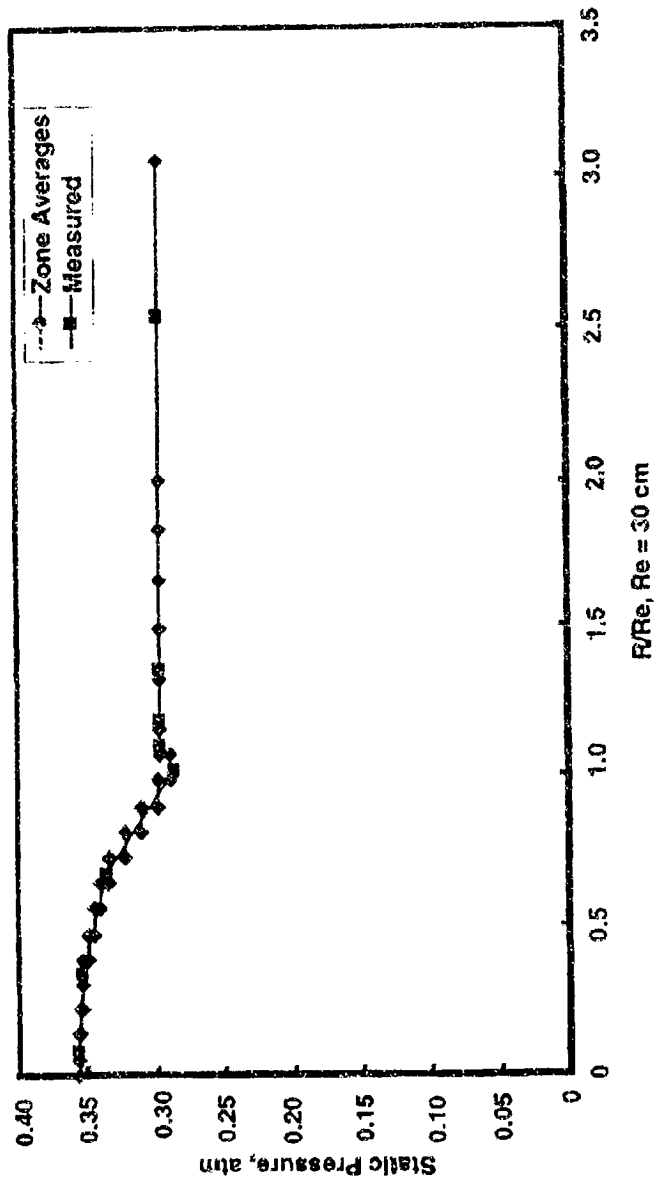
b. Static pressure
Figure C-4. Continued.
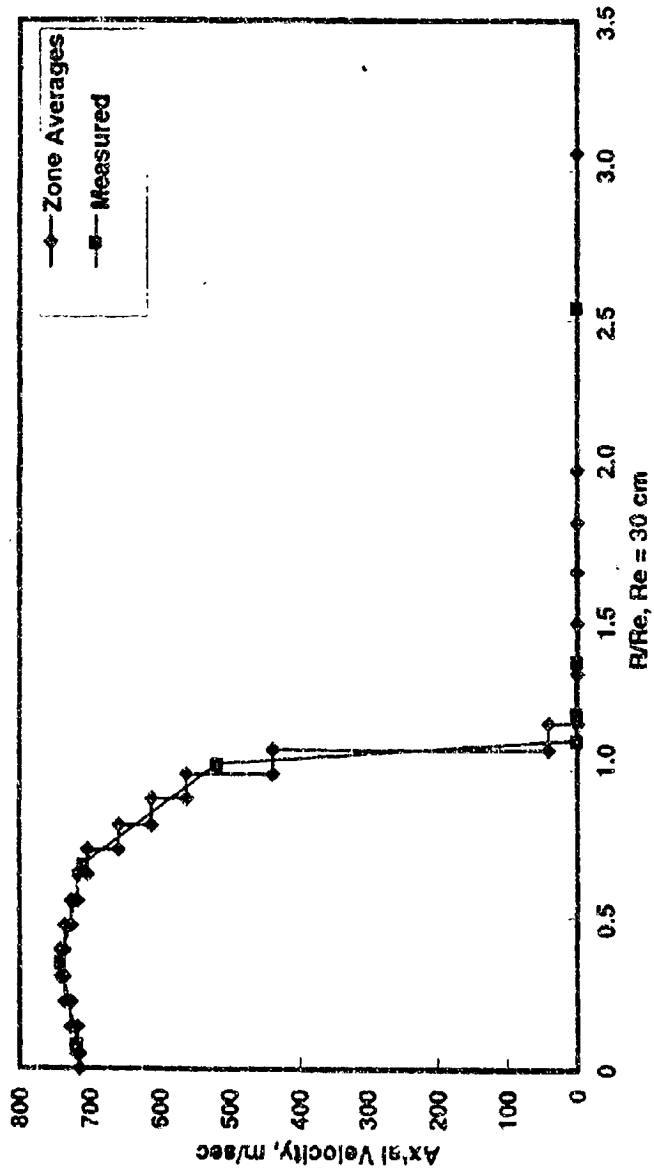
c. Velocity
Figure C-4. Concluded
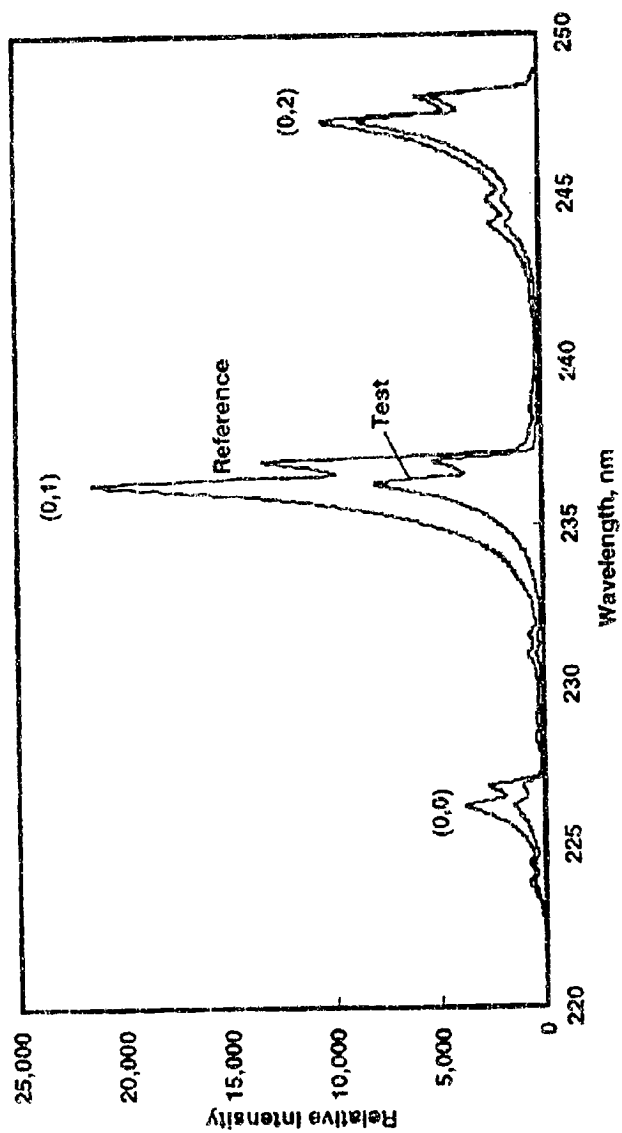
a. Lamp spectra

Figure C-5. Resonance absorption system spectral data.

94
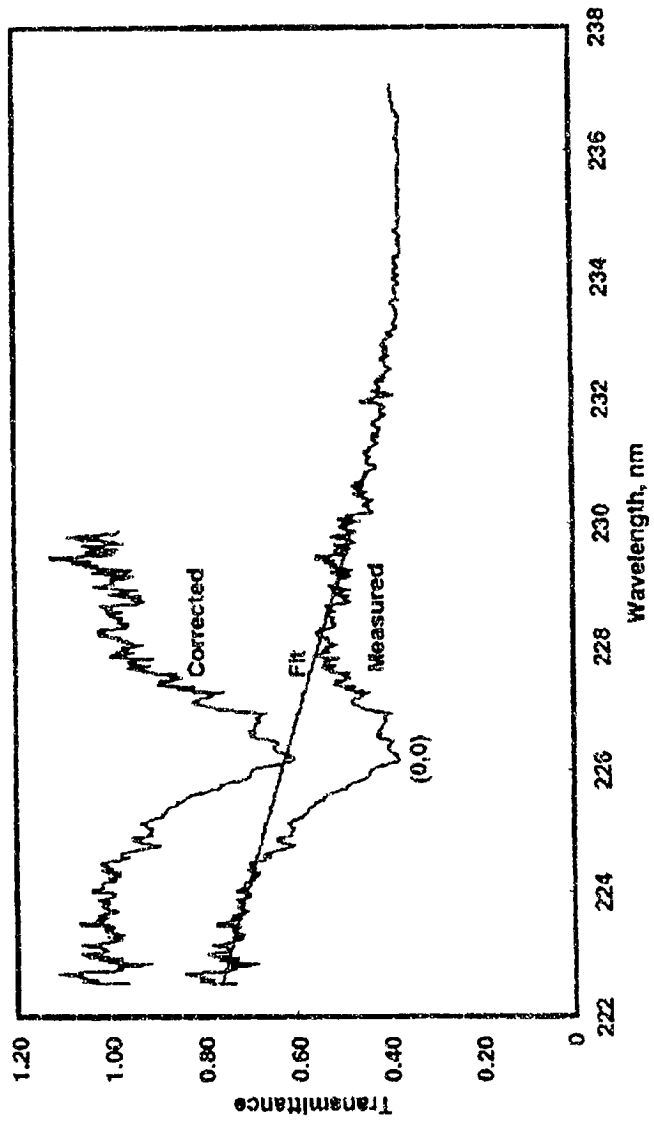
b. Spectral transmittance
Figure C-5. Concluded.
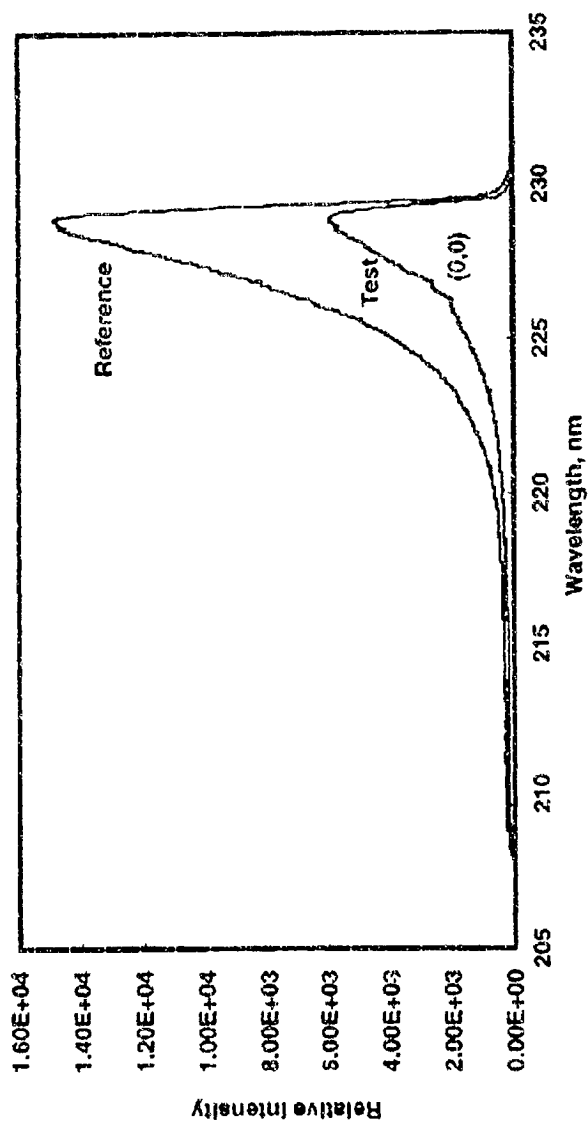
a. Lamp spectra

Figure C-6. Continuum absorption system spectral data.
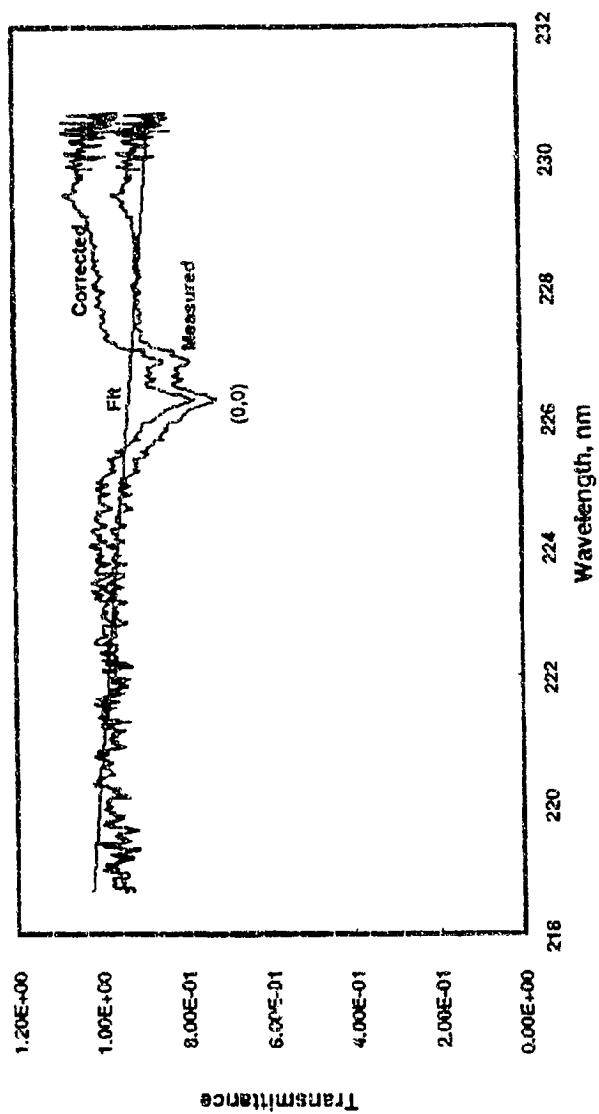
h. Spectral transmittance
Figure C-6. Concluded.

97
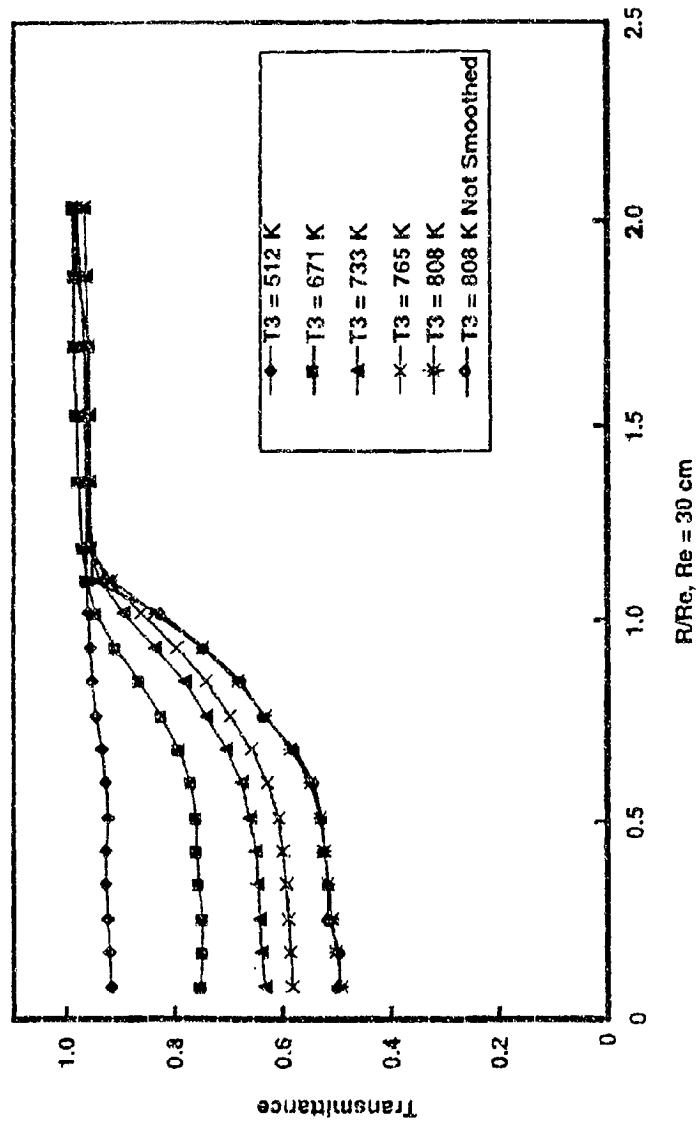
a. Resonance absorption system

Figure C-7. Radial profiles of (0,0) transmittance at 9.1-km altitude.

98
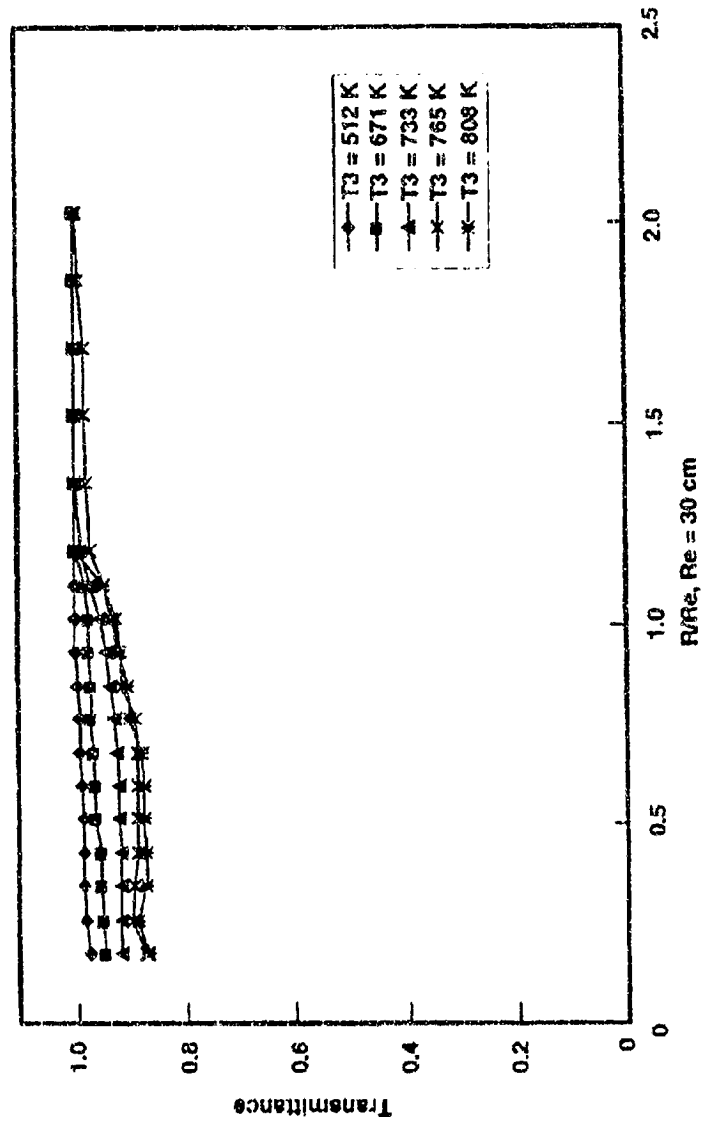
b. Continuum absorption system
Figure C-7. Concluded.
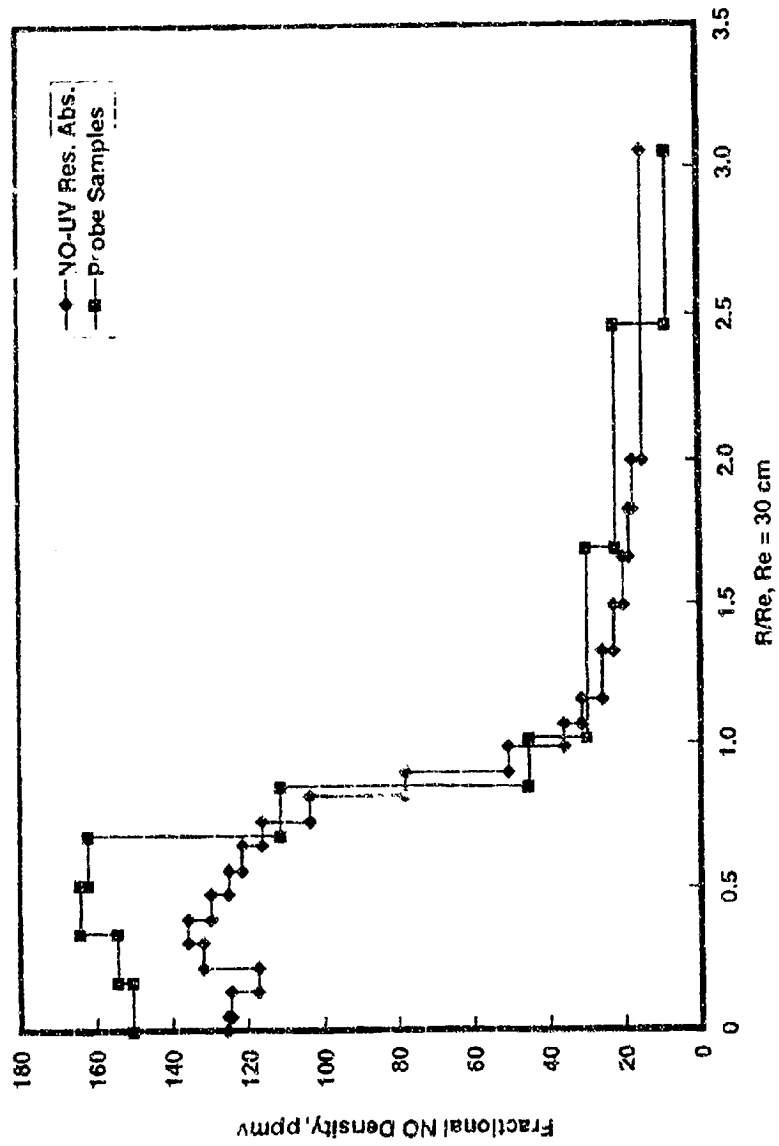
Figure C-8. Resonance absorption and probe sampling radial profiles of NO density for T3 = 733 K and 3.1-km (SLS) altitude.
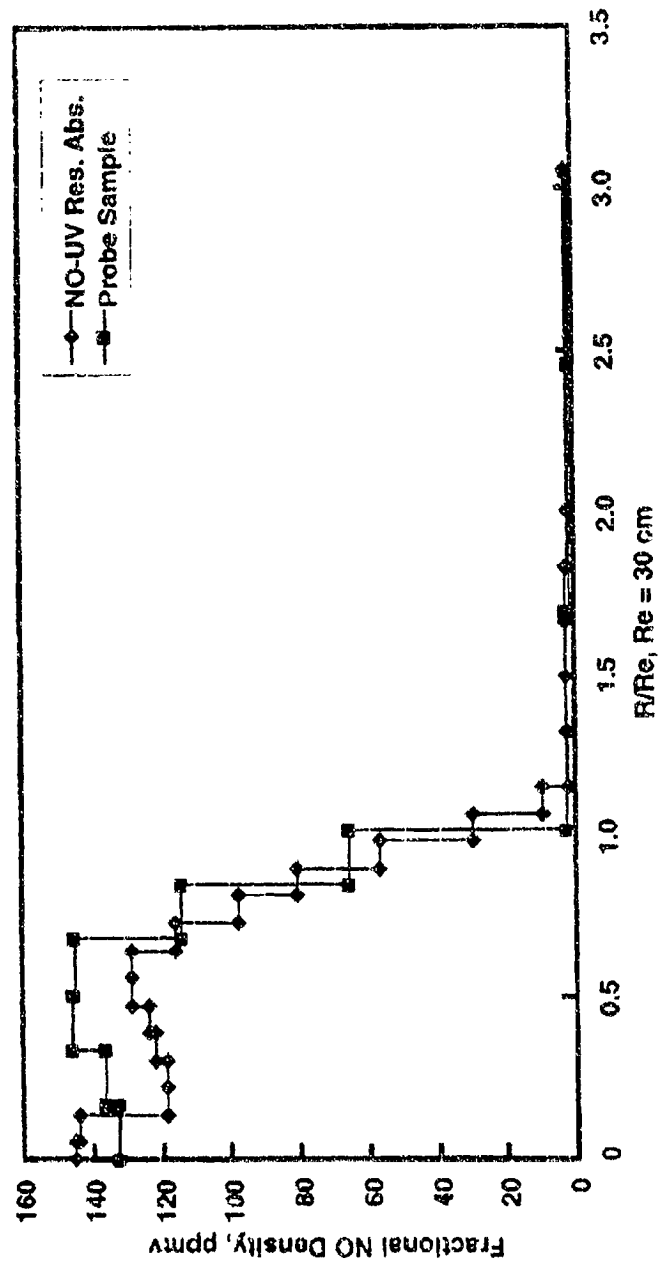
Figure C-9. Resonance absorption and probe sampling radial profiles of NO density for T3 = 733 K and 9.1-km altitude.
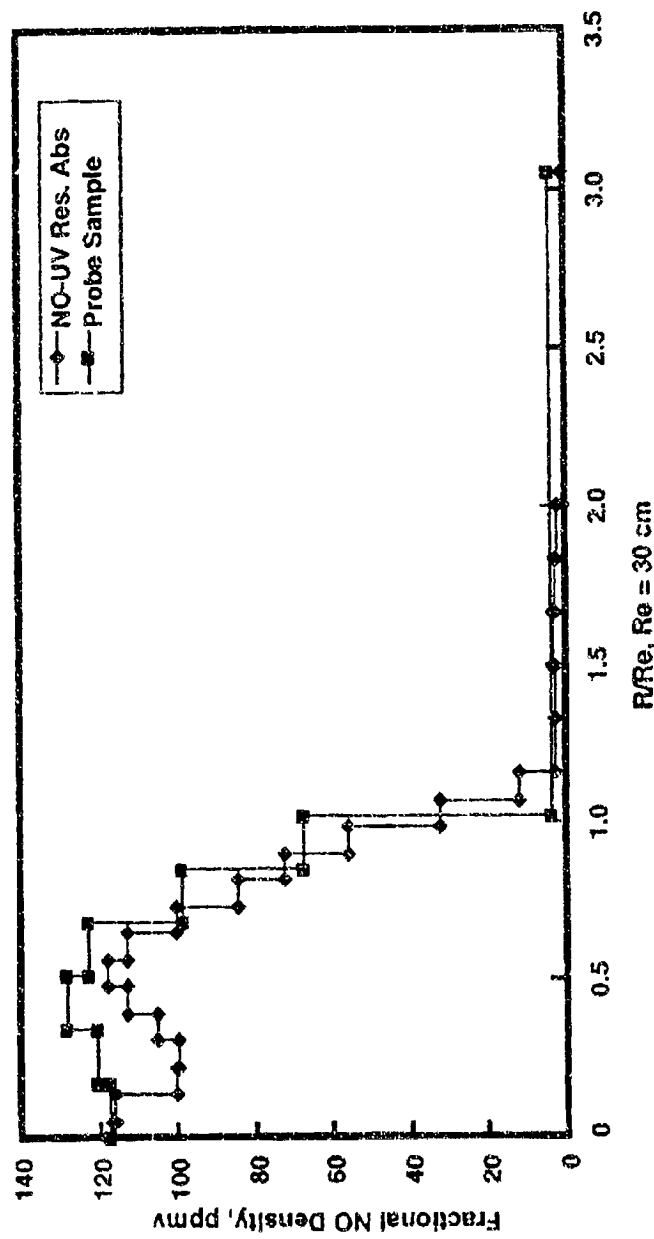
Figure C-10. Resonance absorption and probe sampling radial profiles of NO density for $T3 = 727$ K and 12.2-km altitude.

APPENDIX D
INFRARED TUNABLE-DIODE LASER SYSTEM

Joda Wormhoudt
Richard Miake-Lye

D-1.0 TDL INSTRUMENT

Tunable lead salt diode lasers have a long history of spectroscopic applications (Ref. D-1), and have recently been applied with considerable success to sensitive detection of atmospheric trace gases (Ref. D-2). Our system had been applied to combustion gas flows twice before, first in a combustor simulator at NASA Lewis Research Center (LeRC) (Ref. D-3) and then in a short engine test at AEDC (Ref. D-4).

Our diodes are housed in a liquid nitrogen dewar, with their nominal operating temperature controlled by a small resistance heater. Coarse frequency tuning is achieved by changing the diode temperature and thereby its refractive index and cavity mode frequencies. Fine tuning is done by scanning the injection current, which also has the effect of slightly changing the diode temperature. This current scanning can be done rapidly, allowing the averaging of many spectra whose spectral features are unperturbed by low-frequency fluctuations in the transmission. In the work reported here, the scanning rate and number of spectral points acquired was such that the scan of each diode took 0.5 msec.

In many applications, simultaneous measurement of concentrations of two molecules provides much greater understanding than measurement of either one, or even sequential measurements of both. Diode lasers emit light in a restricted range of frequencies, so that different laser diodes are usually required to detect each molecule of interest. Our typical cryogenic dewar configuration houses four laser diodes behind an infrared (IR) transmitting window, with translation of the dewar serving to select which diode emits into the collecting optics and so through the entire optical train, until laser light is focused onto a detector located in the same dewar. We therefore drew the conclusion that the usefulness of the TDL instrument would be greatly increased if data could be acquired using two diodes at the same time, and set to work reconfiguring the optical layout of the laser table into the arrangement shown in Fig. D-1.

Our focus on *in-situ* measurements in aircraft engine exhausts motivated two other choices in this design. First, we could gain space on the optical table by eliminating the long path absorption cell and therefore the extractive sampling capability used in the NASA LeRC field test. Second, our measurement time scales were such that it was adequate to use a single detector, with discrimination between the two lasers achieved by alternating laser-on (frequency scanning) and laser-off periods.

Therefore, the optical layout drawn in Fig. D-1 is capable of collecting light from two laser diodes (one in each of two banks of four on opposite sides of the dewar), sending two coincident, collimated beams to a retroreflector, then collecting the return beams and focusing them onto the same detector element.

We begin a discussion of the details of the optical layout by tracing the paths of the main or diagnostic beams. Infrared light from the laser diodes is collected by reflective microscope objectives (15x) and focused onto 200-μm pinholes, which define input apertures. The pinholes are used only during alignment, so they are mounted on removable kinematically indexed bases. The microscope objectives are mounted on X-Y-Z translators to allow accurate focusing into the fixed apertures. Past the input aperture, curved mirrors create approximately collimated beams. The two laser beams are then combined at the main beamsplitter, and the co-aligned beams pass to a pair of flat mirrors and onto a large gimbal-mounted steering mirror which directs the beam off the table and into the engine test cell. The return beam is collected by the large steering mirror and a curved mirror of similar diameter, passed through several more flat mirrors and finally focused onto the main beam detector.

The remaining combined beam associated with the main beamsplitter goes into the reference optical path, where it may be sent through a gas calibration cell and/or passed through a grating monochromator, then focused onto the reference detector. The calibration cell contains a sufficient pressure of the gases of interest (in this case, NO, NO_2, and N_2O) that their strong absorption features fully absorb the laser light. This makes it easy to recognize that the laser is operating in the right wavelength region, and to check for the presence of other laser modes. These strong absorption features can also be used to set the frequency scale of the laser scan. The monochromator is used to provide a coarse measurement of the laser frequency during setup of the instrument, and to determine whether the diode is emitting at different wavelengths (different modes). Since no monochromator is available in the main beam path, diode operating conditions must be chosen that allow single mode operation.

There is a parallel visible optical system for alignment and setup. A red HeNe "trace" laser beam passes through the dichroic beamsplitter downstream of each microscope objective, and is coaligned with each infrared beam. Coalignment is guaranteed by focusing the beam through the input aperture. The trace beam is an indispensable aid for alignment of the optical system. In addition, the trace beam is used for accurate calibration of the monochromator, via higher order diffraction. The fourth port of the dichroic beamsplitter can be used to observe the laser diode during alignment. An eyepiece mounted at the position conjugate to the pinhole forms an effective 150x microscope.

We set up the instrument with an NO diode on one side of the dewar and NO_2 and CO_2 diodes on the other, with the CO_2 diode operating at the beginning of the test. At several points during the test, the collection optics were moved to pick up light from the NO_2 laser, then moved back to the CO_2 laser. The change from one diode to another followed by optimization of transmitted laser intensity could be successfully completed in a few minutes.

The temperature and current of each laser are controlled by a Laser Photonics controller. All inputs to this controller were made via a program running on the data acquisition and analysis computer. In a typical experiment, the laser temperature is held constant while the current through the laser is modulated with a computer-generated sawtooth to sweep the output frequency across the IR transition. The sawtooth was generated in 150 discrete steps for each laser by a digital-to-analog converter board. The total of 300 display points in the two laser spectra is swept at a rate of 1 kHz. During approximately 10 percent of the duty cycle, the laser current is dropped below the lasing threshold to provide a precise measurement of zero light intensity.

The data acquisition techniques, involving a Scientific Solutions Lab Master analog-to-digital converter board and direct memory access transfer to the extended memory of the data-acquisition computer, remain as described previously (Ref. D-3). Although the TDL instrument could in principle produce real-time records of gas concentrations, this would require input of probe rake data (or assumptions about properties along the line of sight (LOS) from other sources). Our data acquisition therefore consisted of the recording of a large number of spectral files covering segments of both the NO and CO_2 (or NO_2) regions. These were recorded as averages over periods of 10 to 60 sec.

D-2.0 DIAGNOSTIC IMPLEMENTATION IN THE ENGINE TEST CELL

Figure D-2 shows two views of how the TDL diagnostic was applied to the engine exhaust in the AEDC altitude test cell. The TDL instrument was placed on a table directly below the optical access port into the test cell. The TDL beams were directed into the test cell by a 45-deg mirror mounted on the outside of the access port flange. A 0.95-cm thick CaF_2 window with a 1-deg wedge (to suppress interference fringes) was mounted on the access port using a retaining plate with a 10-cm-diam clear area. Because the access port was offset from the engine exit plane location, the beam next passed through a 150-cm long aluminum tube containing two flat mirrors. This periscope was purged with gaseous nitrogen to protect against both recirculating exhaust, and oil and water mists from the engine, and the exhaust treatment device called a diffuser. The TDL beams were returned, horizontally displaced by about 2 cm by a retroreflector. The HeNe trace beam could be followed through the entire optical path, which allowed precise aiming of each steering mirror.

The potential dangers to our mirrors of the diffuser water spray and engine oil fumes mentioned above concerned us enough that an arrangement was made to place baffles in front of the periscope and retroreflector when the TDL diagnostic was not operating. This was done by attaching aluminum baffle plates on the AEDC ultraviolet cross-flow absorption device. In addition, purged tubes extended from the periscope (50 cm in length) and from the retroreflector (45 cm) toward the exhaust flow, leaving an unpurged length along the LOS of about 238 cm.

D-3.0 EXAMPLES OF OBSERVED SPECTRA

Figure D-3 presents two examples of raw diode intensity spectra for the TDL diagnostic beam, one taken while the laser beam was passing through the exhaust and the other while the beam path was blocked by the UV instrument. The vertical axis is simply intensity at the detector expressed in mV, with the lowest point on the beam-blocked spectrum being shifted to zero, and the exhaust spectrum also shifted until the laser-off points at the right-hand side of the figure coincide with the beam-blocked values. The horizontal axis is in display units or data acquisition points over the laser scan. The NO absorption line used in almost all measurements is clearly seen, with the wing of the first of two neighboring water absorption lines contributing to the decrease in transmission at the right-hand side of the figure. These water lines have fairly high lower-state energies and hence are substantially stronger in the hot exhaust plume than they are at ambient temperature, even over the much longer optical path outside the test cell.

The NO_2 scan presents smaller absorption features than those seen in the NO scan, but it will be seen below that the absorption lines indicated are due to known lines of NO_2 and H_2O. A mode change is seen at about 20 display units. Observation of the reference leg intensity as the monochromator grating is scanned confirms that the diode laser intensity below this point was in an entirely different wavelength range than in the rest of the scan. The diode is emitting in only one mode throughout the entire scan, but there is an abrupt change from one mode to another. (Clearly, in insidious cases there could be no telltale discontinuity, and only the monochromator diagnostic would make the situation clear.) In Fig. D-4, we present a corresponding raw intensity spectrum at the reference leg detector, while the reference laser beams are passing through a short cell containing substantial amounts of NO and NO_2. In the NO scan, two strong NO line features are seen. The line at 222 display units is the diagnostic NO line indicated by the arrow in Fig. D-3. The second line is exactly coincident with the lower frequency of the two water lines in Fig. D-3. Therefore, it is of no interest for the measurement of NO in exhausts, but it would have to be taken into account if one wanted to use the water lines for high accuracy measurement of the water mixing fraction in the plume.

Turning to the NO_2 laser reference scan, we see the high density of NO_2 lines which adds to the difficulty of sensitive detection of this molecule. Furthermore, it will be seen that a similar den-

sity of water lines also exists in this region. The line we will use as the diagnostic line is the strong line near the center of the NO_2 scan, at 77 display units.

D-4.0 DATA ANALYSIS PROCEDURES AND ERROR LIMIT ESTIMATES

D-4.1 DATA ANALYSIS

Several steps are required to convert the raw diode intensity scans into transmission spectra and deduce molecular mixing fractions, mass fluxes, and emission indices. In the first step, absorbances of the diagnostic lines are quantified by least squares fits, using the TDL data acquisition program in data analysis mode. This is the routine that allows real-time fitting and concentration measurement, here applied to stored spectra. Lines are fit to Voigt line profiles using a nonlinear least squares routine based on the Levenberg-Marquardt approach (Ref. D-5). The baseline, varying from unit transmission due to diode laser power fluctuations and residual etalon fringes, is represented as a slowly varying polynomial of low order. Lines or sets of lines in six spectral regions were fit: the NO line pointed out in Fig. D-3 (near 1897 cm⁻¹), the pair of water lines to its right, an NO line near 1909 cm⁻¹ (for two engine conditions), a pair of NO_2 lines, one of which has an overlapped water line (all near 1597 cm⁻¹, observed during six engine conditions), and a CO_2 line near 2225.5 cm⁻¹ (observed during one engine condition).

Figures D-5 and D-6 show two of the spectral regions that were analyzed. In each figure the solid line is the observed trace as converted to a transmission scale by the TDL data analysis program, through its fit of a polynomial baseline (this calculation also uses as an input the relative position of the laser-blocked intensity trace shown as the dotted line in Fig. D-3). The ratios of Doppler and pressure-broadened line widths in the fitting models were constrained, using HITRAN parameters (Ref. D-6) and a single representative temperature and pressure that changed with engine condition. In the fitting of the 1897-cm⁻¹ H_2O doublet, there is an additional constraint of a fixed intensity ratio and an additional fitting parameter, the spacing between the two lines. In the NO_2 region, all lines contributing to the two features in Fig. D-6 are included, with NO_2 and H_2O concentrations varied separately to achieve the best fit.

The second step is to convert the optical depths (absorption line peak intensities) determined by the least squares fits into a set of column densities over the nonuniform optical path through the exhaust plume. Our approach uses predicted spectra generated from the HITRAN database using a program written at Aerodyne Research, Inc. (ARI), which takes sets of temperatures, pressures, species mole fractions, and path lengths for each segment of the nonuniform LOS through the exhaust plume and calculates a total absorption spectrum. The result of this model calculation is a line peak absorbance to be matched to the observed value from the least squares fitting discussed above. The sets of temperatures, pressures, and path lengths used in our analyses were those used

107

in the analysis of the AEDC NO resonance lamp data. This model assumed the plume to be made up of 20 concentric annular cylinders with constant properties equal to linear interpolations of the probe values. The final set of parameters we require, the relative mixing fractions in the 20 cylinders, can be obtained from several sources, and we used a number of sets to evaluate our sensitivity to the assumption of a particular model mixing profile. Examples of two such mixing models are shown in Figs. D-7 and D-8 for two engine conditions.

One mixing fraction profile is derived by taking ratios of differences of probe total temperature measurements and an ambient total temperature (converted from static temperatures outside the exhaust flow, or taken from probe total temperature values outside the exhaust) to that difference at the plume center. This relative mixing fraction is near unity for the innermost cylinder, and decreases for the outer cylinders. The other mixing fraction shown in the figures is derived from the inversion of the AEDC NO resonance lamp data sets, and consists of NO mole fractions normalized to unity at the centerline. The absolute value of the centerline mixing fraction is then determined as the multiplicative factor that brings the model calculation of line peak transmission into agreement with the value determined from the least squares fit of the observed line. The resulting model spectra for the two models described above are averaged to give the dotted lines in Figs. D-5 and D-6. Figure D-6 also contains model spectra for the individual contributions of NO_2 and H_2O. In order to plot these model calculations on the same scale as the data and TDL analysis program fits, the line positions and frequency scales were set by the reference line positions shown in Fig. D-4.

D-4.2 DERIVATION OF CONCENTRATION AND MASS FLUX VALUES

The sampling probe not only produced spatially resolved values of temperature and pressure but also velocity. These values can be used to convert our single LOS measurement to a total species flux in the exhaust. Our procedure was to use the same 20-cylinder model, multiplying cylinder areas, species number densities (formed from mixing fractions and total densities computed from static temperatures and pressures), and velocities with conversions involving the molar volume and the molecular weight to yield a mass flux in g/s. In the aircraft emissions community, the results of such mass flux measurements are typically expressed as emission indices (EI), the ratios of g/s of the exhaust species to fuel flow rate in kg/s. Our conversion from mass flux to EI was made using the tabulated fuel flow rates.

As a check on this procedure, we performed the same mass flux calculations except with the mixing fraction omitted. This total mass flux should match the tabulated input mass flux, a quantity measured at a level equivalent to the fuel flow rate mentioned above. It turns out that in most (but not all) cases, the total mass flux computed from probe rake measurements is substantially less than the inlet mass flux. Discrepancies are not surprising, given the coarse grid on which probe rake

sampling measurements were made. However, it is not possible to be certain whether a correction factor that converts probe rake integrations into inlet total mass fluxes should be applied to exhaust species emission indices as well. If the integration of probe rake values has underestimated contributions to the total mass flux from regions near the outer boundary of the exhaust flow, the corrections to an NO or CO_2 emission index will be much smaller than the correction to total mass flux, because the mixing fraction of exhaust species is going to zero in this region. On the other hand, corrections stemming from inaccuracies in flow parameters near the centerline will apply equally to the total mass flux and to exhaust species emission indices. Because of this uncertainty, we did not apply individual corrections factors, but used their average to estimate the magnitude of errors involved in using probe rake data to convert concentration profiles to emission indices.

The other contributions to an error estimate which we considered were the statistical errors in sets of multiple optical depth measurements, and an estimate of the systematic errors involved in conversion of optical depths to concentration profiles. The former actually involve two classes of nominally comparable measurements. The first class involves multiple measurements while the engine remained at a given operating condition. Analyzed in the same way, multiple spectra typically gave remarkable repeatable optical depths, with standard deviations of a few percent except for low signal idle conditions. The second class of multiple measurements involves variation of the order of the baseline polynomial used as part of the TDL data analysis program least squares fitting to determine line peak optical depths. Polynomials of order three through five were used. Again, differences were typically small except in low signal cases. In some of those cases, there may be interfering lines or etalon fringes, and additional analysis of individual spectra may reduce these error limits.

Our estimate of the errors involved in converting optical depths to concentration profiles (that is, assigning a peak concentration scaling factor to an assumed mixing profile within a model calculation of the absorption spectrum along a nonuniform path) focused on the differences resulting from different mixing profiles. (Example calculations performed by varying the assumed temperature profiles, for example, indicated lower sensitivities to the other model parameters.) The model calculation discussed above, of predicted optical depth for a given set of model parameters including mixing fraction and of conversion factor (independent of spectral region) between centerline mixing fraction and emission index, can be combined into a single conversion factor, which multiplies peak optical depth for a given spectral line to convert it to emission indices. In Table D-1, these conversion factors are listed for the 24 steady engine conditions and the NO absorption line near 1897 cm $^{-1}$, for the two mixing model examples shown in Figs. D-7 and D-8.

These two models, while broadly similar, differ in at least two significant ways. First, while the mixing profiles based on ratios of total temperature differences almost always have their peak values on the centerline, the UV NO profiles typically show a peak in mixing fraction at an

intermediate radius. Although uncertainties in the inversion of UV lamp data increase for the lines of sight near the centerline, we believe that the indication of a dip in the middle of the concentration profile is qualitatively correct, since for the three cases where spatially resolved sampling probe measurements were made, such a central dip is clearly and consistently observed. The significance of such differences in profiles is that an outer cylinder makes the same contribution to the observed line-of-sight optical depth as one near the centerline with the same column density (product of number density and path length), but its contribution to the mass flux and hence the emission index is larger by the ratio of the radii.

The second difference, of significance in the sea-level cases such as the one shown in Fig. D-7, is that our particular implementation of a model based on ratio temperature differences accounts for very little recirculating exhaust gas outside the jet radius, while the UV NO based profile in Fig. D-7 indicates a significant concentration. However, during this case and a few others, sampling measurements were made at three points outside the jet radius (the outermost at just inside 3 radii). These measurements indicate that the true exhaust mixing fraction in this region along the centerline LOS lies between the values indicated in Fig. D-7. It must be kept in mind that the UV NO lines of sight that determine the values shown in the dotted curve in Fig. D-7 are above the plume, not on either side, and it may be that more recirculating gas is found near the top of the test cell. Also, a third full set of models was used to analyze the data, with the mixing fraction determined by ratios of static temperature differences. This is clearly not defensible on first principles, and indeed gives a mixing fraction within the exhaust flow that is much too peaked at the centerline compared with any other method of estimation. However, this model has the advantage that the recirculation sampling measurements are all fairly well reproduced (most to within a factor of two), so it can function as a correlation of expected concentrations in the recirculation region for all cases. Inclusion of these conversion factors in our evaluation did not increase the estimate of error limits due to systematic errors in the assumed mixing profiles.

Numerical values resulting from the above three estimates of contributions to an overall error limit are listed in Table D-1. In that table, NO emission indices (from 1897-cm^{-1} line observations) and the resulting estimate of a total error limit, in EI units, are given in the second and third columns. The fourth column, the fractional standard deviation in multiple measurements of comparable optical depths, is seen to vary from less than 1 percent (in one idle case) to more than 30 percent. The next two columns are the absolute values of the calibration factors which convert peak optical depth to EI(NO) within the two models discussed above. The deviations from unity of the ratios of these two columns are averaged to give an estimate of this uncertainty level as a fraction of EI. This average is then applied uniformly to all cases. The same procedure is applied to the last column, which is the ratio of total mass flux measured at the engine inlet to mass flux deduced from an integration of exhaust probe rake values. The fact that this converts a correction

factor, which in almost all cases increases the reported emission index into an error estimate which implies positive and negative corrections are equally likely, is not a problem, in our opinion. There are other potential errors in our model-based analysis which could result in systematic downward corrections, so our choice of expanding the error bars rather than employing the correction factors seems reasonable. When the error estimates derived from averages of differences from unity of mixing model conversion factor ratios and total mass flux ratios are added in quadrature, the total fractional error limit assigned to these systematic errors is 19 percent. This is added (in quadrature) to the statistical error estimates in optical depth listed in the fourth column to give a total fractional error, which is then multiplied times the EI(NO) to give error limits in EI units, tabulated in the third column, and used in the comparison plots in the main body of this report.

Our analyses of the smaller number of data points obtained in other spectral regions indicated that similar 20- to 30-percent error limits in emission indices should apply. One final comment can be made based on the two columns of EI conversion factors in Table D-1. If the idle condition points are excluded, it is interesting to note that all other conversion factors vary by not much more than a factor of two, even though conditions vary over a wide range of power settings and simulated altitudes from sea level to 15.2 km. In other words, although much of our discussion has focused on how the current TDL technique is dependent on characterization of the optical path for the derivation of accurate values, this shows that factor-of-two emission indices could be obtained directly from optical depths with only minimal corollary information about the exhaust plume, such as previous observations or a CFD calculation. In the present test where the focus was on comparison to state-of-the-art NO measurement techniques, such approximate determinations are of no interest. However, it is possible to imagine situations in which the TDL technique could be extended to new species, for which even order-of-magnitude measurements are not now available, and used in a screening mode to identify which species, engines, and operating conditions require more careful and quantitative studies. In those situations, factor-of-two values without the need for probe rake instrumentation might be very useful. Of course, we hope to develop TDL techniques which use line pairs (such as an NO and a CO_2 line) to make self-calibrating measurements, as is currently done by deriving sampling EI(NO) measurements from the ratio of NO and CO_2 concentrations. However, some additional development work will be required before we can be sure this can be done, even for the species we already detect.

The full set of observed emission indices obtained to date is given in Table D-2. The generally good agreement between the EI(NO) values and those from the two other measurement techniques has been discussed in the main body of the report, where comparison plots showed identical trends in almost all cases and agreement within the estimated error limits, again in almost all cases. A few anomalous points can be mentioned: the 9.1-km idle NO observation is clearly too low, whereas at 15.2 km, differences at one or more power settings lead to the appearance of a different trend than observed by the other techniques. It may be that additional analysis of the

spectra in these cases will resolve some of these anomalies. For two engine conditions, a second line at 1909 cm⁻¹ was used to measure NO in addition to the line at 1897 cm⁻¹. The NO concentrations determined from the two lines were in good agreement, as expected. The NO_2 and H_2O values obtained in the 1597-cm⁻¹ region are clearly sensitive to assumptions about the baseline position (in this spectral region, lines are sufficiently overlapped that the baseline is not directly observed). Still, with the exception of the 9.2-km idle point, the water emission indices agree with the theoretical value of 1233 to well within the expected uncertainty limits. The water lines in the 1897-cm⁻¹ region are inadequate for accurate measurements in several respects, so we evaluated one observation, found (not surprisingly) a substantial disagreement with the theoretical value, and do not plan further investigation of this region. The CO_2 observation is the only one in which all lines in the scan are in the HITRAN92 tabulation. Spectra were obtained for all other engine conditions, but have not yet been analyzed. The HITRAN96 data compilation, soon to be released, will contain a separate file of high-temperature CO_2 lines which may allow a full set of CO_2 emission indices to be derived from our spectra, but until that analysis is carried out, we cannot be certain how accurate that database will prove to be, and whether laboratory characterization of unknown lines will also be required. The CO_2 emission index listed in Table D-2 differs by less than 10 percent from the theoretical value of 3260. The theoretical values were determined from the fuel analysis data, assuming that all the carbon in the fuel was converted to CO_2 during combustion.

REFERENCES

D-1. Eng, R. S. and Ku, R. T. "High Resolution Linear Laser Absorption Spectroscopy." *Spec. Lett,.* 15, 1982, pp. 803–929.

D-2. Kolb, C. E., Wormhoudt, J. C., and Zahniser, M. S. "Recent Advances in Spectroscopic Instrumentation for Measuring Stable Gases in the Natural Environment." *Biogenic Trace Gases: Measuring Emissions from Soil and Water*, P. A. Matson and R. C. Harriss, Editors, pp. 259–290, Blackwell Science Ltd, Oxford, UK, 1995.

D-3. Wormhoudt, J., Zahniser, M. S., Nelson, D. D., McManus, J. B., Miake-Lye, R. C., and Kolb, C. E. "Infrared Tunable Diode Laser Diagnostics for Aircraft Exhaust Emissions Characterization." in *Laser Applications in Combustion and Combustion Diagnostics II*, Randy J. Locke, Editor, Proc. SPIE 2122, 1994, pp. 49–60.

D-4. Wormhoudt J., Zahniser, M. S., Nelson, D. D., McManus, J. B., Miake-Lye, R. C., and Kolb, C. E. "Infrared Tunable Diode Laser Measurements of Nitrogen Oxide Species in An Aircraft Engine Exhaust." *Optical Techniques in Fluid, Thermal and Combustion Flows*, Proc. SPIE 2546, 1995, pp. 552–561.

D-5. Press, W. H., Flannery, B. P., Teukolsky, S. A., and Vetterling, W. T. *Numerical Recipes.* Cambridge Univ. Press, Cambridge, 523–528, 1986.

D-6. Rothman, L.S., Gamache, R. R., Tipping, R. H., Rinsland, C. P., Smith, M.A.H., Benner, D. C., Malathy, Devi, Flaud, J.-M., Camy-Peyret, C., Perrin, A., Goldman, A., Massie, S. T., Brown, L. R., and Toth, R. A. "The HITRAN Molecular Database: Editions of 1991 and 1992." *Journal of Quantitative Spectroscopy Radiative Transfer,* 48, 1992, pp. 469–507.
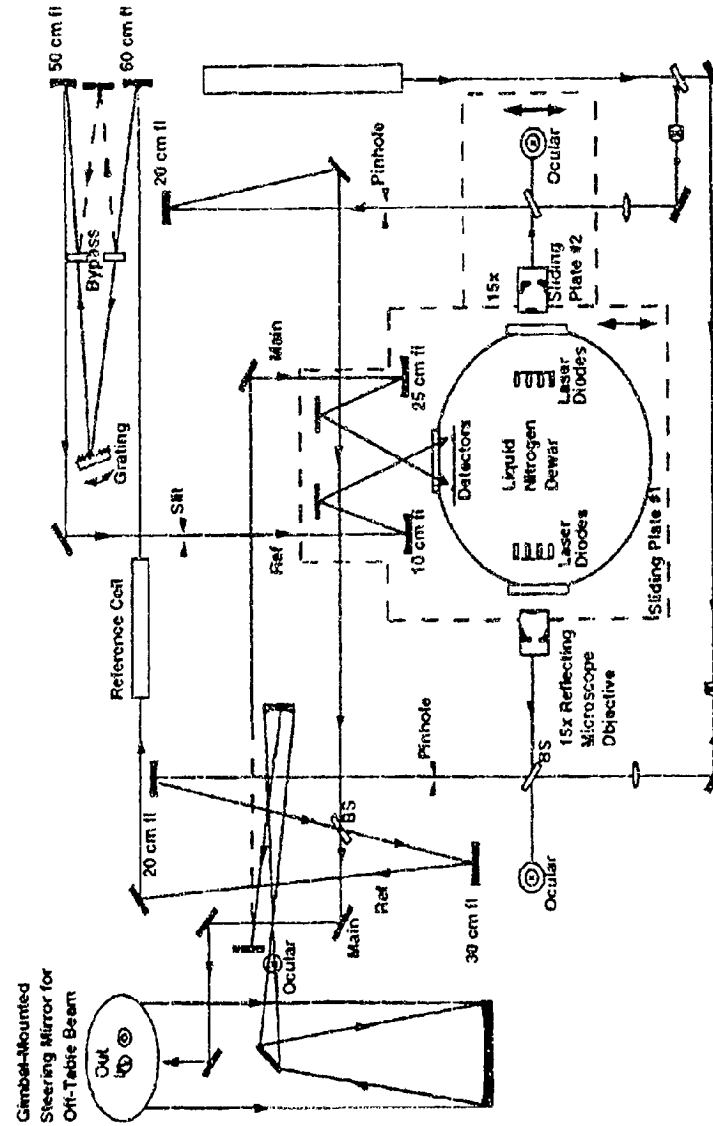
Figure D-1. Optical layout of laser table.

114
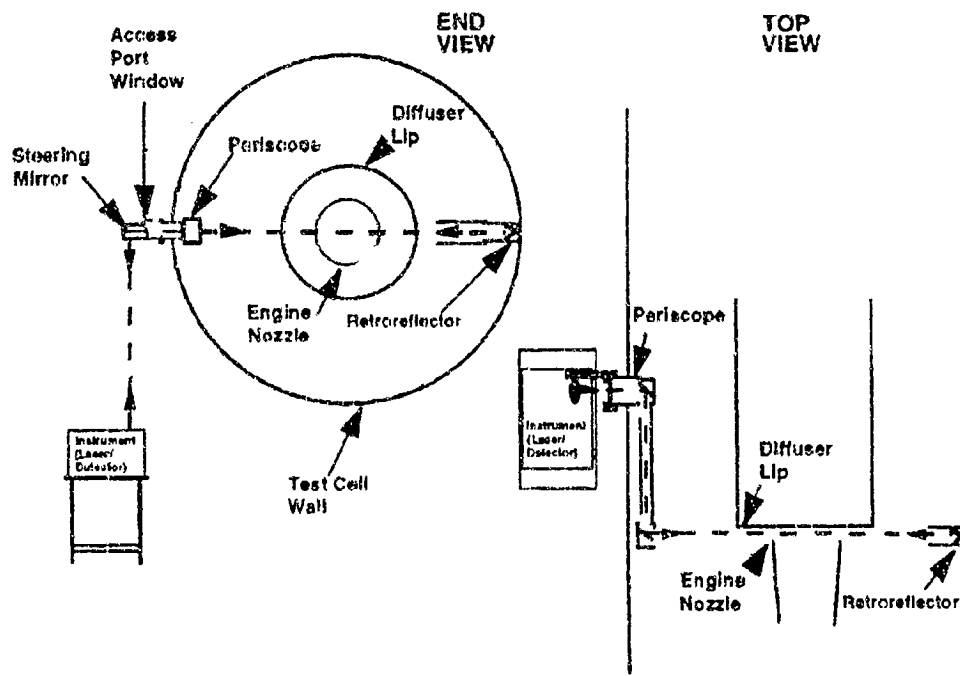
Figure D-2. Schematic of TDL diagnostic beam path through engine test cell.
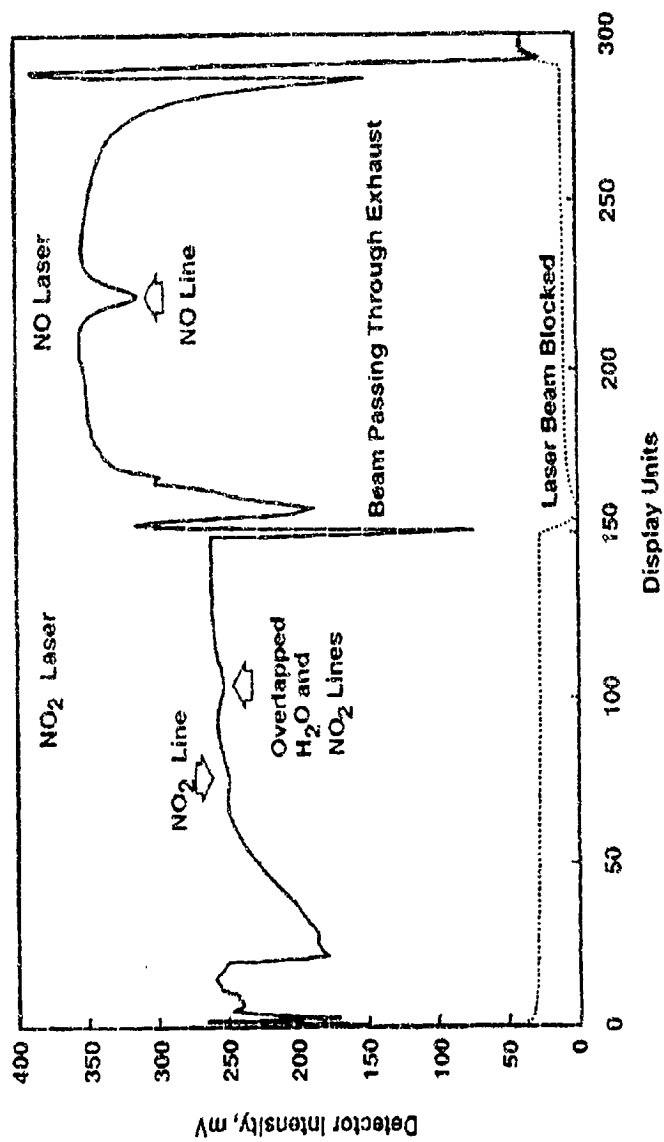
Figure D-3. Example intensity scans for NO_2 and NO lasers.

116
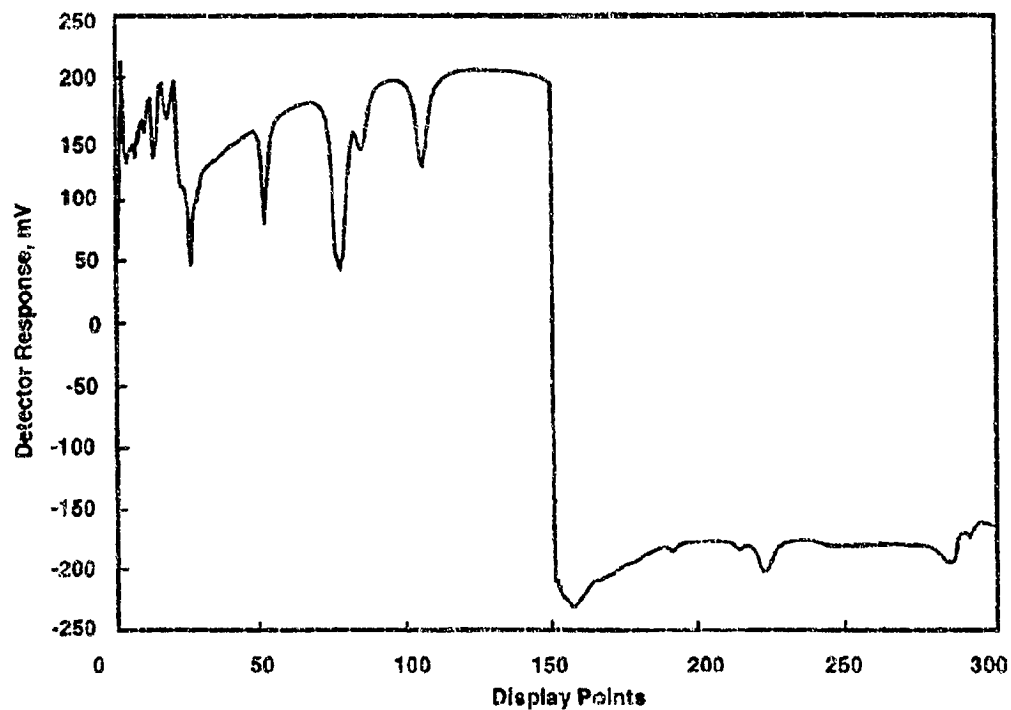
Figure D-4. Reference cell intensity scan (corresponding to Fig. D-3)
showing reference lines of target gases.

117
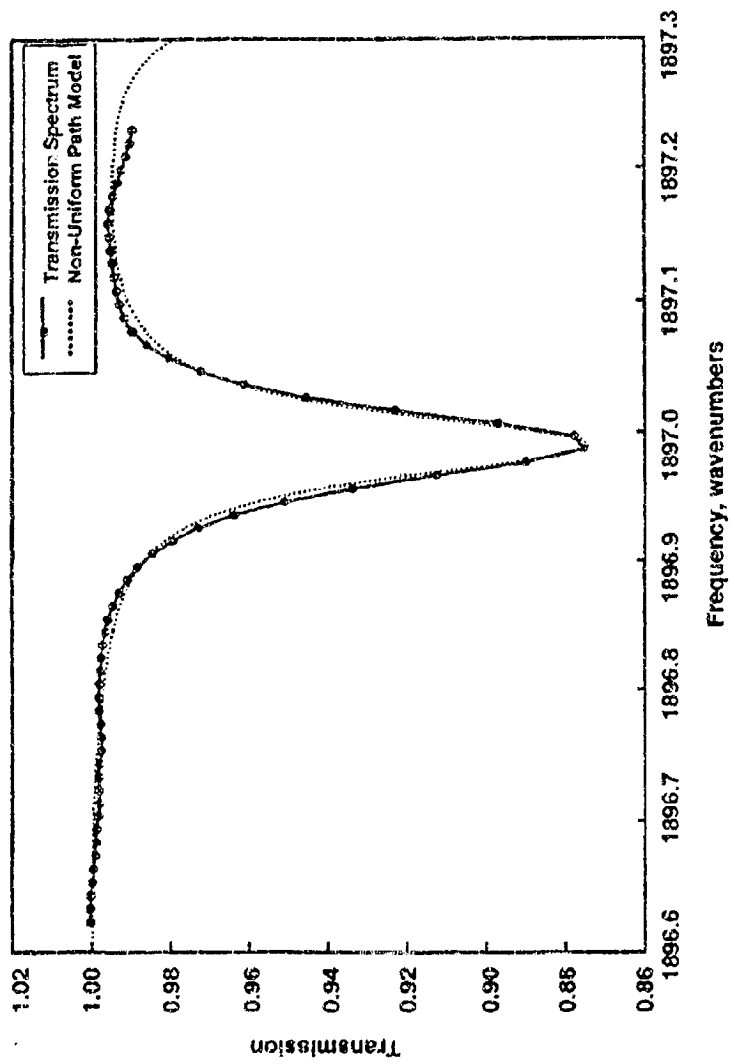
Figure D-5. NO region observed transmission spectrum and non-uniform path model.
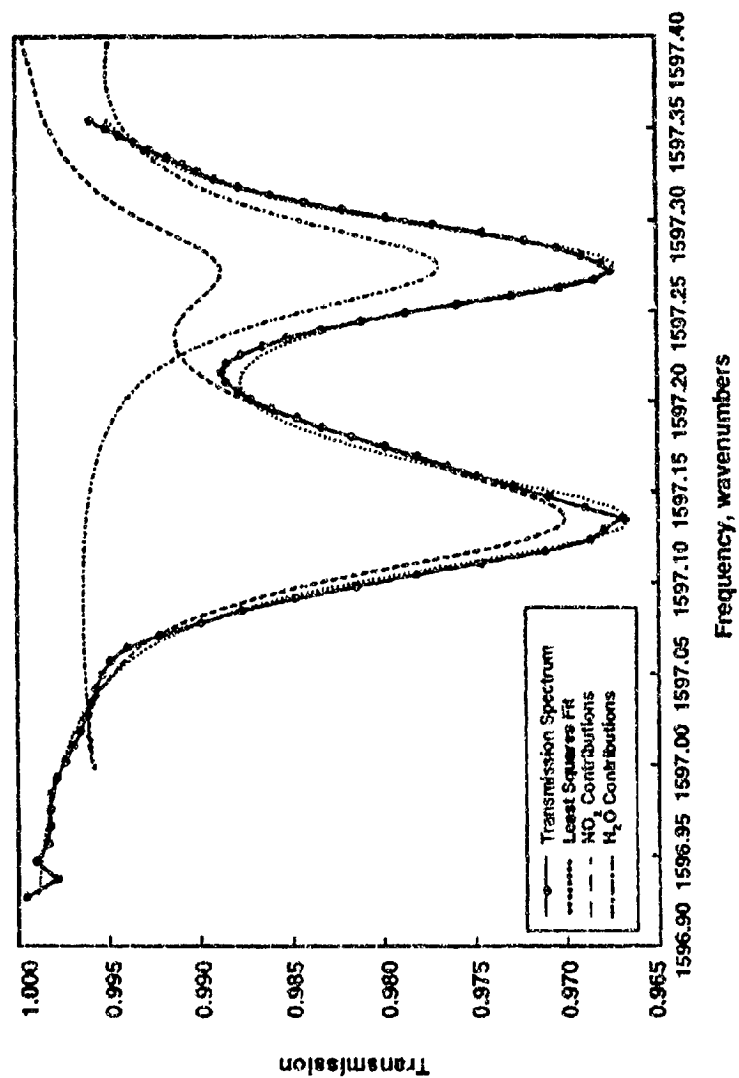
Figure D-6. NO$_2$ region observed transmission spectrum, least squares fit using segment model, and individual contributions from NO$_2$ and H$_2$O from non-uniform path model.

119
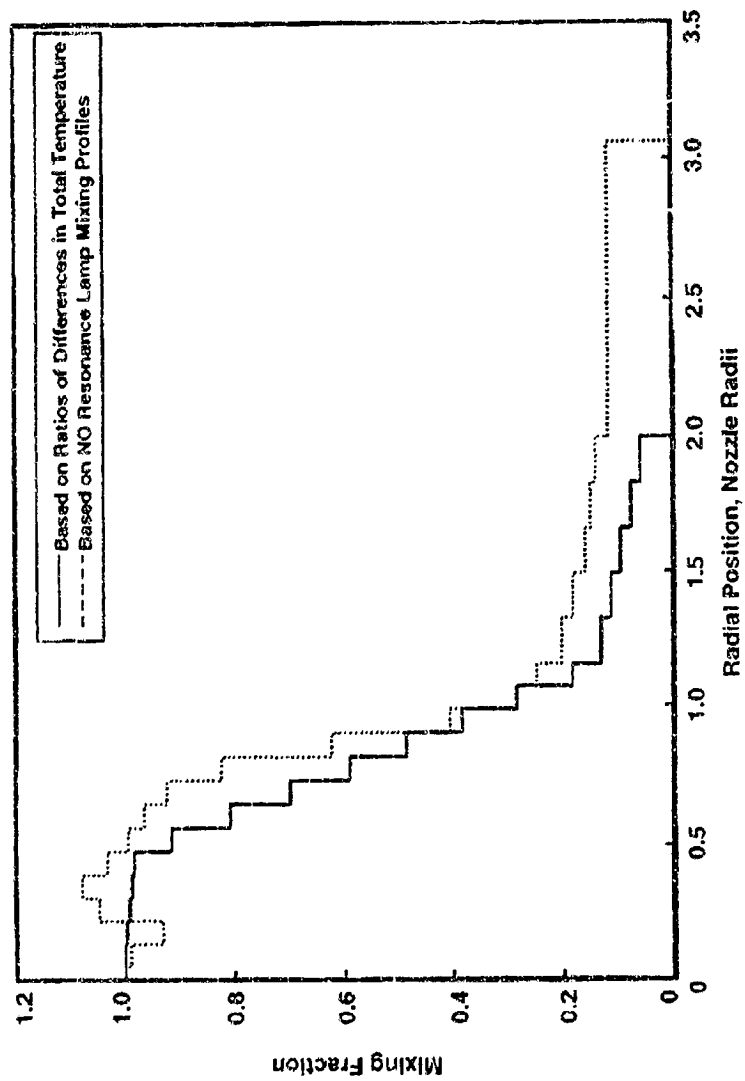
Figure D-7. Relative mixing fractions for case SLS/733 used in two analysis models.
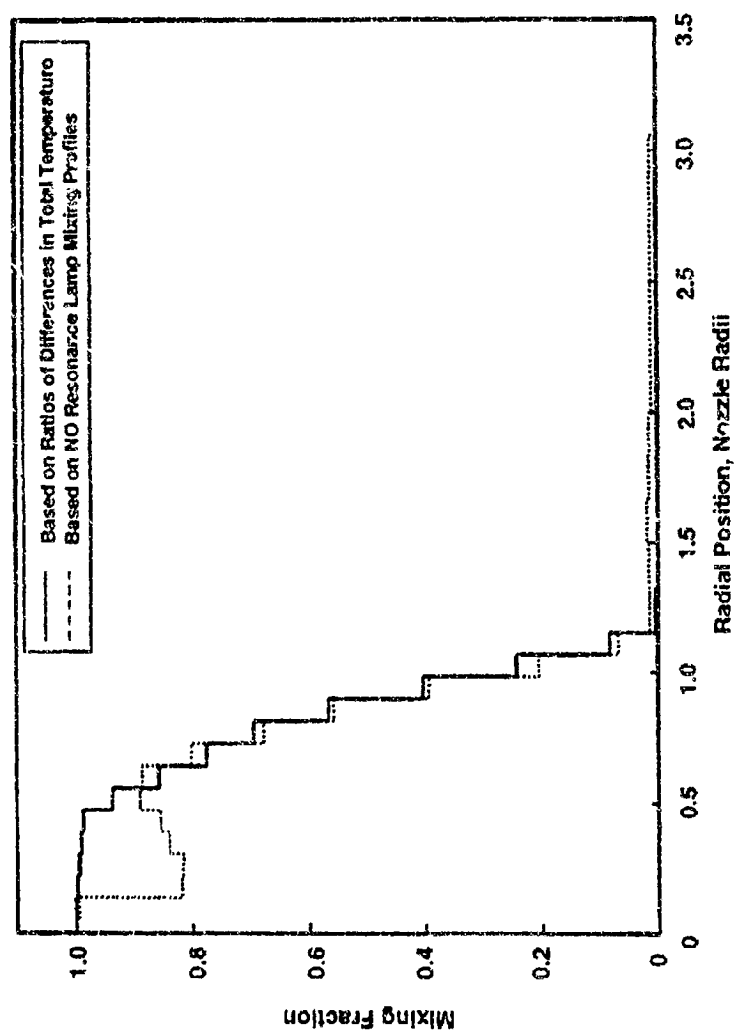
Figure D-8. Relative mixing fractions for case 9.1 km/733 used in two analysis models.

Table D-1. Emission Index Values for NO Determined from IR TDL Absorption in the 1897-cm^{-1} Region, with Total Error Limits and Quantities Used to Estimate Them

Condition T3/Altitude	EI(NO)	Error Limit in EI	Standard Deviation in Optical Depth	T-Ratio EI Conversion Factor	UV EI(NO) Conversion Factor	Total Mass Flux Factor: Inlet/Model
858/7.6 km	27.38	5.27	0.0082	163.70	156.35	1.08
764/7.6 km	13.28	2.56	0.0155	169.32	164.71	1.23
733/7.6 km	11.15	2.16	0.0219	178.29	175.71	1.21
668/7.6 km	8.91	1.73	0.0304	226.21	209.43	1.14
512/9.1 km	2.06	0.47	0.1240	364.26	249.58	0.99
733/9.1 km	12.55	2.46	0.0370	168.77	167.79	1.08
765/9.1 km	14.26	2.75	0.0153	161.94	162.95	1.08
808/9.1 km	18.53	3.57	0.0118	155.77	156.75	1.10
671/9.1 km	9.02	1.74	0.0130	186.28	187.15	1.22
727/12.2 km	10.20	2.03	0.0505	187.87	186.75	1.08
766/12.2 km	11.85	2.28	0.0075	180.36	182.43	1.09
665/12.2 km	7.20	1.39	0.0099	207.91	203.47	1.17
557/12.2 km	3.85	0.75	0.0312	306.25	255.78	1.08
635/15.2 km	6.01	1.22	0.0647	257.32	175.07	1.15
671/15.2 km	8.73	1.70	0.0303	267.98	217.14	1.17
732/15.2 km	9.88	1.90	0.0061	238.22	214.97	1.11
764/15.2 km	10.29	1.98	0.0155	238.31	234.68	1.07
733/SLS	17.19	3.33	0.0219	145.04	110.62	1.17
669/SLS	13.31	2.57	0.0193	169.28	130.77	1.16
651/SLS	12.59	2.43	0.0205	182.59	140.46	1.13
526/SLS	3.59	0.90	0.1629	392.55	277.70	0.99
517/SLS	3.43	1.26	0.3147	407.16	307.40	0.97
762/SLS	18.94	3.67	0.0258	139.86	118.34	1.19
861/SLS	41.78	8.20	0.0392	150.29	119.17	1.11

Table D-2. Emission Index Values Obtained from IR TDL Absorption Spectra
(Spectral Regions of Lines Used in Wavenumbers,
Given in Parentheses)

Condition T3/Altitude	EI(NO) (1897)	EI(NO) (1909)	EI(NO_2) (1597)	EI(CO_2) (2225)	EI(H_2O) (1897)	EI(H_2O) (1597)
858/7.6 km	27.38					
764/7.6 km	13.28					
733/7.6 km	11.15					
668/7.6 km	8.91					
512/9.1 km	2.06		1.45			2113
733/9.1 km	12.55	13.18	1.32			1400
765/9.1 km	14.26					
808/9.1 km	18.53					
671/9.1 km	9.02					
727/12.2 km	10.20		1.11			1492
766/12.2 km	11.85					
665/12.2 km	7.20					
557/12.2 km	3.85					
635/15.2 km	6.01					
671/15.2 km	8.73					
732/15.2 km	9.88		1.45			1341
764/15.2 km	10.29		1.61			1128
733/SLS	17.19	19.16	1.40	3260	1760	1523
669/SLS	13.31					
651/SLS	12.59					
526/SLS	3.59					
517/SLS	3.43					
762/SLS	18.94					
861/SLS	41.78					

APPENDIX E
AEROSOL SAMPLING MEASUREMENTS (INCLUDING CO₂ DIAGNOSTIC TEST)

D. E. Hagen, P. D. Whitefield, A. R. Hopkins, J. D. Paladino, M. B. Trueblood
Cloud and Aerosol Sciences Laboratory
University of Missouri-Rolla
Rolla, MO 65409-0430 USA

E-1.0 INTRODUCTION

There is a real need to improve the industry standard for aerosol characterization in jet engine emissions. The current "smoke number" technique, although useful, does not provide the essential characteristics: total aerosol and non-volatile aerosol concentration, size distribution, and hydration or growth as measured by soluble mass fraction and critical supersaturation spectrum. These characteristics are needed in order to effectively monitor the environmental impact of engine emissions. They also represent the input parameters required by models designed to describe the production and dispersion of engine aerosol emittants from the combustor, through the exhaust nozzle plane to their eventual equilibration with the ambient atmosphere. In this appendix, we describe the application of a mobile aerosol monitoring facility, the University of Missouri-Rolla Mobile Aerosol Sampling System (UMR MASS), to characterize engine aerosol emissions in partial fulfillment of the altitude chamber test, which is the subject of this report. The multi-configurational MASS has been employed in both ground and airborne field operations. It has been successfully flown on the NCAR Sabreliner research aircraft (Ref. E-1), the DLR (German Aerospace Research Establishment) Falcon research aircraft (Refs. E-2 and E-3), and on the NASA DC8 research platform in project SUCCESS. In ground tests, the MASS has participated in numerous jet engine related ground tests at NASA Lewis, Pratt and Whitney, AEDC and MDAF (Refs. E-4 and E-5), and has been deployed to the Air Force's Phillips Laboratory to resolve aerosol generation problems in a high power chemical laser system (Ref. E-6). In all cases the measurements were made on samples taken from a harsh physical and chemical environment: with both high and low temperature and pressure, and in the presence of highly reactive gases.

E-2.0 EXPERIMENTAL APPROACH

A schematic diagram of the UMR MASS (Mobile Aerosol Sampling System) configured for the AEDC Current Advanced Commercial Engine Simulation Emissions Studies is shown in Fig. E-1. For this test, the MASS was divided into two work stations. The first, located close to the extractive sampling probe selection manifolds, was used in conjunction with the extractive sampling system to acquire total condensation nuclei (CN) concentrations for all aerosols in real-time and to fill and pressurize sample tanks. The exhaust sample was delivered to the MASS from

individual and ganged probe sources. An isobaric cooler for supersaturation pulse simulation, a laser aerosol spectrometer for real-time large diameter aerosol measurements (diameters from 1.0 to 30 μm), and a needle-to-grid electric precipitator for aerosol collection on electron microscope grids were also located at the first work station. The second work station consisted of two EAC's (Electrostatic Aerosol Classifier) configured in series as shown in Fig. E-1. With this system the tank samples taken at the first work station were analyzed for size distribution, and growth and/ or hydration (critical supersaturation) information for aerosols in the submicron range 10 nm to 0.5 μm.

The MASS methodology is described in the following sections.

E-2.1 TOTAL CN CONCENTRATIONS

For total CN the incoming sample stream is routed straight to a CN counter (CNC). Aerosol concentrations are measured continuously with typically a 3-sec counting period. In situations where the sample pressure drops below 0.5 atm, it is found that particle counting efficiency falls off and must be accounted for. The efficiencies for the counters used in this work were measured during a recent study devoted to calibration and operation of CNC's.

E-2.2 SIZE DISTRIBUTION MEASUREMENT

Aerosol size distribution measurements are made using a single EAC (Ref. E-7) where sample aerosol laden air is drawn from the source and ducted to the MASS (see Fig. E-1). In cases where the sample is available only for a short time (i.e., seconds), an intermediate storage tank is used to store the sample for subsequent processing with the MASS. For size distribution and hydration characterization, the air is directed along path (1) and given an electrical charge in the bipolar charger. The aerosol then passes through EAC1 and a selected size aerosol (monodispersed) emerges. Clean sheath air is provided by the pump and absolute filter. The monodispersed aerosol is directed around EAC2 via path (2) and on into the CN counter. EAC1 is stepped through a selection of voltages (aerosol particle sizes) and a particle concentration is taken at each particle size with the CN counter, and hence a size distribution is generated. The aerosol can be directed around both EAC's via path (3) and sent directly to the CN counter to get a total CN count. The count versus voltage data set must be numerically analyzed in order to generate the actual size distribution (Ref. E-8). Here we note that an interesting feature of the EAC is that it not only takes a polydisperse aerosol and separates out a monodisperse fraction, but it also transfers this monodisperse fraction to the clean sheath air stream. The EAC can likewise be used to remove aerosol from the original sample air stream. This methodology applies for both total aerosol sampling and for non-volatile aerosol sampling. In the latter case an in-line preheater set at 175°C provides the means to separate the non-volatile component of the total aerosol flow.

E-2.3 AEROSOL HYDRATION EXPERIMENT

The UMR MASS can access aerosol hydration properties through the haze chamber or Laktionov technique (Refs. E-8, 9, and 10). Sample air is drawn into the MASS and size selected in EAC1 as above. This preselected monodispersed aerosol passes via path (4) to the saturator integrated into EAC2. Here it is brought to 100-percent relative humidity in the saturator, and the aerosol particles deliquesce to their equilibrium size at 100-percent relative humidity. Even though the particles entering the saturator are monodispersed in size, a spectrum of particle sizes will exit the saturator because of differences in particle chemistry and soluble mass fraction. To investigate the deliquesced particle size spectrum, the voltage on EAC1 is held fixed. The voltage (size setting) on EAC2 is then stepped through various values. The aerosol is passed onto the CN counter, and a count is taken for each voltage setting of EAC2. These counts can then be translated into a critical supersaturation spectrum for the particles of the size given by EAC1.

Under conditions where particles are sampled at or near the exit plane of an exhaust nozzle, the particle emission index can be determined by measurement of the number of particles emanating from the engine per cm^3 of gas in the exhaust flow, and knowledge of fuel/air ratio at the sample location. The latter quantity can be simply related to the mass of fuel (in kilograms) for each cm^3 of gas passing through the engine. The ratio of the number of particles per cm^3 to the kilograms of fuel per cm^3 yields the number-based emission index. A mass-based EI has also been estimated (Table E-2). In this case a soot volume fraction (SVF) was extracted from appropriate size distribution data, assuming all particles to be spherical and of known diameters. This SVF was then converted into mass units by employing an average particle density of 2 gm/cm^{-3}.

E-3.0 PARTICLE CHARACTERIZATION RESULTS

In this project the following aerosol properties were characterized as a function of altitude and T3 and P3: total concentration, aerosol, number- and mass-based emission indices, soot volume fraction, total aerosol and non-volatile aerosol size distributions and hydration (soluble mass fraction). Table E-1 is a compilation of the aerosol concentration [CN] and number-based emission indices EI(CN). Information relating to data acquisition start times, test facility data acquistion steady-state data point (SSDP) number, sample source defined by probes sampled, T3, P3, percent CO_2, and altitude are also provided. Figures E-2 through E-4 are correlations made between these data and other test parameters, i.e., Fig. E-2 is a plot of the aerosol number-based emission indices as a function of thrust (as represented by CO_2 concentration) at simulated sea-level-static (SLS); Fig. E-3 is a plot of aerosol number-based emission indices as a function of altitude; and Fig. E-4 is a plot of aerosol number-based emission indices as a function of T3 for 9.1 km. These data show no strong correlation between aerosol emission index and thrust, altitude, and combustor inlet temperature. However, there appears to be a correlation between combustion efficiency and aerosol

emission index observed in the ground idle data points, where elevated emission indices for aerosols, CO, and unburned hydrocarbons are recorded.

Size distributions for total aerosol and non-volatile aerosol samples were recorded for a selected subset of conditions and sample sources. Table E-2 lists the time, test facility SSDP number, sample source, and UMR data point (run number) for all of the size distributions measured. Plots of these distributions are given in Figs. E-5 through E-14. In these figures each size distribution is identified by UMR data run number, time, test facility SSDP, and altitude.

Hydration data analyzed as the fraction of a given aerosol sample population as a function of soluble mass fraction were acquired for aerosol dry sizes 20, 50, and 80 nm and continue to be deconvolved. The general observation from these data is that very little soluble mass is found on these aerosols with very few aerosols having a soluble mass fraction > 0.1. The dry sizes of 20, 50, and 80 nm were chosen because these sizes tend to encompass the peak in the size distribution typically observed for aircraft engine soot emissions.

E-4.0 CONCLUSIONS

The purpose of this report is to provide the scientific community with the data from this altitude chamber test as soon as possible. As a result at this time only the following preliminary conclusions can be drawn from these data. This is the first database of its kind and provides particulate characterization (i.e., total concentration, aerosol, number- and mass-based emission indices, aerosol (soot) volume fraction, total aerosol, and non-volatile aerosol size distributions and hydration (soluble mass fraction)) for an advanced current commercial engine simulation operating at 0.8 Mach cruise conditions at altitudes from simulated SLS to 15.2 km. These data characterize the aerosol generated in the engine and that continues to exist at a distance <10 cm downstream of the exit plane of the engine exhaust nozzle.

There is no strong correlation between emission index and thrust (measured as CO_2 concentration), altitude, or combustor inlet temperature (T3). However, there is a correlation between combustion efficiency and aerosol emission index. In the case at SLS where CO and unburned hydrocarbon emission indices are elevated, a similar elevation is observed in the aerosol emission index. The mean aerosol number-based emission index calculated from all measurements is $(2.2 \pm 0.7) \times 10^{15}$, the associated mean mass-based emission index is 0.012 ± 0.001 (where the quoted uncertainty in both cases is the standard deviation of the mean).

Typical size distributions are log-normal and peak in the vicinity of 20 to 40 nm diameter. The volatile component is small and in most cases can be considered negligible.

When exposed to a supersaturation pulse, the aerosol concentrations in sample flows were enhanced by at least a factor of four.

E-5.0 CO_2 DIAGNOSTIC TEST

The McDonnell Douglas CO_2 detector was designed to be an efficient, compact, and portable means of detecting CO_2 to be used in conjunction with the Mobile Aerosol Sampling System (MASS) in order to obtain emission indices during ground testing of aircraft engines.

Air from the engine exhaust flowed through two absorption cells before being exhausted to the mechanical pump (Fig. E-15). The flow was regulated with a flowmeter located downstream of the cells. The flow meter was set to 1 liter/min. The pressure in the cells was continually monitored using a capacitance manometer.

The pressure in the absorption cells was maintained near 1 atm by regulating the flow through the detector with a valve located upstream of the CO_2 detector. The air from the engine exhaust was preconditioned before entering the detector by flowing the air over Dryerite* to remove water vapor and by flowing it through a filter to remove particles.

The absorption cells are commercially obtained units which detect absorption of the v_3 band of CO_2 near 4.25 μm. These cells were connected in parallel to each other and to the capacitance manometer.

The absorption cells each consisted of a modulated infrared light source, an infrared filter centered at 4.25 μm, an absorption cell, and a detector. The path lengths of the two cells were fabricated to maximize sensitivity for Cell 1 of 0 to 2 percent CO_2 and 0 to 3000 ppm for Cell 2.

E-5.1 CALIBRATION VERSUS KNOWN CO_2 CONCENTRATIONS

The absorption cells are calibrated at the factory to read in percent CO_2 for a gas at standard temperature and pressure. The absorption of the light is determined by Beer's Law, $\log(I/I_0) = -\varepsilon L$, where I_0 is the unattenuated light intensity, I is the attenuated intensity, L is the length of the cell, and ε is the absorption of CO_2. The absorption, ε, is proportional to the density of CO_2 in the cell; therefore, the cells are calibrated at the factory with gases of known percentages of CO_2 in the range of interest. Calibration curves are then generated over the range of interest and fit with a multiparameter fitting equation. These curves are then programmed into a microprocessor so that the microprocessor outputs a voltage that is linearly proportional to the percent of CO_2 for a given detector attenuation (I/I_0). This process is accurate only over a limited range of CO_2 partial pressures.

We have increased this range by employing two absorption cells of differing ranges. In this manner we can monitor CO_2 percentages from 10 percent down to below 300 ppm. We checked the factory calibrations in our laboratory using gases with known concentrations of CO_2. These included calibration gases of 2 percent, 0.2 percent, 1000 ppm and 300 ppm.

E-5.2 MEASUREMENT OF THE ENGINE EXHAUST

The purpose of employing our detector in these tests was to validate our detector by comparison with standard techniques. The CO_2 in engine exhaust was measured by employing the procedure described above. CO_2 concentrations were derived using the readings from the absorption cells. Absolute densities of CO_2 were determined using the CO_2 readings and the pressure and temperature of the absorption cells and the ideal gas law ($PV = nRT$).

The system as currently constructed is limited to making measurements at cell pressures at or above ambient pressure. This is the normal condition encountered under ground test conditions. Therefore, we limited our comparisons with other measurements taken by other groups during the engine testing to those which were taken at above ambient pressures. These comparisons showed our measurements to be always within 5 percent of the AEDC CO_2 measurements using an NDIR analyzer (Appendix B). The AEDC CO_2 gas sampling measurement results in turn compared favorably with the fuel-to-air ratios determined from the test facility engine performance data.

The system can be enhanced to make measurements at sub-ambient pressures by employing a two-chamber vacuum pump so that the blank-off pressure of the system is much less than the pressure in the engine exhaust.

REFERENCES

E-1. Hagen, D. E., Trueblood, M. B. and Podzimek J. "Combustion Aerosol Scavenging." *Atmospheric Environment*, 25A, 2581, 1991.

E-2. Hagen, D. E., Trueblood, M. B., and Whitefield P. D. "A Field Sampling of Jet Exhaust Aerosols." *Particle Science & Technology*, 10, 53–63, 1992.

E-3. Hagen, D. E., Podzimek, J., and Trueblood, M. B. "Upper Tropospheric Aerosol Sampled During Project FIRE IFO II." *Journal of Atmospheric Science*, accepted 1995.

E-4. Hagen, D. E., Whitefield, P. D., Trueblood, M.B., and Lilenfeld, H.V. "Particulates and Aerosols Characterized in Real Time from Harsh Environments using the UMR Mobile Aerosol Sampling System (MASS)." AIAA 93-2344, AIAA, SAE, ASME, ASEE 29th Joint Conf., Monterey, CA, June 1993.

E-5. Whitefield, P. D. and Hagen, D. E. "Particulates and Aerosols Sampling from Combustor Rigs Using the UMR MASS." AIAA 95-0111 33rd Aerospace Sciences Meeting, Reno, NV, January 1995.

E-6. Hagen, D. E., Trueblood, M. B., and White, D. R. "Hydration Properties of Combustion Aerosols." *Aerosol Science and Techology*, 10, 63–69 (1989).

E-7. Hagen, D. E. and Alofs, D. J. "A Linear Inversion Method to Obtain Aerosol Size Distributions from Measurements with a Differential Mobility Analyzer." *Aerosol Science and Technology*, 2, 465-475 (1983).

E-8. Alofs, D. J., Trueblood, M. B., White, D. R., and Behr, V.L. "Nucleation Experiments with Monodisperse NaCl Aerosols." *Journal of Applied Meteor.*, 18, 1106–1117 (1979).

E-9. Alofs, D. J. and Podzimek, J. "A Review of Laktionov's Isothermal Cloud Nucleus Counter", *Journal of Applied Meteor.*, 13, 511–512 (1974).

E-10. Podzimek J., Truebolld, M.B., and Hagen, D.E., "Condensation Nucleii Activation or Deactivation by Deposited Insoluble Particles." *Atmospheric Environment*, 25A 2587 (1991).
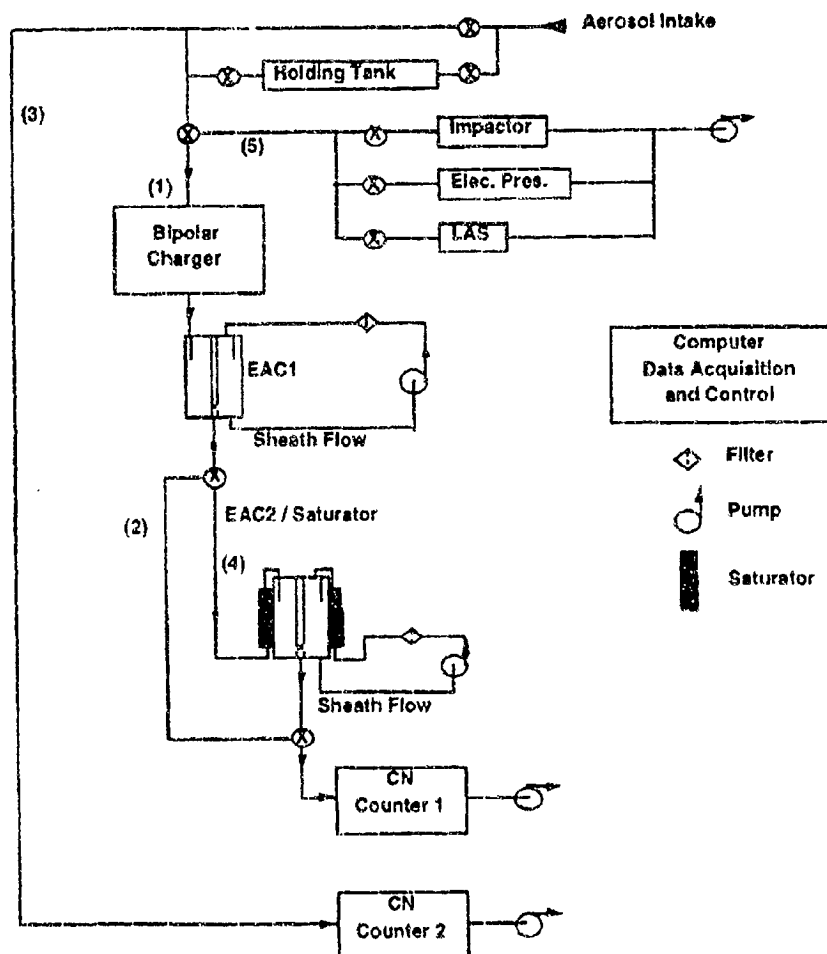
Figure E-1. UMR Mobile Aerosol Sampling System.

131
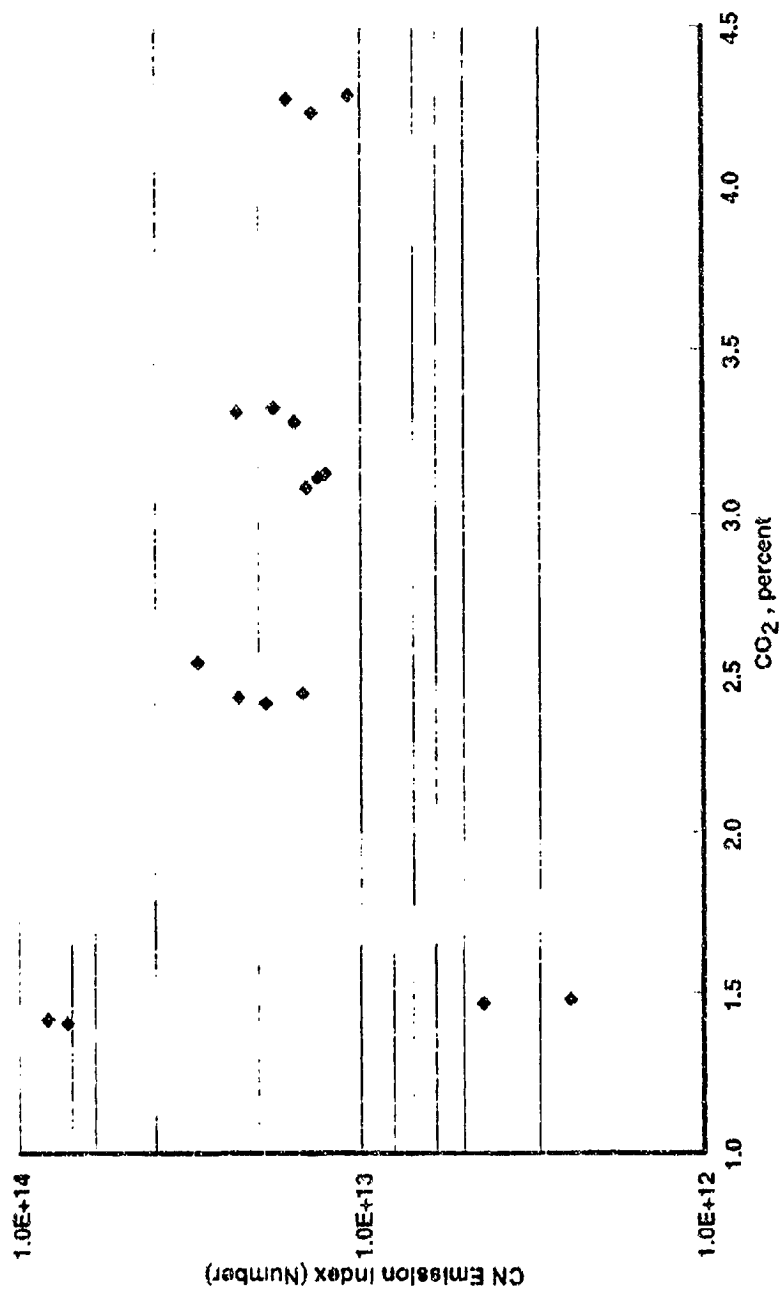
Figure E-2. EI(CN) (cor) versus CO_2 at simulated sea-level-static (3.1-km) altitude.

132
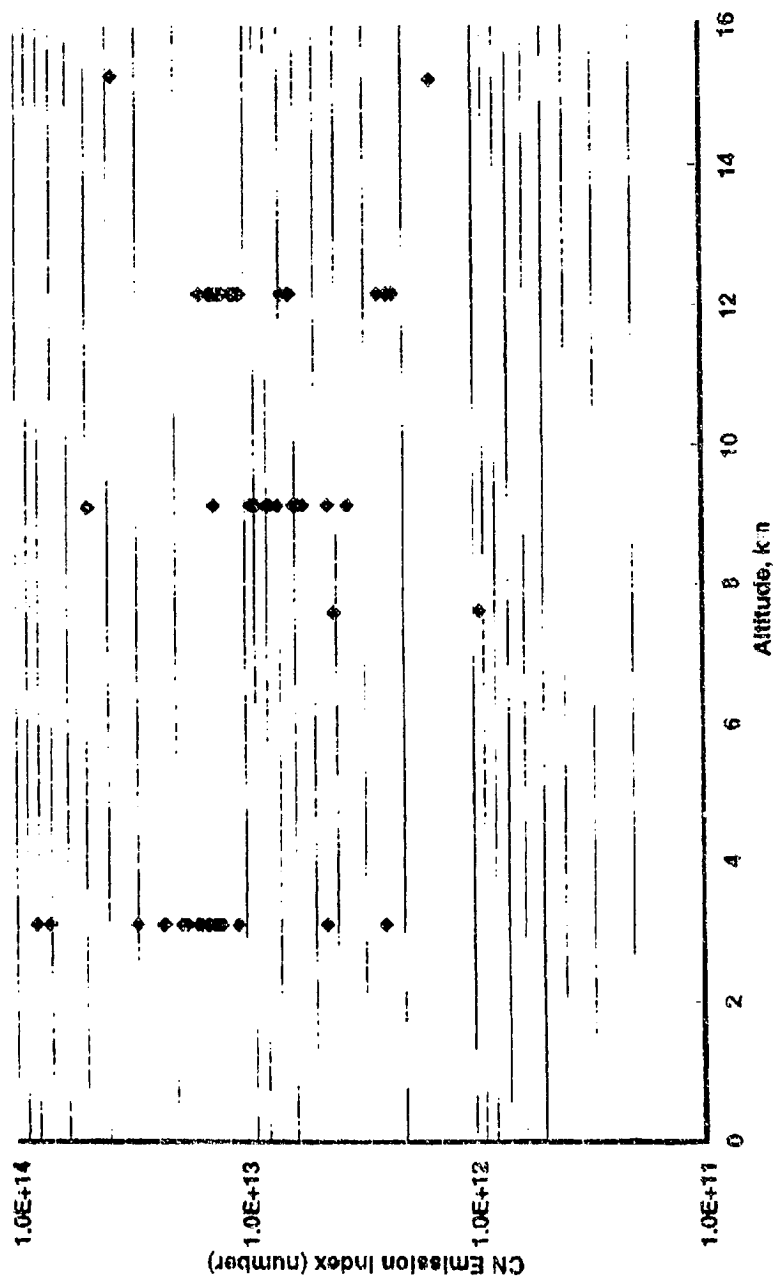
Figure E-3. EI(CN) (avg) vers is altitude.

133
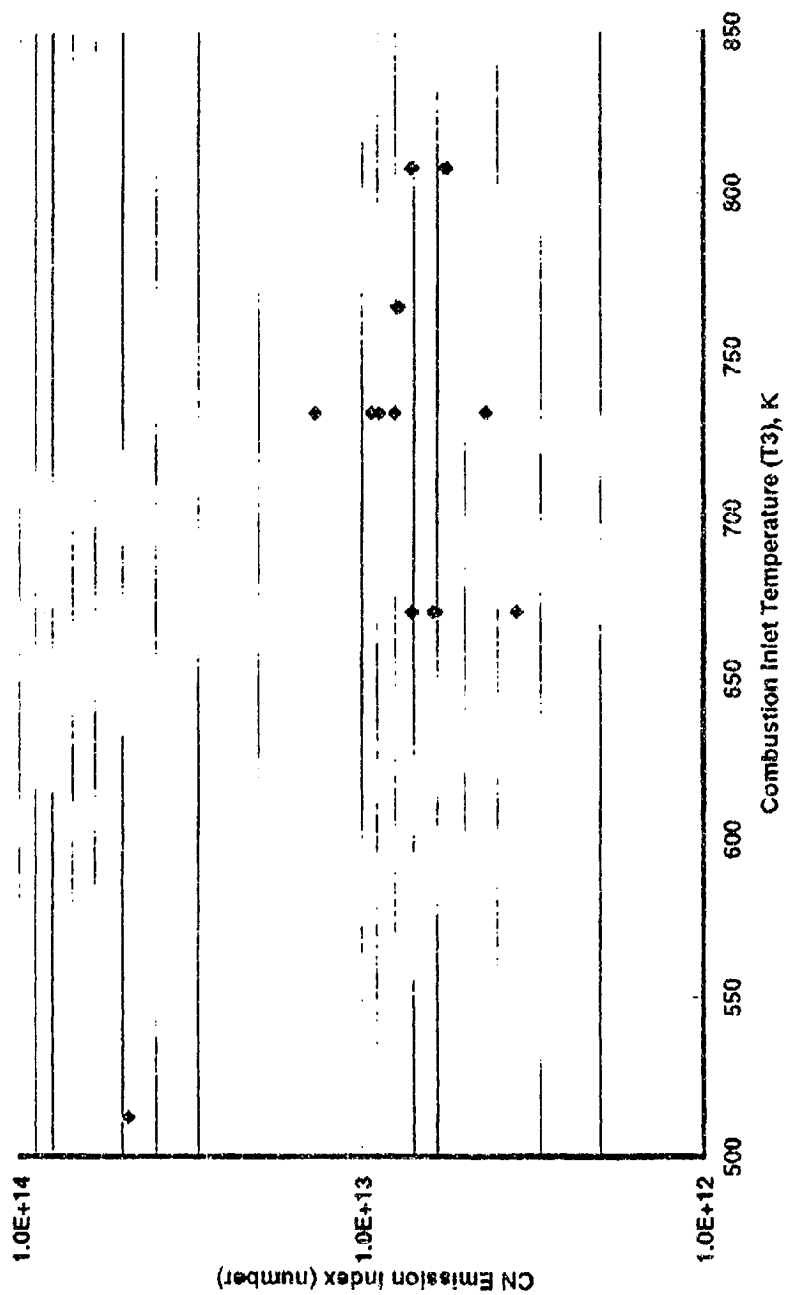
Figure E-4. EI(CN) (cor) versus combustion inlet temperature (T3) at 9.1-km altitude.
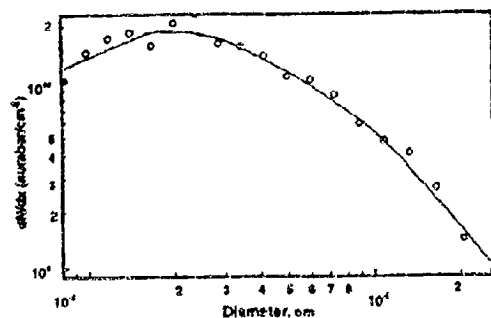
a. T3 and Altitude unknown,
Time = 07:57:00
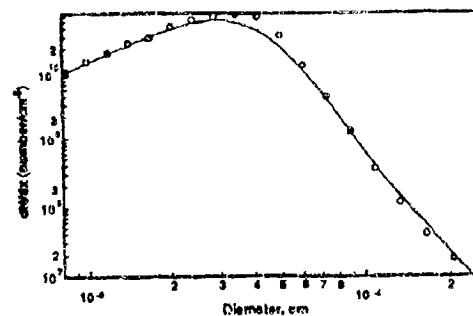
b. T3 = 764 K, Altitude = 7.6 km,
Time = 08:22:34
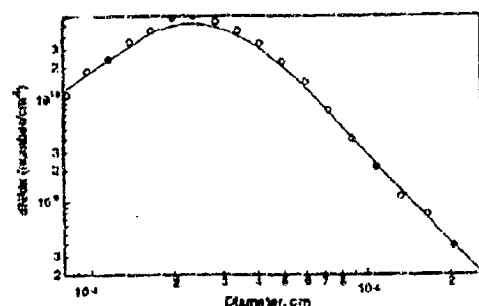
c. T3 = 733 K, Altitude = 7.6 km,
Time = 08:39:50
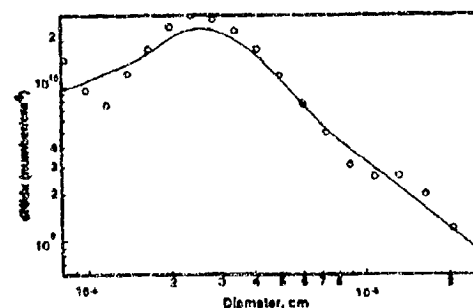
d. T3 and Altitude unknown,
Time = 08:59:30
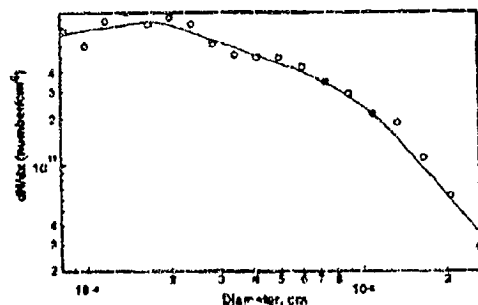
e. T3 and Altitude unknown,
Time = 09:05:30
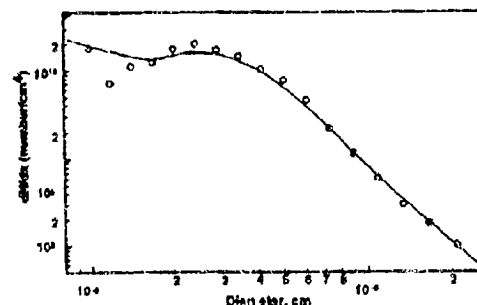
f. T3 = 733 K, Altitude = 9.1 km,
Time = 09:21:2A'

Figure E-5. Total aerosol size distribution, Set 1.
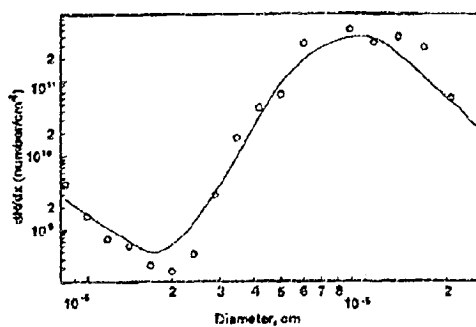
a. T3 = 733 K, Altitude = 9.1 km,
Time = 09:34:00
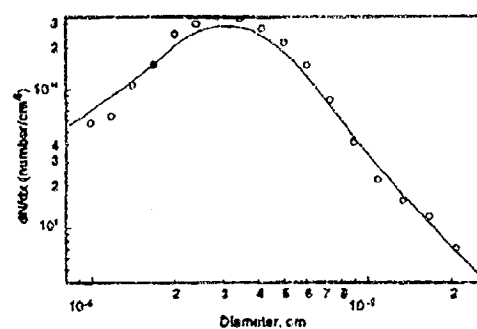
b. T3 = 733 K, Altitude = 9.1 km,
Time = 10:27:20
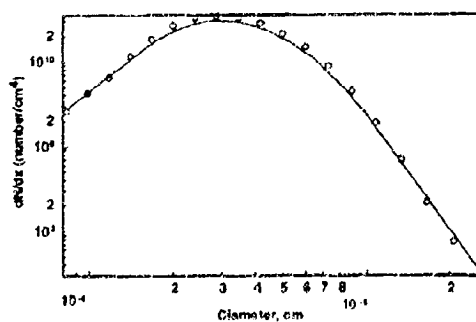
c. T3 = 733 K, Altitude = 9.1 km,
Time = 10:29:00
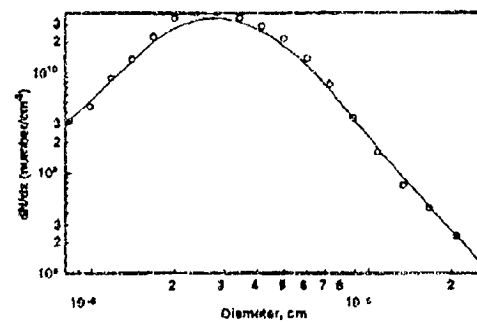
d. T3 = 733 K, Altitude = 9.1 km,
Time = 10:42:08
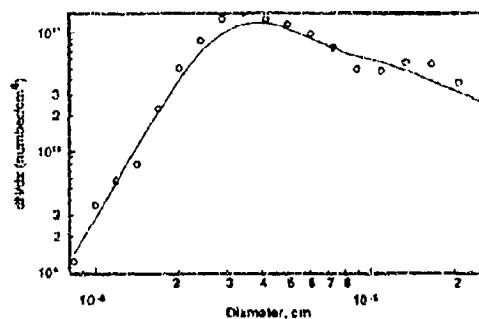
e. T3 = 733 K, Altitude = 9.1 km,
Time = 10:47:00
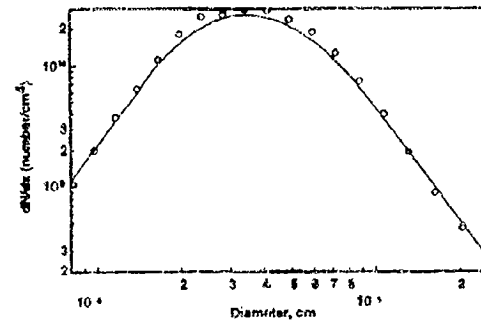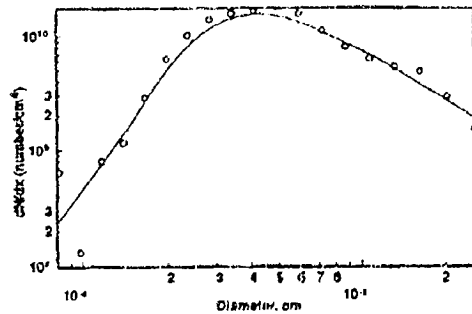
Figure E-6. Total aerosol size distribution, Set 2.
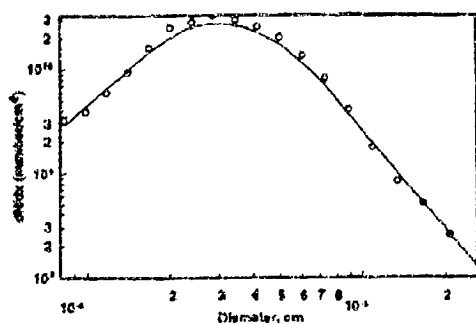
a. T3 = 733 K, Altitude = 9.1 km,
Time = 10:54:00
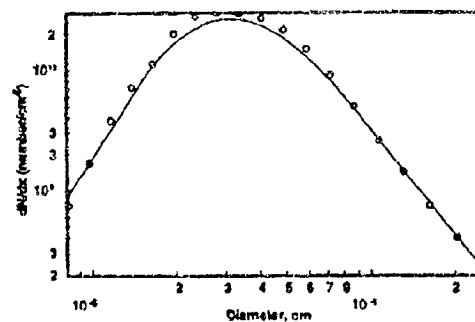
b. T3 = 733 K, Altitude = 9.1 km,
Time = 11:00:00
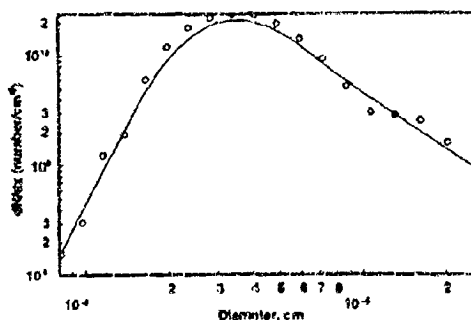
c. T3 = 733 K, Altitude = 9.1 km,
Time = 11:02:00
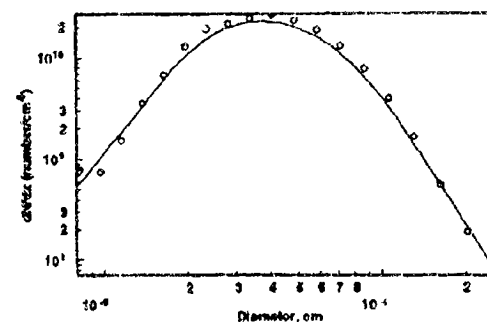
d. T3 = 765 K, Altitude = 9.1 km,
Time = 11:18:00
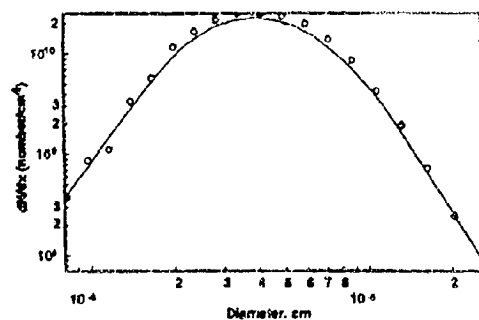
e. T3 = 808 K, Altitude = 9.1 km,
Time = 11:29:00
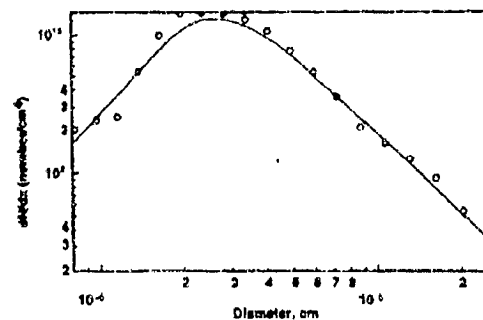
f. T3 = 671 K, Altitude = 9.1 km,
Time = 11:49:00

Figure E-7. Total aerosol size distribution, Set 3.
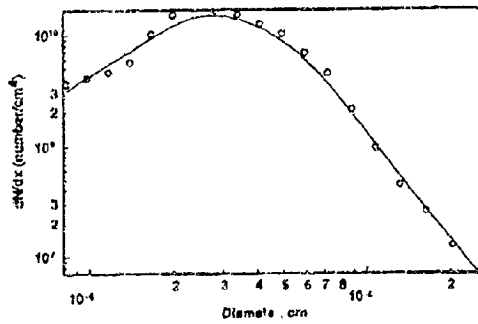
a. T3 = 727 K, Altitude = 12.2 km,
Time = 12:07:00
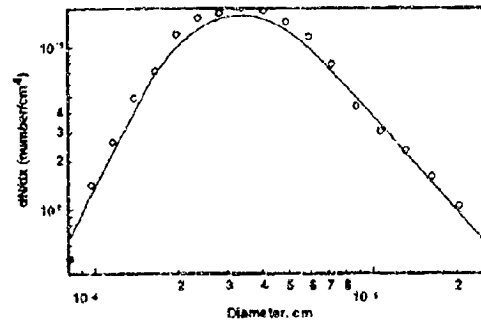
b. T3 = 727 K, Altitude = 12.2 km,
Time = 12:28:00
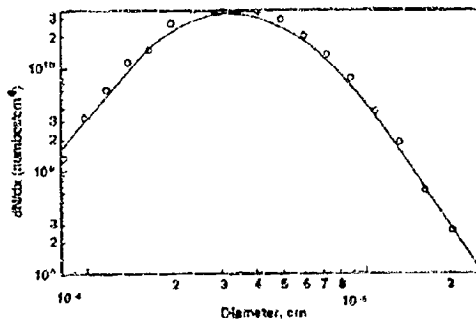
c. T3 = 766 K, Altitude = 12.2 km,
Time = 12:52:00

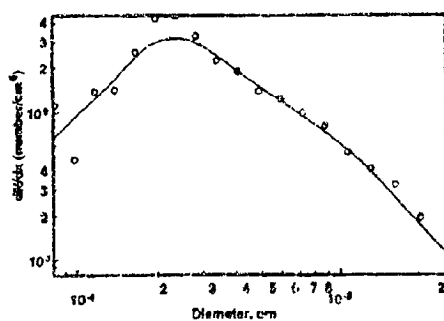d. T3 = 766 K, Altitude = 12.2 km,
Time = 12:56:00

e. T3 = 766 K, Altitude = 12.2 km,
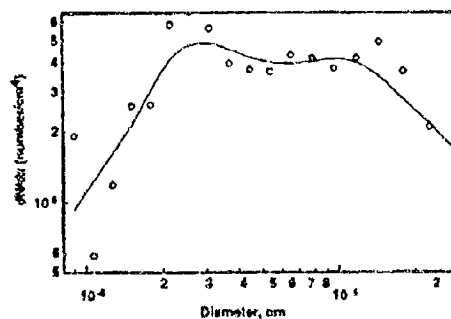Time = 13:00:00
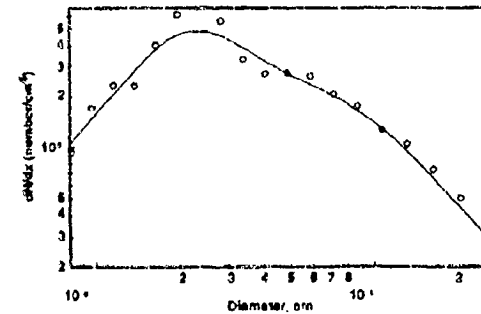
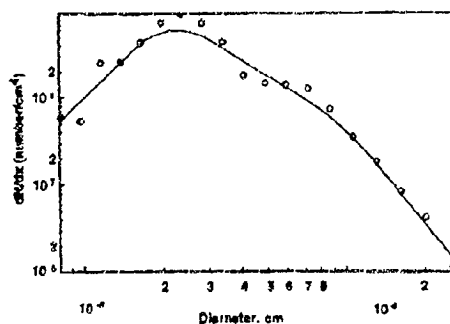f. T3 = 665 K, Altitude = 12.2 km,
Time = 13:20:00

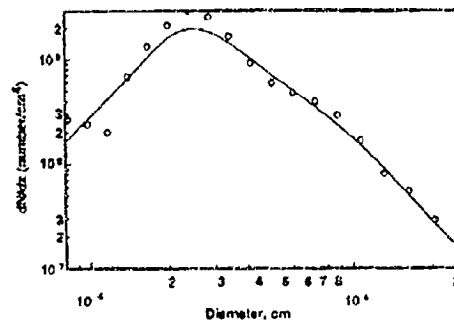Figure E-8. Total aerosol size distribution, Set 4.

a. T3 = 665 K, Altitude = 12.2 km,
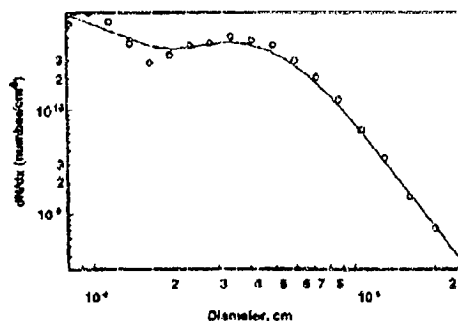Time = 13:24:00

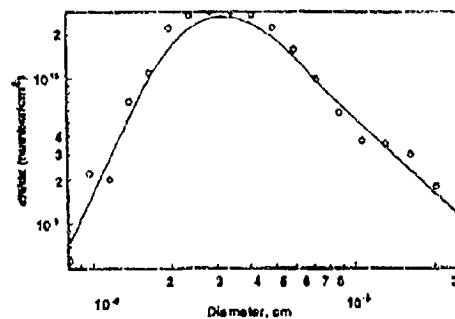b. T3 = 557 K, Altitude = 12.2 km,
Time = 13:30:00

c. T3 = 635 K, Altitude = 15.2 km,
Time = 13:45:00

d. T3 = 671 K, Altitude = 15.2 km,
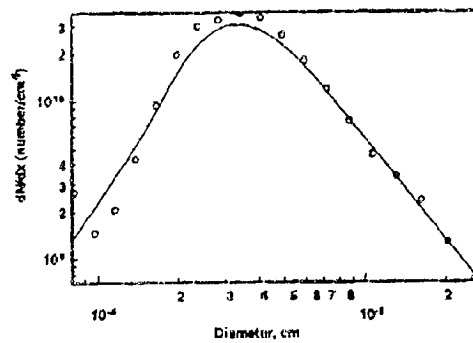Time = 14:00:00

e. T3 = 764 K, Altitude = 15.2 km,
Time = 14:18:00

f. T3 = 733 K, Altitude = 3.1 km(SLS),
Time = 14:57:00

Figure E-9. Total aerosol size distribution, Set 5.

a. T3 = 733 K, Altitude = 3.1 km(SLS), Time = 15:05:00

b. T3 = 733 K, Altitude = 3.1 km(SLS), Time = 15:38:00

c. T3 = 733 K, Altitude = 3.1 km(SLS), Time = 16:07:00

d. T3 = 669 K, Altitude = 3.1 km(SLS), Time = 16:24:00

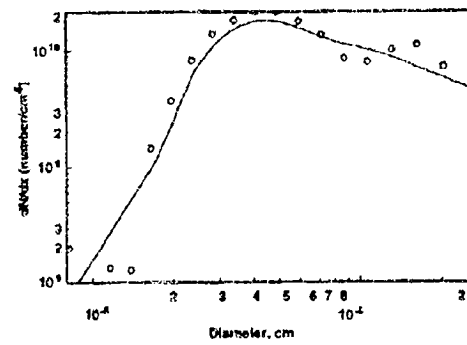e. T3 = 651 K, Altitude = 3.1 km(SLS), Time = 16:36:00

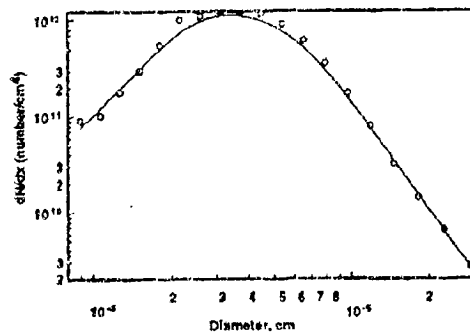f. T3 = 526 K, Altitude = 3.1 km(SLS), Time = 16:45:00

Figure E-10. Total aerosol size distribution, Set 6.
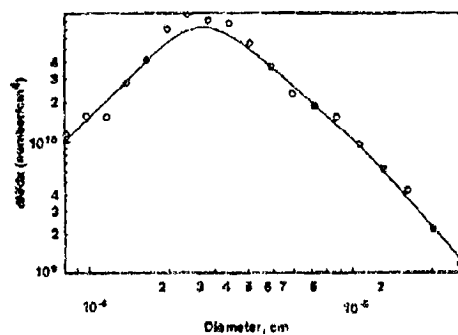
a. T3 = 517 K, Altitude = 3.1 km(SLS),
   Time = 16:55:00
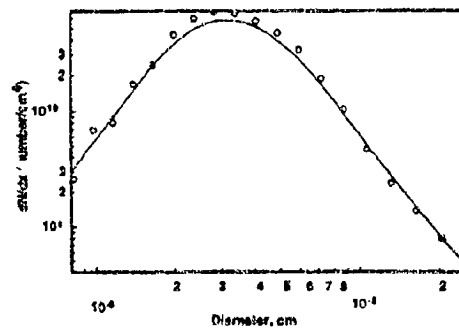
b. T3 = 762 K, Altitude = 3.1 km(SLS),
   Time = 17:08:00
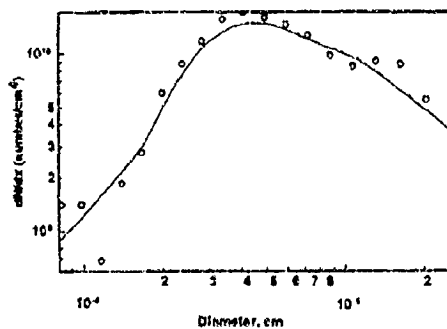
c. T3 = 861 K, Altitude = 3.1 km(SLS),
   Time = 17:19:00

Figure E-11. Total aerosol size distribution, Set 7.
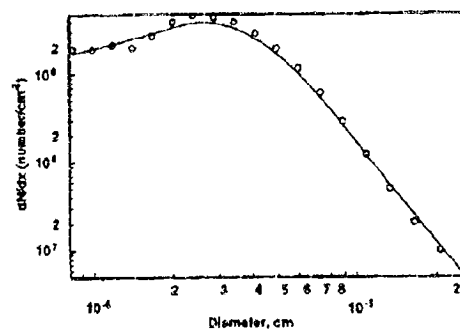
141

a. T3 and Altitude unknown,
Time = 07:57:00

b. T3 = 764 K, Altitude = 7.6 km,
Time = 08:22:34

c. T3 = 733 K, Altitude = 7.6 km,
Time = 08:39:50

d. T3 and Altitude unknown,
Time = 08:59:30
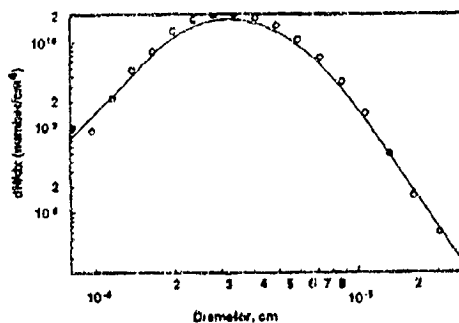
e. T3 = 733 K, Altitude = 9.1km,
Time = 10:29:00

Figure E-12. Non-volatile aerosol size distribution, Set 1.
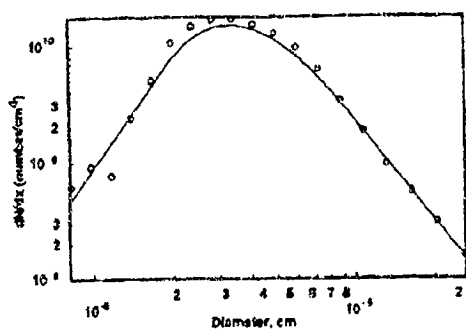
a. T3 = 733 K, Altitude = 9.1 km,
   Time = 11:00:00
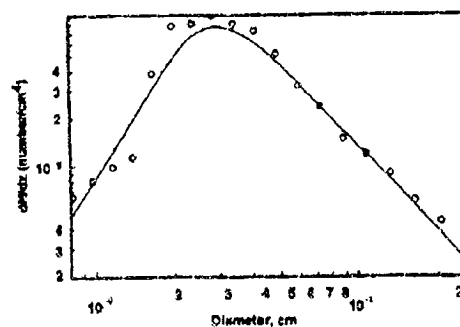
b. T3 = 671 K, Altitude = 9.1 km,
   Time =11:49:00
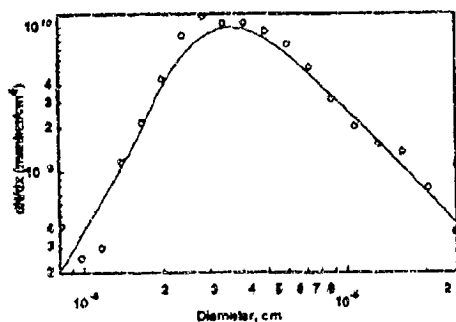
c. T3 = 727 K, Altitude = 12.2 km,
   Time = 12:28:00
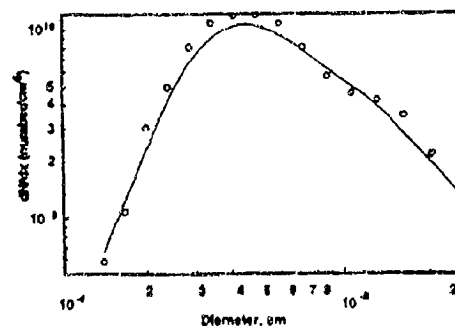
d. T3 = 766 K, Altitude = 12.2 km,
   Time = 13:00:00
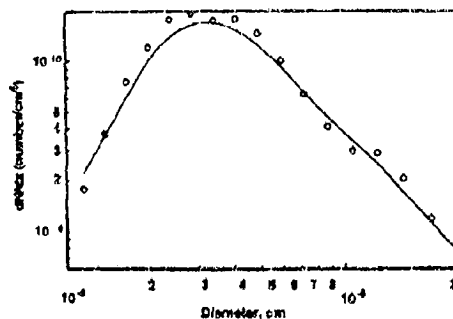
e. T3 = 733 K, Altitude = 3.1 km(SLS),
   Time = 14:57:00

Figure E-13. Non-volatile aerosol size distribution, Set 2.
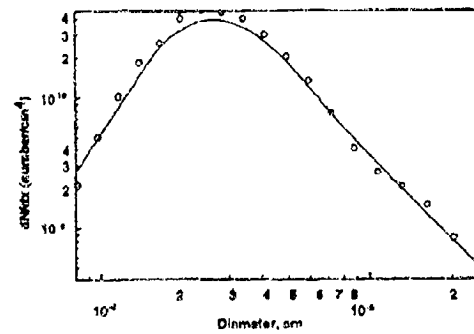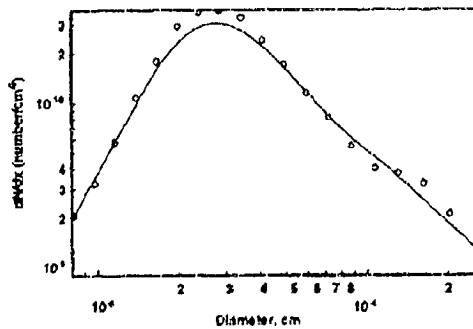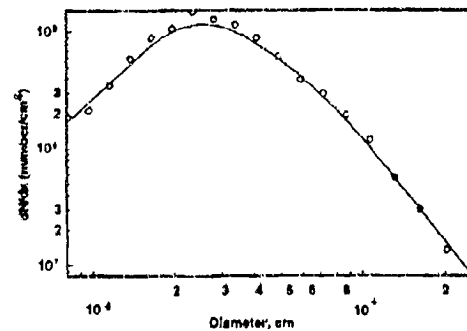
143

a. T3 = 733 K, Altitude = 3.1 km(SLS),
   Time = 15:05:00
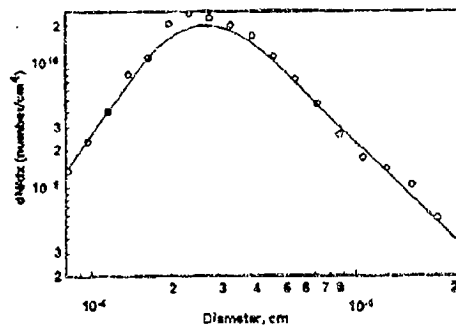
b. T3 = 669 K, Altitude = 3.1 km(SLS),
   Time = 16:24:00
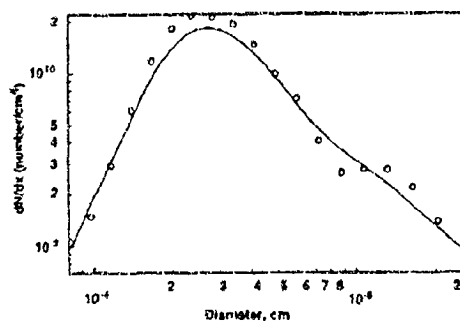
c. T3 = 651 K, Altitude = 3.1 km(SLS),
   Time = 16:36:00
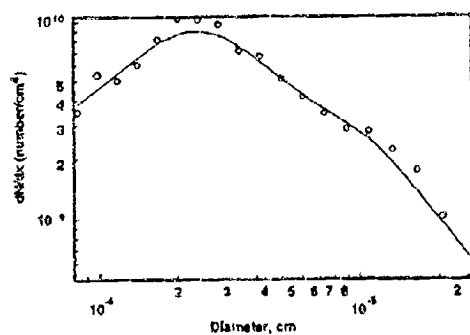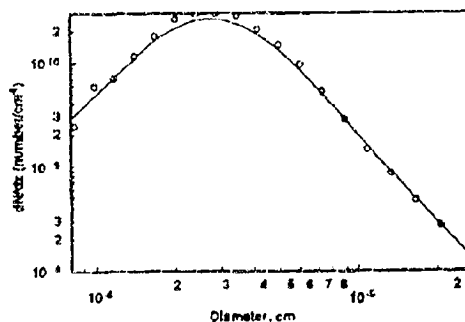
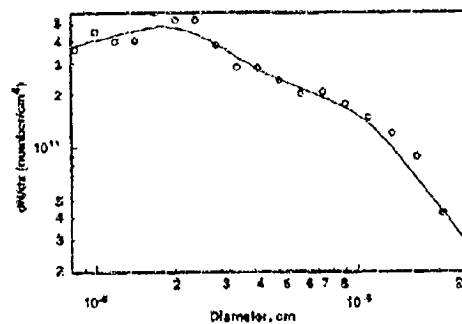Figure E-14. Non-volatile aerosol size distribution, Set 3.

Engine Exhaust Flow

Absorption Cell 1

To Pump

Capacitance Manometer

Absorption Cell 2

Flow Regulator
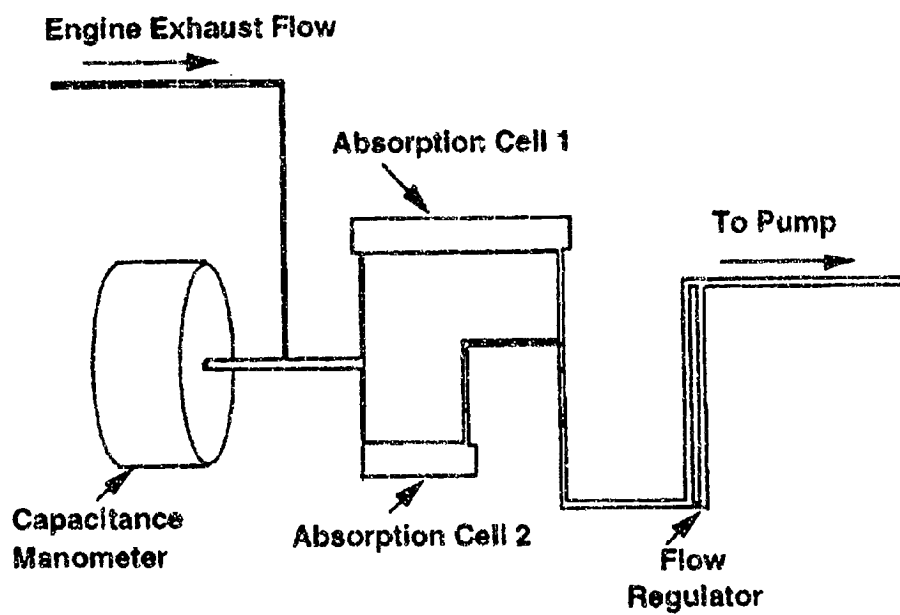
Figure E-15. McDonnell Douglas CO$_2$ detector.

Table E-1. CN Concentration and Number-Based EI as a Function of Test Parameters

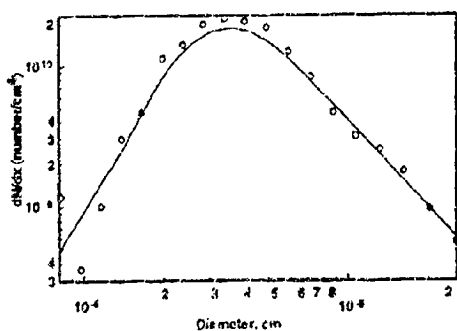| Time, sec	Time (h:m:s)	Facility SSDP	Sample Source	T3, K	P3, atm	[CN]	%CO₂	EI (CN)	Alt, km
29500	8:11:40	26	180,360	658	15.983	215875.6			7.6
30494	8:28:14	30	180,360	733	9.938	60000.0	3.18	4.04E+12	7.6
31410	8:43:30	32	180,360	668	7.084	12233.3	2.72	9.42E+11	7.6
32800	9:06:40	35	180,360	512	3.240	195773.7	1.61	4.82E+13	9.1
33384	9:16:24	37,38,40-49	P10	733	11.872	20775.7	3.34	2.74E+12	9.1
33446	9:17:26	37,38,40-49	P11	733	11.872	4112.3	3.39	5.35E+11	9.1
33504	9:18:24	37,38,40-49	P12	733	11.872	6316.7	3.40	8.20E+11	9.1
33564	9:19:24	37,38,40-49	P13	733	11.872	82747.8	3.10	5.69E+12	9.1
33720	9:22:00	37,38,40-49	P14	733	11.872	69695.6	2.30	8.69E+12	9.1
33840	9:24:00	37,38,40-49	P33	733	11.872	109225.5	1.78	1.33E+13	9.1
33900	9:25:00	37,38,40-49	P32	733	11.872	38304.2	2.90	2.86E+12	9.1
33960	9:26:00	37,38,40-49	P31	733	11.872	80732.3	3.86	4.77E+12	9.1
34020	9:27:00	37,38,40-49	P30	733	11.872	121611.0	3.71	7.09E+12	9.1
34080	9:28:00	37,38,40-49	P29	733	11.872	59469.0	3.44	3.74E+12	9.1
34140	9:29:00	37,38,40-49	P28	733	11.872	96157.8	3.30	6.20E+12	9.1
34260	9:31:00	37,38,40-49	180	733	11.872	70798.1	3.46	4.36E+12	9.1
34320	9:32:00	37,38,40-49	360	733	11.872	148450.1	3.37	9.39E+12	9.1
37800	10:30:00	37,38,40-49	Full Cross	733	11.872	90581.3	3.43	8.04E+12	9.1
38468	10:41:08	37,38,40-49	90,270	733	11.872	155273.3	3.42	1.38E+13	9.1
38582	10:43:02	37,38,40-49	P19	733	11.872	75561.9	3.32	6.91E+12	9.1
38660	10:44:20	37,38,40-49	P20	733	11.872	146161.5	3.36	8.65E+12	9.1
38710	10:45:10	37,38,40-49	P21	733	11.872	145327.1	3.58	8.12E+12	9.1
38760	10:46:00	37,38,40-49	P22	733	11.872	148319.2	3.58	8.26E+12	9.1
38950	10:49:10	37,38,40-49	P23	733	11.872	131285.6	2.70	9.70E+12	9.1
39050	10:50:50	37,38,40-49	P24	733	11.872	109880.1	1.37	1.60E+13	9.1
39075	10:51:15	37,38,40-49	P6	733	11.872	145982.3	1.79	1.62E+13	9.1
39120	10:52:00	37,38,40-49	P5	733	11.872	148765.4	2.67	1.14E+13	9.1
39180	10:53:00	37,38,40-49	P4	733	11.872	149829.8	3.27	9.35E+12	9.1
39360	10:56:00	37,38,40-49	P3	733	11.872	151509.3	3.47	8.70E+12	9.1
39420	10:57:00	37,38,40-49	P2	733	11.872	153150.7	3.41	8.95E+12	9.1
39480	10:58:00	37,38,40-49	P1	733	11.872	150365.2	3.30	9.08E+12	9.1
39540	10:59:00	37,38,40-49	90	733	11.872	153546.8	3.28	9.33E+12	9.1
39660	11:01:00	37,38,40-49	270	733	11.872	153132.0	3.44	8.87E+12	9.1
40560	11:16:00	51,52	360	765	13.334	143172.7	3.63	7.86E+12	9.1
40620	11:17:00	51,52	180	765	13.334	144264.7	3.73	7.71E+12	9.1
40740	11:19:00	51,52	360,180	765	13.334	153110.8	3.85	7.88E+12	9.1
41160	11:26:00	54,55	360,180	808	14.576	155048.7	4.03	7.24E+12	9.1
41280	11:28:00	54,55	180	808	14.576	157518.3	4.11	7.15E+12	9.1

Table E-1. Continued

Time, sec	Time (h:m:s)	Facility SSDP	Sample Source	T3, K	P3, atm	[CN]	%CO$_2$	EI (CN)	Alt, km
41370	11:29:30	54,55	180	808	14.576	127575.9	4.11	5.79E+12	9.1
41460	11:31:00	54,55	360	808	14.576	120858.0	4.01	5.61E+12	9.1
42180	11:43:00	57,58	360	671	8.779	91527.1	2.70	7.16E+12	9.1
42380	11:46:00	57,58	360	671	8.779	78689.5	2.70	5.98E+12	9.1
42480	11:48:00	57,58	180	671	8.779	46427.3	2.77	3.53E+12	9.1
42600	11:50:00	57,58	360,180	671	8.779	78698.4	2.71	6.13E+12	9.1
43500	12:05:00	60-64	360,180	727	8.300	82201.4	3.53	6.25E+12	12.2
43560	12:06:00	60-64	360	727	8.300	86688.6	3.40	6.85E+12	12.2
43700	12:08:20	60-64	180	727	8.300	145266.9	3.54	1.10E+13	12.2
44430	12:20:30	60-64	360,180	727	8.300	183217.0	3.53	1.42E+13	12.2
44520	12:22:00	60-64	360	727	8.300	116175.7	3.40	1.05E+13	12.2
44600	12:23:20	60-64	180	727	8.300	166833.8	3.54	1.29E+13	12.2
44640	12:24:00	60-64	P10 + P28	727	8.300	145823.8	3.42	1.17E+13	12.2
44700	12:25:00	60-64	P11 + P29	727	8.300	129095.5	3.53	9.60E+12	12.2
44780	12:26:00	60-64	P12 + P30	727	8.300	102885.4	3.51	7.69E+12	12.2
44820	12:27:00	60-64	P13 + P31	727	8.300	107503.6	2.31	1.28E+13	12.2
44940	12:29:00	60-64	P13 + P31	727	8.300	119107.2	2.31	1.39E+13	12.2
46200	12:50:00	66,87,68	360,180	766	9.099	112329.5	3.70	1.08E+13	12.2
46350	12:53:00	66,87,68	360	766	9.099	164318.1	3.70	1.33E+13	12.2
46440	12:54:00	66,67,68	180	766	9.099	193961.2	3.70	1.57E+13	12.2
46500	12:55:00	66,67,68	360,180	766	9.099	176390.9	3.70	1.23E+13	12.2
46620	12:57:00	66,67,68	360	766	9.099	146296.8	3.70	1.03E+13	12.2
46700	12:58:20	66,67,68	180	766	9.099	199163.9	3.70	1.39E+13	12.2
46760	12:59:20	66,87,68	360,180	766	9.099	163862.2	3.70	1.14E+13	12.2
47960	13:19:20	71,72	360,180	665	6.331	50550.8	2.98	6.34E+12	12.2
48060	13:21:00	71,72	360	665	6.331	21089.6	2.98	2.34E+12	12.2
48120	13:22:00	71,72	180	665	6.331	20879.6	2.98	2.22E+12	12.2
48160	13:23:00	71,72	360,180	665	6.331	24346.6	2.98	2.59E+12	12.2
50330	13:58:50	79	180,360	671	4.011	8900.0	3.18	1.52E+12	15.2
51420	14:17:00	63,84	180,360	764	5.645	340000.0	3.98	3.79E+13	15.3
53610	14:53:30	86-94	P10	733	18.741	223564.4	3.16	1.35E+13	3.1(SLS)
53640	14:54:00	86-94	P11	733	18.741	212166.0	3.29	1.23E+13	3.1(SLS)
53700	14:55:00	86-94	P12	733	18.741	198187.9	3.25	1.15E+13	3.1(SLS)
53760	14:56:00	86-94	P13	733	18.741	184831.7	2.43	1.44E+13	3.1(SLS)
53880	14:58:00	86-94	P14	733	18.741	158344.3	1.39	2.18E+13	3.1(SLS)
53950	14:59:10	86-94	P33	733	18.741	97818.1	1.39	1.36E+13	3.1(SLS)
54020	15:00:20	86-94	P32	733	18.741	211030.0	2.43	1.67E+13	3.1(SLS)
54060	15:01:00	86-94	P31	733	18.741	230739.0	3.25	1.37E+13	3.1(SLS)

Table E-1. Concluded

Time, sec	Time (h:m:s)	Facility SSDP	Sample Source	T3, K	P3, atm	[CN]	%CO₂	EI (CN)	Alt, km
54120	15:02:00	86-94	P30	733	18.741	238004.6	3.29	1.37E+13	3.1(SLS)
54180	15:03:00	86-94	P29	733	18.741	220117.0	3.16	1.33E+13	3.1(SLS)
54250	15:04:10	86-94	P28	733	18.741	188277.1	3.09	1.16E+13	3.1(SLS)
54375	15:06:15	86-94	180	733	18.741	235153.8	3.09	1.45E+13	3.1(SLS)
54420	15:07:00	86-94	360	733	18.741	217029.7	3.12	1.33E+13	3.1(SLS)
54460	15:08:00	86-94	180,360	733	18.741	210315.6	3.13	1.27E+13	3.1(SLS)
57280	15:54:40	86-94	P19	733	18.741	236441.9	3.08	1.92E+13	3.1(SLS)
57320	15:55:20	86-94	P20	733	18.741	263850.1	3.14	1.60E+13	3.1(SLS)
57360	15:56:00	86-94	P21	733	18.741	256059.3	3.28	1.49E+13	3.1(SLS)
57420	15:57:00	86-94	P22	733	18.741	244430.3	3.27	1.42E+13	3.1(SLS)
57550	15:59:10	86-94	P23	733	18.741	210031.9	2.17	1.84E+13	3.1(SLS)
57610	16:00:10	86-94	P24	733	18.741	142027.9	0.82	3.30E+13	3.1(SLS)
57675	16:01:15	86-94	P6	733	18.741	165384.1	1.03	3.08E+13	3.1(SLS)
57750	16:02:30	86-94	P5	733	18.741	164247.0	2.12	1.49E+13	3.1(SLS)
57780	16:03:00	86-94	P4	733	18.741	196428.0	3.07	1.23E+13	3.1(SLS)
57840	16:04:00	86-94	P3	733	18.741	212583.2	3.24	1.26E+13	3.1(SLS)
57900	16:005	86-94	P2	733	18.741	253221.3	3.17	1.56E+13	3.1(SLS)
57960	16:06:00	86-94	P1	733	18.741	190684.3	3.37	1.10E+13	3.1(SLS)
59100	16:25:00	98,98	360	669	13.330	391127.1	2.54	2.99E+13	3.1(SLS)
59650	16:37:30	100,101	360	651	12.041	279557.7	2.43	2.28E+13	3.1(SLS)
59680	16:38:00	100,101	180	651	12.041	229123.8	2.41	1.89E+13	3.1(SLS)
59940	16:39:00	100,101	360,180	651	12.041	189376.1	2.44	1.49E+13	3.1(SLS)
60360	16:46:00	103,104	360	526	5.158	34077.3	1.47	4.39E+12	3.1(SLS)
60420	16:47:00	103,104	180 360,180	526	5.158	15805.2	1.48	2.43E+12	3.1(SLS)
60960	16:56:00	105,106	360	517	4.766	507454.3	1.42	8.20E+13	3.1(SLS)
61020	16:57:00	105,106	180	517	4.766	437381.1	1.41	7.20E+13	3.1(SLS)
61620	17:07:00	108,109	360,180	762	21.473	328168.1	3.33	1.81E+13	3.1(SLS)
61740	17:09:00	108,109	360	762	21.473	417273.6	3.32	2.31E+13	3.1(SLS)
61800	17:10:00	108,109	180	762	21.473	273898.7	3.29	1.56E+13	3.1(SLS)
62280	17:18:00	111,112,113	360,180	861	30.458	250475.3	4.29	1.08E+13	3.1(SLS)
62400	17:20:00	111,112,113	360	861	30.458	378987.5	4.26	1.64E+13	3.1(SLS)
62460	17:21:00	111,112,113	180	861	30.458	315494.3	4.24	1.38E+13	3.1(SLS)

Table E-2. Size Distribution Index and Associated EI's Listed as a Function of Test Parameters

Time (h:m:s)	Time, sec	Total Aerosol	Non-Volatile	Tank Label	Fill Time, sec	Test Facility Steady-State Data Point	Sample Source (Valve Settings)	Altitude, km	Volume Fraction	EI (Number)	EI (Mass)	%CO₂
7:57:00	28620	1	2	1B(4B)	30	not listed	V+(10-14,28-33)	7.6				
8:22:34	30154	9	10	5A	40	28	V+(10-14,28-33)	7.6	4.33E-11	4.04E+12	0.001494	3.18
8:39:50	31190	12	13	5A	40	30	V+(10-14,28-33)	7.6				2.72
8:44:3	31470			2B	40	32	V+(10-14,28-33)	7.6				
6:59:36	32370	21		7A	40	not listed	V+(10-14,28-33)	9.1				
9:05:30	32730	26	27	8A	30	not listed	V+(28-33,10-14)	9.1	3.37E-10	5.93E+12	0.001736	3.10
9:21:24	33684	29		9A	40	37,38,40-49	single(V13)	9.1	6.98E-09	7.07E+12	0.001703	3.39
9:33:00	34380			10A	30	37,38,40-49	V+(28-33,10-14)	9.1	6.71E-11	4.59E+12	0.003620	3.42
9:34:00	34440	39		11A	-	37,38,40-49	V+(28-33,10-14)	9.1	2.15E-11	4.59E+12	0.001230	3.42
10:27:20	37640	51		1C	30	37,38,40-49	full across	9.1	3.07E-11	9.58E+12	0.003433	3.42
10:29:00	37740	56	57	2C	30	37,38,40-49	full across	9.1	2.62E-09	8.13E+12	0.028174	3.58
10:42:08	38526	59		3B	30	37,38,40-49	H+-(1-6,19-24)	9.1	3.30E-10	6.30E+12	0.002751	3.27
10:47:00	38820	64		4B	30	37,39,40-49	single(V22)	9.1	4.35E-11	6.82E+12	0.005569	3.28
10:54:08	39240	69		5B	30	37,38,40-49	single(V4)	9.1	1.15E-10	9.49E+12	0.014340	3.44
11:00:00	39600	76	77	6B	30	37,36,40-49	H+(1-6)	9.1	3.67E-11	7.14E+12	0.003323	3.73
11:02:00	39720	79		7B	30	37,38,40-49	H+(19-24)	9.1	4.11E-11	6.84E+09	0.000094	4.11
11:18:00	40680	82		8B	30	51,52	V+(28-33)	9.1	4.15E-11	2.96E+12	0.003198	2.77
11:29:00	41340	87		9B	30	54,55	V+(28-33)	9.1	1.63E-11	6.81E+12	0.002773	3.40
11:49:00	42540	92	93	10-B	30	57,58	V+(28-33)	12.2	8.14E-11	1.44E+13	0.019529	2.31
12:07:00	43620	95		11-B	33	60-64	V+(10-14)	12.2	4.14E-11	1.01E+13	0.004191	3.70
12:28:00	44860	105	106	1-D	40	60-64	V13,V31	12.2	5.49E-11	1.07E+13	0.006893	3.70
12:52:00	46320	108		2-C	40	66,67,68	V+(10-14,28-33)	12.2	2.09E-10	7.48E+12	0.018420	3.70
12:56:00	46560	113		3-C	50	66,67,68	V+(10-14,28-33)	12.2	3.44E-11	8.64E+12	0.015643	2.98
13:00:00	46800	118	119	4-C	50	66,67,68	V+(10-14,28-33)	12.2	1.43E-11	4.73E+12	0.006778	2.66
13:20:00	48000	125		5-C	50	71,72	V+(10-14,28-33)	12.2				2.14
13:24:00	48240	130		6-C	50	71,72	V+(10-14,28-33)	12.2				
13:30:00	48600	135		7-C	50	74,75	V+(10-14,28-33)	15.2				
13:45:00	49500	138		8-C	90	not listed	V+(10-14,28-33)	15.2				
14:00:00	50400	143		9-C	60	79	V+(10-14,28-33)	15.2	8.41E-13	1.52E+12	0.000910	3.18
14:03:30	50913			10-C	60	not listed	V+(10-14,28-33)	15.2				
14:16:00	51480	151		11-C	60	83,84	V+(10-14,28-33)	15.2	4.34E-11	3.79E+13	0.019356	3.98
14:57:00	53620	156	157	12-C	30	86-94	single(V13)	3 (SLS)	1.32E-10	1.55E+13	0.022249	2.43
15:05:00	54300	162	163	1-E	30	86-94	single(V28)	3 (SLS)	6.42E-12	1.35E+13	0.000856	3.09
15:53:00	57180	169		2E	30	86-94	V+(10-14,28-33)	3 (SLS)				3.13
15:58:00	57450	172		4D	45	88-94	single(V22)	3 (S&S)				3.27
16:07:00	58020			5D	45	86-94	single(V1)	3 (S&S)	7.03E-11	3.11E+13	0.022435	3.37
16:24:00	59040	175	176	6D	45	96,98	V+(10-14,28-33)	3 (SLS)				2.54
16:36:00	59760	178	179	7D	45	not listed	V+(10-14,28-33)	3 (SLS)				
16:45:00	60300	183		8D	45	103,104	V+(10-14,28-33)	3 (SLS)	1.61E-12	2.76E+12	0.001482	1.48
16:55:00	60900	188		9D	45	105,106	V+(10-14,28-33)	3 (SLS)	1.95E-10	1.53E+13	0.014532	1.42
17:08:00	61680	193		10D	45	108,109	V+(10-14,28-33)	3 (SLS)	8.65E-11	1.67E+13	0.008737	3.33
17:19:00	62340	196		4E	45	111,112,113	V+1(10-14,28-33)	3 (SLS)	3.66E-10	6.41E+11	0.002132	4.29

149

APPENDIX F
OH-UV LASER ABSORPTION SYSTEM

C. W. Brasier

J. A. Drakes

R. P. Howard

F-1.0 INTRODUCTION

A laser absorption system was installed in the test cell during the NASA test sequence as part of an ongoing effort to increase the diagnostic capability of AEDC. This effort represented the first turbine test cell entry of the AEDC UV laser measurement system. Consequently, the majority of the effort was aimed at understanding the dynamics of the test cell interactions with the laser system, even though a high priority was placed on the acquisition of data on OH concentration levels during this engine test period. Although OH absorption was not directly observed in the exhaust flow, the data are useful in that upper bounds to the OH concentration may be discerned from the detection threshold.

F-2.0 METHOD

The procedure for conducting and interpreting an absorption measurement is well established. For this application, a primary assumption was that the flow field was spatially uniform across the entire exit plane. In that case, the number density, N_I, of the OH in a given rotational state is determined by the absorption out of that state, denoted as I, to an upper state, denoted as 2, via,

$$N_1 = \left[\frac{c^2}{8\pi v_0^2} \frac{g_2}{g_1} A_{21} \right]^{-1} \int k_v dv \qquad (F-1)$$

where g_1 and g_2 represent the state degeneracies, A_{21} is the Einstein coefficient for the transition, v_0 is the frequency of the transition, and k_v is the absorption coefficient given by

$$k_v = \frac{1}{L} ln\left(\frac{I_0}{I}\right) = \frac{1}{L} ln\left(\frac{1}{\tau_v}\right) \qquad (F-2)$$

In this expression, I_0 refers to the measured incident laser intensity, I refers to the measured laser intensity after passing through the media. L refers to the physical path length of the media, and τ_v is the spectral transmission.

For this application, no absorption profiles were observed, so an assessment of the threshold detection was made. First, the absorption data from the individual laser frequency scans were averaged together and the nominal peak-to-peak noise was noted. To be conservative, the peak-to-peak noise variation was considered to be the largest possible signal due to OH absorption which could be present in the data. In other words,

$$k_{v_0} L \le \delta_{pp}(k_v L) \tag{F-3}$$

The peak height of the absorption line can be expressed as

$$k_{v_0} = S \sqrt{\frac{ln2}{\pi}} \frac{e^{a^2} \{1 - erf(a)\}}{\Upsilon_D} \tag{F-4}$$

where S is referred to as the line strength, which is simply the frequency integral of Eq. (F-2). The line strength can be directly converted into the state specific number density of the lower, absorbing state, N_l, and the Einstein coefficient of the transitions (i.e., A_{2l}), through Eq. (F-1). For this work, the Einstein coefficients were taken from first-principle calculations. In Eq. (F-4), a is the broadening parameter, which was taken as 0.2 for this work. Note that the results are extremely insensitive to the value of a chosen. The remaining parameter is the Doppler width of the spectral line, Υ_D, which is dependent on the gas static temperature. The appropriate reported temperature measurements from the probe data were used to determine Υ_D. Furthermore, the characteristic path length, L, was taken from the half-height points of the pressure profiles. Thus, by combining these factors with Eq. (F-3), it was possible to define an upper limit to the state specific number density.

In order to determine the total OH density from the state specific upper limit, the partition function was evaluated under the guiding assumption that the rotational and translational modes were in at least near equilibrium with each other, implying that the above probe temperatures could be used. The total OH(X) density then follows as

$$N_{OH} = \frac{N_1 Q(T)}{g_1 \exp(-E_1/kT)}, \tag{F-5}$$

where $Q(T)$ is the temperature-dependent partition function.

F-3.0 APPARATUS

Experimentally, the measurement followed the standard procedure for an amplitude-modulated absorption measurement, with a few modifications specific to this application. Shown in Fig. F-1 is a schematic of the experimental setup used for the OH absorption measurements. The system consisted of a continuous wave Coherent 699-21 scanning ring dye laser pumped by a Coherent INNOVA-400 argon-ion laser. Using Kiton Red laser dye, an intra-cavity Lithium Niobate frequency doubling crystal, and a pump laser power of 8 W at a wavelength of 514.5 nm, the ring laser output was nominally 3 mW single frequency at a wavelength of 306 nm. The frequency-doubled dye laser wavelength could be tuned over a wavelength range of approximately 304 nm to 327 nm with a frequency linewidth on the order of 500 kHz, which corresponds to a wavelength resolution of roughly 1.5×10^{-7} nm at 306 nm. The dye laser output frequency could be scanned ± 30 GHz about the selected absorption line of the OH molecule. A reference signal from the laser controller representing the laser frequency scan range was recorded by the data acquisition system.

A Burleigh wavemeter, model WA-10, and an OH discharge tube were included in the setup to provide laser diagnostic instrumentation. The wavemeter provides a convenient method of monitoring the fundamental laser wavelength, centered about 612 nm, during initial alignment and laser wavelength selection with a wavelength resolution of 0.003 nm. The frequency-doubled output of the dye laser was directed onto a retractable mirror which, when placed in the beam path, directs the beam to the OH discharge tube for additional verification of the proper laser wavelength. Once the OH absorption feature from the OH discharge tube was verified, the retractable mirror was removed, and the beam was then passed through a chopper wheel operating at 1.4 kHz and focused onto a 30-m, 200-μm core diameter UV grade multimode fiber optic cable for delivery to the test cell.

The beam arrangement in the test cell is shown schematically in Fig. F-2. At the fiber optic output the beam was split. Approximately 5 percent of the beam was directed onto a Hamamatsu 1P28 photomultiplier tube with a UV-enhanced photocathode for recording the laser power exiting the fiber optic cable. The photomultiplier output was passed through a pre-amp and a Stanford Research model SR-250 lock-in amplifier referenced to the 1.4-kHz chopper frequency and recorded in the data acquisition system. This reference signal was remotely monitored from the laser room so that minor adjustments to the laser beam alignment as it entered the fiber optic cable could be made in order to optimize the throughput.

After passing through the beam splitter in the test cell, the majority of the beam was directed across the turbine engine exit plane and onto a Hamamatsu 1P28 photomultiplier tube with UV-enhanced photocathode and pre-amp to provide the OH absorption measurement. The pre-amp out-

put was directed to a second Stanford Research model SR-250 lock-in amplifier referenced to the 1.4-kHz chopper frequency and recorded by the data acquisition system.

The data acquisition system consisted of a Data Translation 16-channel 12-bit A/D board inside a microcomputer. The laser frequency scan width, the fiber optic reference power, and the absorption signal were all recorded by this unit. During the OH measurement the laser frequency scanned a frequency interval of ± 30 GHz in 2.5 sec per scan. The data from the reference photo-multiplier tube, the absorption photomultiplier tube, and the laser scan width were each sampled at 1.0 kHz during the data acquisition period.

F-4.0 RESULTS

One result was glaringly evident from this measurement effort: the OH density at the exit plane was below the sensitivity threshold of the absorption system. System cross-checks, such as verifying the wavelength setting with the OH discharge lamp, during these measurements indicated that the entire system was functioning properly. Yet, no discernible trace of OH absorption was detected even though the strong Q_1 lines were monitored. This was true regardless of the altitude and engine power settings throughout the test period.

An effort was made to estimate the upper bound of the OH number density for the higher power settings of the 9.1-km altitude using the algorithm described above. The calculational results are shown in Table F-1. From the variety of lines measured, it is clear that the upper bound to the maximum OH number density is nominally 10^{12} cm^{-3}.

REFERENCE

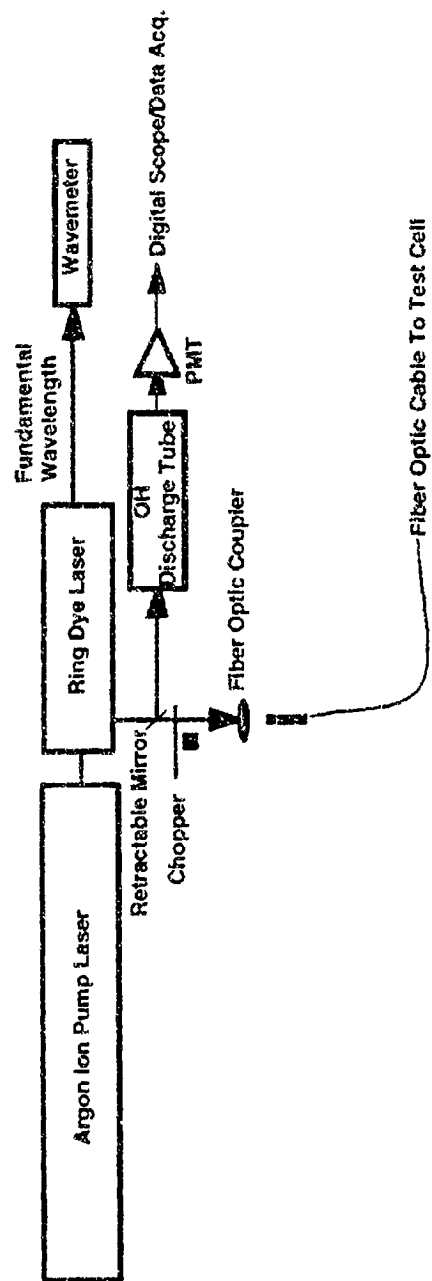F-1. Thorne, A. P. *Spectrophysics*. Chapman and Hall, 1974.

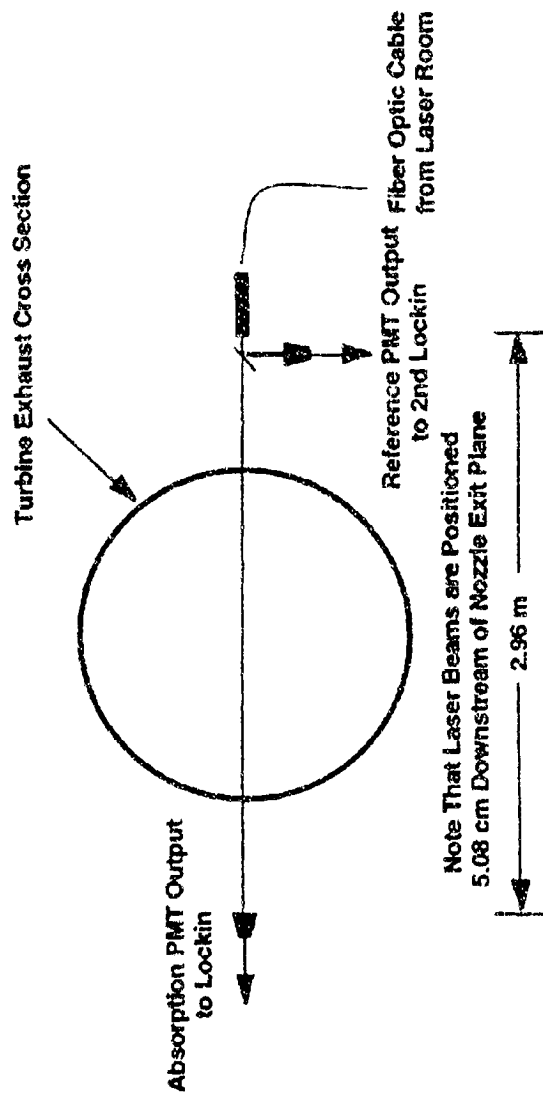Figure F-1. Schematic of experimental setup for OH measurements.

Figure F-2. OH laser beam arrangement in the test cell.

Table F-1. Estimates of Maximum OH Number Density at the 9.1-km Condition

T3 K	Line Measured	Maximum OH, cm^{-3}
671	$Q_1(5)$	1E12
733	$Q_1(2)$	1E12
	$Q_1(3)$	2E12
	$Q_1(4)$	2E12
	$Q_1(5)$	2E12
	$Q_1(6)$	1E12
765	$Q_1(4)$	3E11
808	$Q_1(4)$	5E11

Thorne, A. P., *Spectrophysics*, Chapman and Hall, 1974.